AN INVESTIGATION CONCERNING THE SIMULATION OF

TORNADO-LIKE VORTICES

by

STEFANIE GILLMEIER

A thesis submitted to the
University of Birmingham
for the degree of
DOCTOR OF PHILOSOPHY

Department of Civil Engineering
School of Engineering
College of Engineering and Physical Sciences
University of Birmingham
October 2018

ABSTRACT

Transient extreme wind events such as tornadoes have received increasing attention among Wind Engineers over the last years because those types of winds have been proven to be extremely dangerous and devastating. Several attempts of varying simplicity have been made to replicate the tornado flow structure analytically and experimentally. However, due to the assumptions made, those model results only show an extremely simplified version of what is a highly complex full-scale flow phenomenon.

In this work, the ability of those simplified models to replicate the flow field of atmospheric tornadoes is discussed thoroughly. A comparison between analytical and experimental models highlights that analytical vortex models are not able to represent the entire complexity of the three-dimensional flow structure obtained experimentally due to their simplifications. Furthermore, this work examines the effect of the simulator's design on the generated vortex flow field and thereby demonstrates that aspect ratio and swirl ratio parity is not enough to guarantee the simulation of vortices with similar flow characteristics in different simulators. This work shows that a better understanding of the flow fields simulated in physical tornado-like vortex simulators is required before data obtained from those models can be used with confidence in practice.

ACKNOWLEDGEMENTS

my research on many occasions to a broad audience. In addition, I would like to thank her for challenging me on tennis court. On this note, good luck in Wimbledon next year ☺.

I am also thankful to my office colleague Giulio Vita, for the enlightening discussions we had on a countless number of topics in our office, for the sometimes long and hard working days, during which we motivated each other and for all the fun we had.

Last but not least, I would like to thank my family and partner for their continuous support, for showing interest in my work and for their encouragement to peruse my interests. I would like to particularly thank my partner for the regular visits throughout the last four years, especially because plenty of sunnier and warmer destinations could have been reached within a similar travel time.

TABLE OF CONTENTS

LIST OF FIGURES

LIST OF TABLES

NOMENCLATURE

a	*[-]*	*aspect ratio*
$\bar{a}$	*[-]*	*constant in the Burgers-Rott and the Sullivan vortex model*
b	*[-]*	*shape parameter in the Sullivan vortex model*
D_1	*[m]*	*tornado simulator's convergence chamber diameter*
D_2	*[m]*	*tornado simulator's convection chamber diameter*
D_3	*[m]*	*tornado simulator's updraft hole diameter*
$\vec{g}$	*[ms^{-2}]*	*gravity vector*
H_1	*[m]*	*tornado simulator's convergence chamber height*
H_2	*[m]*	*tornado simulator's convection chamber height*
K	*[-]*	*constant in the Baker vortex model*
p	*[Nm^{-2}]*	*static pressure*
p_{min}	*[Nm^{-2}]*	*static pressure minimum*
$\bar{p}$	*[-]*	*normalised static pressure*
Q	*[m^{3}s^{-1}]*	*flow rate*
r	*[m]*	*radial distance*
R	*[m]*	*vortex core radius - radial distance at which $u_\theta = u_{\theta,max}$*
$\bar{r}$	*[-]*	*normalised radial distance*
$R_{average}$	*[m]*	*height-averaged core radius*
Re	*[-]*	*Reynolds number*
R_{global}	*[m]*	*vortex core radius - radial distance at which $u_\theta = u_{\theta,max,global}$*
R_{local}	*[m]*	*vortex core radius for each measurement height*
r_m	*[m]*	*radial distance at which u_r has its maximum*
S	*[-]*	*swirl ratio*

t	[s]	time
u_r	[m/s]	radial velocity component
$\overline{u}_r$	[-]	normalised radial velocity component
$u_{r,max}$	[m/s]	maximum of radial velocity component
u_z	[m/s]	vertical velocity component
$\overline{u}_z$	[-]	normalised vertical velocity component
u_θ	[m/s]	circumferential velocity component
$\overline{u}_\theta$	[-]	normalised circumferential velocity component
$u_{\theta,max}$	[m/s]	circumferential velocity maximum
$u_{\theta,max,average}$	[m/s]	height-averaged circumferential velocity maximum
$u_{\theta,max,global}$	[m/s]	overall circumferential velocity maximum
$u_{\theta,max,local}$	[m/s]	circumferential velocity maximum for each measurement height
z	[m]	vertical distance from surface
Z	[m]	vertical distance at which $u_{\theta,max,global}$ has its maximum
$\overline{z}$	[-]	normalised vertical distance
z_m	[m]	vertical distance at which u_r has its maximum
α	[°]	guide vane angle
γ	[-]	shape parameter in the Baker vortex model
Γ	[m^2s^{-1}]	circulation
Γ_{max}	[m^2s^{-1}]	circulation maximum
δ	[-]	length scale ratio of z_m to r_m
κ	[-]	kurtosis
θ	[°]	circumferential angle
v	[m^2s]	kinematic viscosity of the fluid
ρ	[kgm^{-3}]	density of the fluid
σ	[*]	standard deviation
ς	[-]	skewness

* Units of the standard deviation are identical to the units of the parameter the standard deviation is calculated for.

1. *INTRODUCTION*

A tornado is a violent rotating column of air attached to a thunderstorm base and in contact with the ground (e.g., *NSSL₁*). These devastating meteorological events can cause strong wind velocities close to the earth's surface on a relatively short temporal and small spatial scale compared to other wind related phenomena in the troposphere (Figure 1.1). Currently, regional meteorological forecasting models very rarely have a horizontal grid resolution of less than 1km. This means that sub-grid scale processes in the atmosphere are not seen by those models. Tornadoes fall under the category of sub-grid scale processes regarding the regional weather forecast (Figure 1.1). Figure 1.1 highlights that tornadoes can have a horizontal extent of approximately 100m and can last for several minutes. For this reason and due to the complexity of determining which thunderstorms may potentially produce a tornado, forecasting when and where a tornado will strike is difficult. In the United States (*US*) an advanced tornado watch and warning system, operated by the National Oceanic and Atmospheric Administration Storm Prediction Centre in collaboration with the local National Weather Service Forecast Office is in place (*NSSL₂*). If atmospheric conditions are favourable for severe weather to occur, a convective watch is issued for the respective area (*NOAA₁*). A warning is announced when a tornado has been sighted or indicated by weather radar (*NSSL₂*). This system currently allows warnings to be given approximately 13 minutes before a tornado strikes (*NOAA₂*). To improve this warning system and to avoid tornado related disruptions and fatalities, research is ongoing.
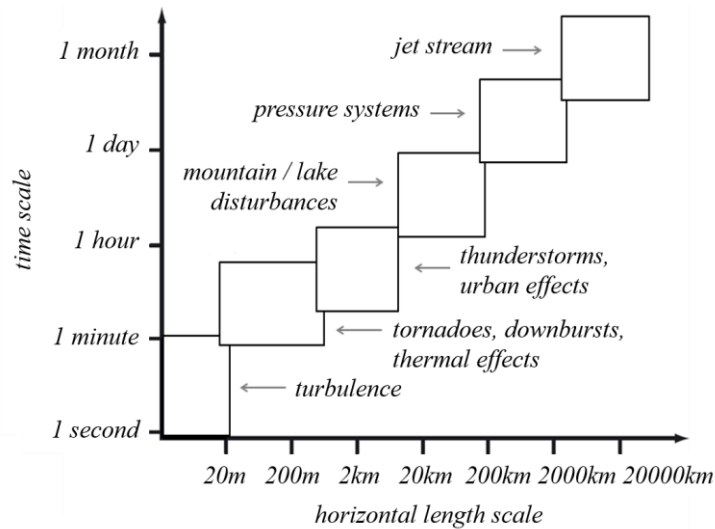
Figure 1.1: Atmospheric length and time scales (adapted from *Promet, 1971*).

On average, wind speeds in tornadoes reach approximately 200km/h (*Alexander and Wurman, 2008*) but can be in excess of 500km/h (*NSSL₃*). It is therefore not surprising that those types of winds can cause structural failures, disruption to everyday life and even death. Figure 1.2 illustrates the destruction caused by a tornado, which hit Joplin, Missouri on the 21st of May 2011. North America experienced one of the most destructive tornado seasons in 2011, with approximately 1600 tornado outbreaks reported and the total damage exceeding $28bn (*NOAA₃*). Solely during three days from 25th – 28th April 2011, 362 tornadoes hit the south-easterly part of the *US*, thereby causing an estimation of 321 fatalities and an approximate damage of $11 billion (*NOAA₄*). Significant damage also occurs elsewhere around the world but not necessarily as frequent or to such an extent. For instance, between 1950 and 2015, approximately 85 tornadoes hit Europe every year (*Antonescu et al., 2017*). This corresponds to only 7% of the number of tornadoes, which hit the *US* during the same period (*NSSL₃*).

Figure 1.2: Illustration of the destruction caused by the Joplin, Missouri tornado on the 21st of May 2011. The picture was taken by Melissa Brandes and is adapted from *shutterstock image ID 80099773*.

Due to the unfavourable combination of forecasting challenges and the deadly environment of a tornado, wind speed measurements inside tornadoes are limited, although, available datasets are increasing since the development of mobile Doppler radars, which enable wind speed measurements in tornadoes from a relatively safe distance. However, due to their working principle, the majority of available wind data are captured at heights much larger than the averaged common size building height (*Alexander and Wurman, 2008*). Additionally, due to the unsteady nature of a tornado, only instantaneous flow field information can be retrieved and for some cases, the spatial resolution of measurements is too low to resolve the highly complex flow structure. Because of that, recourse is often made to physical simulations to provide a statistical representative data set for tornado-like vortices, measured with a comparably high spatial and temporal resolution. In recent years, a variety of physical simulations but also analytical calculations have been undertaken in order to analyse tornado flow fields.

Whilst useful, analytical and physical models show a simplified version of a highly complex real life phenomenon with a large number of inherent assumptions, which may or may not be

correct. For that reason, this work and the publication by *Gillmeier et al. (2018)* provides detailed information about assumptions and limitations of each modelling technique.

Furthermore, despite most physical simulations being based largely on the same principles, i.e., tornado-like winds are created by generating a circulation in the presence of a suction updraft (*Ward, 1972*), currently used physical simulators differ in scale and geometric design. This makes comparison between vortices simulated in different simulators challenging because there is as of yet little understanding of how geometric boundary conditions of a simulator affect the similitude of generated vortices. The originality of this work is to investigate the sensitivity of experimentally simulated tornado-like vortices to the simulator's geometric boundary conditions.

1.1. Aim

The aim of this work is twofold. Firstly, to investigate whether the assumptions of analytical and experimental models allow a realistic simulation of tornado flow fields. Secondly, to improve our current understanding of physical tornado-like vortex modelling by assessing the sensitivity of results on the scale and the geometric design of experimental simulators.

1.2. Objectives

In order to address the above aim the following objectives have been defined.

Objective 1: to compare and contrast the flow field and surface pressure characteristics obtained in a physical simulator with those obtained analytically (step 1 in figure 1.3).

Objective 2: to examine the influence that scale (step 2.1 in figure 1.3) and geometry (step 2.2 in figure 1.3) may exert in the physical simulation of tornado-like vortices.
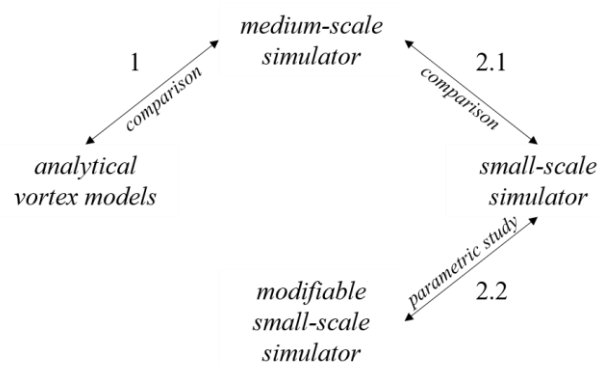
Figure 1.3: Illustration of objectives.

1.3. Thesis outline

This thesis is organised as follows. Sections 2.1 – 2.3 present relevant background knowledge, which enables an understanding of tornadoes. The assumptions made in analytical and physical vortex models are introduced in section 2.4 and 2.5, respectively. Section 3 contains a critical literature review, which is divided into three sections – section one provides a detailed review of a number of analytical models (3.1), section two reflects in detail on different physical vortex models with respect to their geometric and dynamic flow field similarity (3.2), whilst section three briefly summarises the motivation of this work and identifies the knowledge gap (3.3). Physical tornado-like vortex simulators at the University of Birmingham (*UoB*) are introduced in section 4 and the experimental setup including measurement and normalisation techniques and data quality are described in section 4.2 – 4.4. The comparison between analytical and physical vortex models is examined fully in section 5. Section 6 outlines the influence of a tornado simulator's scale and geometric design on the vortex flow field and section 7 highlights the dynamic flow field complexity. Reflections on findings of this work and recommendations for further work can be found in section 8.

2. BACKGROUND KNOWLEDGE

A significant amount of section 2.4 has been published elsewhere, see *Gillmeier et al. (2018)* and is reproduced with the permission of the authors.

2.1. Tornadoes – a meteorological phenomenon

Tornadoes are highly complex meteorological phenomena and require the environment of a supercell thunderstorm to occur. For that reason, it is essential to understand the physical processes within thunderstorms in order to understand the formation of tornadoes. One of the atmospheric preconditions, which is essential for the formation of every thunderstorm, is atmospheric instability, which is defined as positive buoyancy of warm air near the surface due to density differences (*Kraus, 2004*). If this near-surface warm layer of air is moist, its water content condensates when rising and latent heat is released. For that reason, moist air cools at a slower rate (moist adiabatic lapse rate) when rising compared to dry air (dry adiabatic lapse rate). In order to quantify the energy, which is available for the vertical air movement in the atmosphere, temperature soundings of the atmosphere can be used (*Stull, 2015*). Figure 2.1a shows an example of a temperature sounding during unstable atmospheric conditions. In a temperature sounding, the environmental temperature change with height (environmental lapse

rate) and corresponding moist and dry adiabatic lapse rates are illustrated. In unstable atmospheric conditions, an unsaturated air parcel close to the ground is lifted along the dry adiabat until it becomes saturated, which defines the height of the Lifting Condensation Level (*LCL*) (*Stull, 2015*, Figure 2.1a). Consequently, this height corresponds to the cloud base (Figure 2.1b). From the *LCL* upwards, the now saturated air parcel is lifted along the moist adiabat (Figure 2.1a). The Level of Free Convection (*LFC*) is defined at the altitude from the ground where the temperature of the environment drops below the moist adiabatic lapse rate (Figure 2.1a). At this point, the parcel accelerates upwards without further need for a forced lifting until it reaches the Equilibrium Level (*EL*), which represents a stable layer of air on top of the troposphere at approximately 10km above ground (*Stull, 2015*). When the updraft reaches the *EL*, the stable layer of air prevents the updraft from further rising. As a result, the air spreads out beneath this layer and a cloud forms, which is called Anvil (*Doswell and Burgess, 1993*; Figure 2.1b), because of the strong updraft, an overshooting top may form.

The area enclosed by *LCF*, the environmental lapse rate, the moist adiabatic lapse rate and *EL* defines the amount of energy, which is available for a thunderstorm's convective processes (e.g., *Stull, 2015*). This energy is referred to as Convective Available Potential Energy (*CAPE*) (Figure 2.1a). Consequently, the more *CAPE* is available, the faster storms will build vertically due to a strong vertical updraft (*NOAA$_5$*).
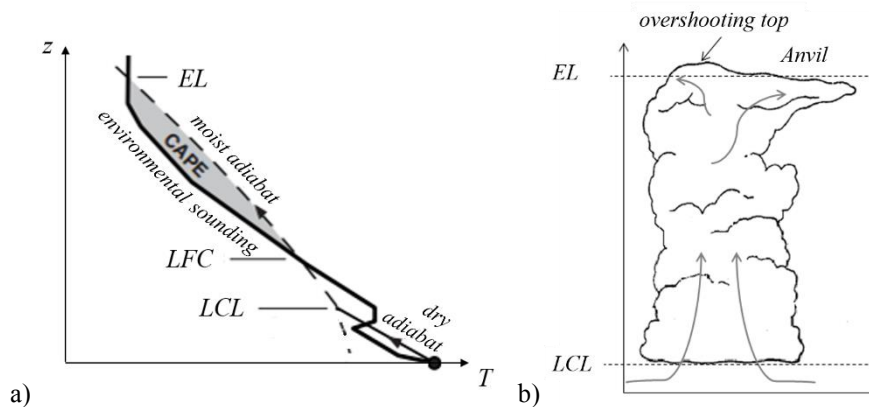
Figure 2.1: Illustration of a vertical temperature sounding of an unstable atmosphere (a) (adapted from *Stull, 2015*) and illustration of the initial formation of a thunderstorm (b) (adapted from *Letchford et al., 2002*).

During the mature stage of a thunderstorm, a downdraft forms beneath the overshooting top because cooled air becomes negatively buoyant and therefore, accelerates to the surface, associated with heavy rain or hail (*Letchford et al., 2002*; Figure 2.2a). A strong directional wind shear with height must be present in the thunderstorms inflow to initiate the development of a rotating updraft (*Davies-Jones et al., 2001*). If the updraft develops rotation, the thunderstorm is defined as supercell and a wall cloud forms at the updraft location at the base of the thunderstorm (*Doswell and Burgess, 1993*; Figure 2.2a). The larger the increase in wind speed with height, and the stronger the directional wind shear, the more intense the supercell becomes. The supercell's rotation is sustained by tilting the ambient near-surface horizontal vorticity vertically (*Davies-Jones et al., 2001*; Figure 2.2b). Horizontal vorticity at the surface is generated as a result of a strong directional wind shear with height, as illustrated at the top left corner of figure 2.2b. The rotational axis of those vortices is tilted vertically when ingested by the storm's updraft (*Davies-Jones, 1984*; Figure 2.2b). As a result, vertical vorticity is generated at mid-level altitudes (~5km) in the storms updraft (*Davies-Jones et al., 2001*). Furthermore, according to the meteorologist *Jeff Haby*, a sufficiently high enough increase in wind speed with height is necessary to tilt the storm's updraft (Figure 2.2b). This enables the

updraft and downdraft to occur at separate regions of the storm (Figure 2.2a) and thereby to enforce each other.

One of the contingencies regarding tornado genesis is the development of near-ground rotation (*Davies-Jones, 2006*). One of the theories describes the interaction between downdraft and updraft as essential for tornado genesis because the downdraft transports mid-level vertical vorticity back towards the surface and thereby initiates near-ground rotation (*Markowski and Richardson, 2009* and *Davies-Jones, 2015*). However, this suggested process could not be fully verified by field observations (*Davies-Jones, 2006*). It is also not yet fully understood why certain thunderstorms produce tornadoes and others of similar intensity do not. In general, for tornadoes to occur, it is important to have a stable and supportive alignment between thermal and mechanical atmospheric conditions, which enhance tornado genesis. If a tornado forms, a rotating funnel-shaped cloud lowers from the wall cloud (*Doswell and Burgess, 1993*; Figure 2.2a).

The final stage of a thunderstorm is the dissipating state, during which, the thunderstorm weakens, the updraft loses intensity and only the downdraft remains (*Letchford et al., 2002*).
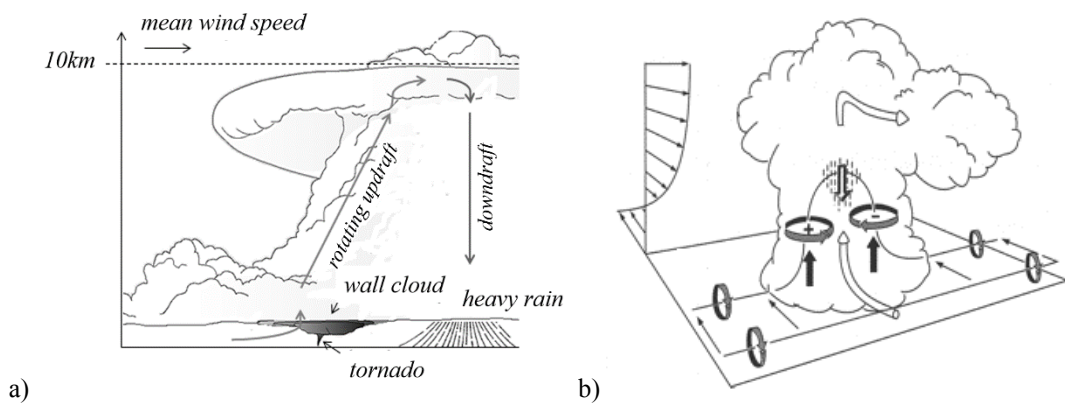
Figure 2.2: Illustration of the mature stage of a thunderstorm (adapted from *Doswell and Burgess, 1993*) (a) and illustration of the concept of how mid-level rotation is generated (taken from *Davies-Jones et al., 2001*).

2.2. The tornado flow structure

This section provides a more detailed look into the flow structure of an idealised axisymmetric tornado. In a tornado, the near-ground vertical vorticity is intensified by vortex stretching by the updraft. This implies that the diameter of the funnel-shaped cloud decreases with decreasing height, causing a local concentration of vertical vorticity near the surface due to conservation of angular momentum (*Lewellen, 1993*). This results in the lowering of maximum circumferential winds from high in the storm towards the surface (*Lewellen, 1993*). Due to this strong rotation, a region of low pressure occurs at the rotational axis, which causes the surrounding air to be sucked inwards (Figure 2.3a).

According to *Lewellen (1976)*, the flow field of an idealised axisymmetric tornado can be divided into four regions, which strongly interact with each other (Figure 2.3b).

(I)   The core flow: a region surrounding the vertical tornado axis and extending up to the radial distance where maximum circumferential velocities occur (the core radius, *R*). Dependent on the intensity of rotation, the flow structure in this region undergoes remarkable changes (e.g., *Snow, 1982* and *Rotunno, 2013*).

(II) The surface boundary layer flow: a region, which is dominated by radial inflow into the vortex centre.

(III) The surface corner flow: where the radial inflow turns and produces some type of vertical jet.

(IV) The upper flow: where the tornado is embedded in the parent thunderstorm (wall cloud). In this region, the tornado's rotation originates and is sustained as outlined in the previous section 2.1.
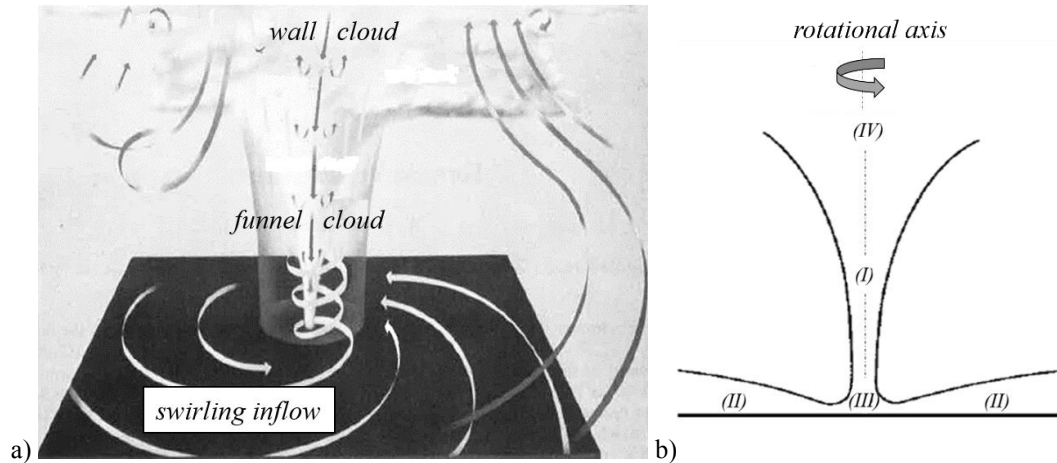
Figure 2.3: Flow structure of a tornado (a) (adapted from *Whipple, 1982*) and different flow regions in a simplified tornado (adapted from *Lewellen, 1976*).

Depending on the intensity of rotation, the vortex flow structure in the core flow region (region (I) in figure 2.3b) can differ significantly. Figure 2.4 shows an attempt to sketch the potentially occurring different flow structures in a simplified way. With increasing rotation, the core flow region may undergo the changes illustrated in figure 2.4 (e.g., *Snow, 1982* and *Rotunno, 2013*). A single-celled vortex structure with radial inflow and central updraft is seen in figure 2.4a and a two-celled vortex structure with a central downdraft, radial outflow from the vortex centre, radial inflow at larger radial distances and a vertical updraft in-between the radial inflow and outflow region is sketched in figure 4.2c. The transition from a single-celled to a two-celled vortex is known as vortex breakdown (e.g., *Trapp, 2000*). During the vortex breakdown, the core flow region is dominated by a central downdraft at greater heights, which terminates aloft a stagnation point (Figure 2.4b). Above the stagnation point, the vortex core broadens significantly (*Trapp, 2000*). With further increasing rotation, the stagnation point lowers until

it reaches the surface, which then describes the flow structure of a two-celled vortex (Figure 2.4c). With even further increasing rotation, the two-celled vortex structure becomes unstable and breaks into multiple vortices, which circle a strong central downdraft (Figure 2.4d). Each of the newly formed vortices can differ in intensity and therefore, flow patterns within their respective core flow regions can differ as well (*Snow, 1982*).

Differences in the observed flow structure can be explained by means of pressure differences between the upper flow region ($p_{(IV)}$) and the surface flow region ($p_{(III)}$) (Figure 2.3b). If $p_{(IV)} < p_{(III)}$, a central updraft is present in the core flow region and a flow structure similar to a single-celled vortex might be expected. The central downdraft of the two-celled vortex structure results in a decrease of the surface pressure deficit at the surface flow region and results in a larger $p_{(IV)}$ than $p_{(III)}$. Therefore, it can be expected that the surface pressure deficit at the surface flow region is larger for a single-celled vortex than for a two-celled vortex.

It is noted that illustrated flow structures in figure 2.4 are extremely simplified and idealised. The flow field of naturally occurring tornadoes can be considerably more complex than suggested by any of the illustrated flow structures in figure 2.4 (e.g., *Refan et al., 2017b*).
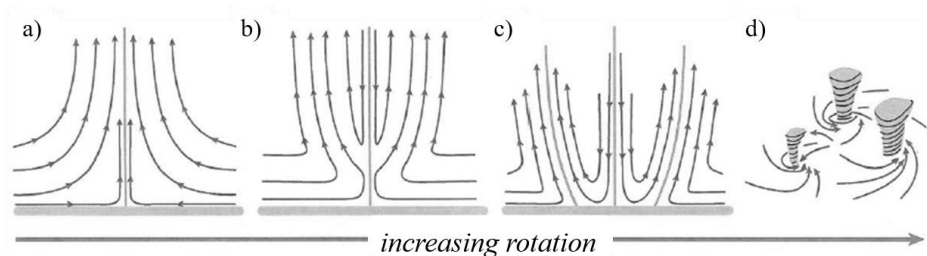
Figure 2.4: Illustration of vortex flow structure changes in the core flow region of an idealised vortex, with increasing rotation (adapted from *Rotunno, 2013*).

2.3. Full-scale tornado measurements

Atmospheric measurements inside tornadoes are extremely difficult because of their unpredictability and destructive environment. For that reason, evaluation systems such as the Fujita-scale and the Enhanced Fujita-scale in the *US* and the TORRO-scale in Europe determine the intensity of tornadoes based on a subsequent assessment of the caused damage.

The Fujita-scale is based on an interpolation of the Beaufort-scale and the Mach number. It clusters tornadoes in twelve intensities from F0 to F12, where F0 represents the tornado causing the least destruction and F12 represents the tornado causing the most damage (*Fujita, 1971*). In order to enable a more detailed distinction of tornado intensities within the Fujita-scale range where tornado damage has actually been observed, the National Weather Service modified the Fujita-scale to the Enhanced Fujita-scale (EF-scale) in 2007 (*Edwards et al., 2013*). The Enhanced Fujita-scale rates tornadoes from EF0 to EF5, where EF5 represents approximately the upper limit of the F3 Fujita-scale intensity (*Edwards et al., 2013*; Table 2.1). The EF-scale is based on the American way of construction and therefore, is not accepted outside the *US*. For Europe, the British TORnado & storm Research Organisation introduced a different scale to classify tornado intensities in the 1980's - the TORRO-scale (*Meaden, 1976*). This scale is an extension of the Beaufort-scale and has 10 clusters from T0 to T10, where T0 is the equivalent to Beaufort 8 and T7 corresponds to Beaufort 22 and approximately to EF5 and F3 (*Meaden, 1976*; Table 2.1). Table 2.1 outlines a rough comparison between different scales and provides an approximate estimation of corresponding wind velocities based on *Fujita (1971)*, *Elsom et al. (2001)* and *Edwards et al. (2013).*

Table 2.1: Overview and comparison of tornado damage based velocity evaluation systems such as the Fujita-scale, the EF-scale and the TORRO-scale.

Fujita-scale	EF-scale	TORRO-scale	Beaufort-scale	wind speed (m/s)
F 0	EF 0	T 0	8	~20
F 1	EF 1	T 1	10	~30
F 1	EF 1	T 2	12	~40
F 2	EF 2	T 3	14	~50
F 2	EF 2	T 4	16	~60
F 3	EF 3	T 5	18	~70
F 3	EF 4	T 6	20	~80
F 3	EF 5	T7	22	~90
F 4		T 8	24	~100
F 5		T 9	26	~115
F 5		T 10	28	~130

Thanks to the improving knowledge of radar technology and tornado field projects such as TWISTEX (*TWISTEX*), ROTATE (*CSWR*) and VORTEX (*NSSL$_4$*), the number of available full-scale tornado flow field measurements is gradually increasing. In particular, for velocity measurements inside tornadoes, the development of mobile Doppler radar technology was the breakthrough, allowing the flow structure in tornadoes to be mapped from a relatively safe distance. Thanks to this development, flow field information of approximately 150 tornadoes has been captured between 1995 and 2008 at heights > 20m with an approximate spatial resolution of ~50m every 60 seconds (*Alexander and Wurman, 2008*). For those tornadoes, large variations in circumferential velocity maxima (70m/s – 120m/s), core radii (75m – 400m) and translation speeds (10m/s – 20m/s) were observed (*Alexander and Wurman, 2008*). In some cases, the spatial resolution of measurements was too large to resolve the complex tornado flow structure (*Kosiba and Wurman, 2010*). However, to date, the three-dimensional flow field of multiple tornadoes could be obtained from single-Doppler data, e.g., the Mulhall, Oklahoma tornado (*Lee and Wurman, 2005*), the Harper, Kansas tornado (*Kosiba et al., 2008*), the

Spencer, South Dakota tornado (*Kosiba and Wurman, 2010*) and the tornadoes at Clairemont, Texas (2005), Stockton, Kansas, (2005), Happy, Texas (2007) and Goshen Country, Wyoming (2009) (*Refan et al., 2017b*). Potential single-celled and two-celled vortex flow structures have been inferred for most of those tornadoes; however, flow patterns in their vortex cores ($r < R$) have revealed multiple smaller circulation cells and highly complex and unsteady flow characteristics.

A detailed insight in the three-dimensional structure and evolution of the boundary layer of the Russell, Kansas tornado (2012) was provided by *Kosiba and Wurman (2013)*. Velocity measurements obtained at heights greater than 3.5m revealed that the highest circumferential velocities occur close to the ground and a strong decrease in circumferential velocities with height was observed. This highlights one of the most restricting factors of Doppler radar tornado data from a wind engineering perspective, viz., velocity information of most Doppler radar measurements are restricted to only a limited number of heights, which very often are much higher than the averaged building height of residential, industrial and public buildings. The reason for this is the reflectivity of radar lights on obstacles and the earth's curvature for larger distances (*Alexander and Wurman, 2008*).

A further improvement of forecasting possible tornado events would be extremely beneficial for in-situ surface pressure measurements because pressure sensors need to be installed and placed in the expected path of a tornado before the tornado strikes, in order to capture relevant surface pressure characteristics. It is noted that similar to velocity measurements, also surface pressure characteristics are extreme dependent on the radial distance from the tornado's central axis. For that reason, it is important to quantify the distance from the vortex centre to the

corresponding pressure sensor; however, the transient behaviour of tornadoes makes an analysis of such data sets challenging. Nevertheless, *Winn et al. (1999)* recorded surface pressure data of the Allison, Texas tornado (1995) and *Lee et al. (2004)* successfully retrieved the surface pressure distribution of the Manchester, South Dakota tornado (2003) and *Karstens et al. (2010)* measured the surface pressure distribution of seven individual tornadoes of different intensity between 2002 and 2008.

Due to challenges of individual measurement techniques, there is still a lag of detailed complimentary velocity and surface pressure measurements of the same tornado.

2.4. *Existing analytical vortex models*

The lack of full-scale data has driven the need to model tornado-like vortices analytically. In this section, detailed descriptions of the most commonly used analytical vortex models to replicate tornado-like flow behaviour (viz., the Rankine (*Rankine, 1882*), the Burgers-Rott (*Burgers, 1948* and *Rott, 1958*) and the Sullivan (*Sullivan, 1959*) vortex model) are provided, together with their derivations and underlying assumptions. In addition, detailed information of the derivation and simplifications of the recently published vortex model by *Baker and Sterling (2017)*, hereafter called 'Baker vortex model' are provided.

A cylindrical coordinate system has been adopted as illustrated in figure 2.5, in which, r, z and θ are the radial distance, vertical distance and circumferential angle, respectively. Thus, u_r, u_z

and u_θ represent the radial, vertical and circumferential components of velocity. For the sake of simplicity, the flow of the analysed vortex models is considered to be incompressible and a density of air of $\rho = 1.2\text{kg/m}^3$ is assumed for all calculations.

Using the aforementioned notation, the continuity equation (2.1), radial, circumferential and vertical components of the Navier-Stokes-Equations (*NSE*, equations 2.2 – 2.4) can be expressed as:
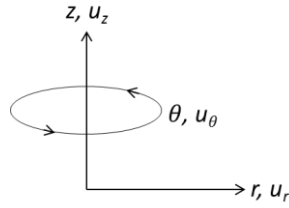
Figure 2.5: Flow field notation.

$$\underbrace{\frac{1}{r}\frac{\partial(ru_r)}{\partial r}}_{1} + \underbrace{\frac{1}{r}\frac{\partial u_\theta}{\partial \theta}}_{2} + \underbrace{\frac{\partial u_z}{\partial z}}_{3} = 0 \tag{2.1}$$

$$\underbrace{\frac{\partial u_r}{\partial t}}_{R1} + \underbrace{u_r\frac{\partial u_r}{\partial r}}_{R2} + \underbrace{\frac{u_\theta}{r}\frac{\partial u_r}{\partial \theta}}_{R3} - \underbrace{\frac{u_\theta^2}{r}}_{R4} + \underbrace{u_z\frac{\partial u_r}{\partial z}}_{R5} =$$

$$\underbrace{-\frac{1}{\rho}\frac{\partial p}{\partial r}}_{R6} + \underbrace{g_r}_{R7} + \nu\left(\underbrace{\frac{1}{r}\frac{\partial}{\partial r}\left(r\frac{\partial u_r}{\partial r}\right)}_{R8} - \underbrace{\frac{u_r}{r^2}}_{R9} + \underbrace{\frac{1}{r^2}\frac{\partial^2 u_r}{\partial \theta^2}}_{R10} - \underbrace{\frac{2}{r^2}\frac{\partial u_\theta}{\partial \theta}}_{R11} + \underbrace{\frac{\partial^2 u_r}{\partial z^2}}_{R12}\right) \tag{2.2}$$

$$\underbrace{\frac{\partial u_\theta}{\partial t}}_{C1} + \underbrace{u_r\frac{\partial u_\theta}{\partial r}}_{C2} + \underbrace{\frac{u_\theta}{r}\frac{\partial u_\theta}{\partial \theta}}_{C3} + \underbrace{\frac{u_r u_\theta}{r}}_{C4} + \underbrace{u_z\frac{\partial u_\theta}{\partial z}}_{C5} =$$

$$\underbrace{-\frac{1}{\rho r}\frac{\partial p}{\partial \theta}}_{C6} + \underbrace{g_\theta}_{C7} + \nu\left(\underbrace{\frac{1}{r}\frac{\partial}{\partial r}\left(r\frac{\partial u_\theta}{\partial r}\right)}_{C8} - \underbrace{\frac{u_\theta}{r^2}}_{C9} + \underbrace{\frac{1}{r^2}\frac{\partial^2 u_\theta}{\partial \theta^2}}_{C10} - \underbrace{\frac{2}{r^2}\frac{\partial u_r}{\partial \theta}}_{C11} + \underbrace{\frac{\partial^2 u_\theta}{\partial z^2}}_{C12}\right) \tag{2.3}$$

$$\underbrace{\frac{\partial u_z}{\partial t}}_{Z1} + \underbrace{u_r \frac{\partial u_z}{\partial r}}_{Z2} + \underbrace{\frac{u_\theta}{r} \frac{\partial u_z}{\partial \theta}}_{Z3} + \underbrace{u_z \frac{\partial u_z}{\partial z}}_{Z4} =$$

$$\underbrace{-\frac{1}{\rho} \frac{\partial p}{\partial z}}_{Z5} + \underbrace{g_z}_{Z6} + \nu \left(\underbrace{\frac{1}{r} \frac{\partial}{\partial r}\left(r \frac{\partial u_z}{\partial r}\right)}_{Z7} + \underbrace{\frac{1}{r^2} \frac{\partial^2 u_z}{\partial \theta^2}}_{Z8} + \underbrace{\frac{\partial^2 u_z}{\partial z^2}}_{Z9} \right) \qquad (2.4)$$

where, t is the time, p is the static pressure, $\vec{g}$ is the gravity vector in its different components and ν is the kinematic viscosity of the fluid.

Different terms in equations $(2.1 - 2.4)$ have been labelled since, as will be demonstrated in this section, it is possible to derive the Rankine, the Burgers-Rott, the Sullivan and the Baker vortex models by disregarding different terms.

In addition to the aforementioned analytical vortex models, an attempt to analytically model the three-dimensional flow in the boundary layer of a tornado-like vortex was made by *Kuo (1971)* by alternatingly solving the two non-linear boundary layer equations for the radial and vertical distribution of velocities. The *Bloor and Ingham* vortex model *(1987)* and the Vyas-Majdalani vortex model (*Vyas et al., 2003*) are exact inviscid solutions to the Euler's equations in a confined conical and cylindrical domain, respectively. *Xu and Hangan (2009)* analytically modelled an inviscid tornado-like vortex using a free narrow jet solution combined with a modified Rankine vortex. However, it is noted that this combined model is not an exact solution to the Navier-Stokes-Equations. *Wood and White (2011)* presented a new parametric model that is based on the Vatistas model (*Vatistas et al., 1991*) and is primarily designed to depict realistic-looking circumferential wind profiles observed in atmospheric vortices. An overview

of some of the aforementioned vortex models can be found in *Kilty (2005)*, *Batterson et al. (2007)* and *Kim and Matsui (2017)*.

In what follows, the focus is set on the Rankine, the Burgers-Rott, the Sullivan and the Baker vortex model.

2.4.1.   Rankine vortex model

The Rankine vortex model has been adopted by a number of researchers (e.g., *Hoecker, 1960*; *Church et al., 1979*; *Winn et al., 1999*; *Wurman and Gill, 2000*; *Brown and Wood, 2004*; *Lee et al., 2004*; *Mishra et al., 2008a*; *Bech et al., 2009*; *Hashemi Tari et al., 2010*; *Wood and Brown, 2011*; *Refan and Hangan, 2016* and *Tang et al., 2018*) to model tornado-like flow behaviour. The following assumptions are made in the derivation of the Rankine vortex model:

- *The flow field is one-dimensional and as such equations (2.3) and (2.4), terms R2, R3 and R5 can be disregarded.*
- *The flow field is steady state, i.e., term R1 can be taken as zero.*
- *The flow is inviscid (v = 0), i.e., terms R8 - R12 can be neglected.*
- *Body forces can be neglected, i.e., ($\vec{g}$ = 0).*

Those assumptions reduce the *NSE* to the cyclostrophic equation (Eq. 2.5).

$$\frac{dp(r)}{dr} = \rho \frac{u_\theta(r)^2}{r} \qquad (2.5)$$

The Rankine vortex model also assumes that the flow consists of two separate flow regions. In the core region (i.e., $r < R$, where R is the core radius, which is defined as the radial distance from the vortex centre at which the circumferential velocity component attains its maximum), the flow is assumed to have a constant vorticity and is considered to be similar to that of a solid body. Outside the core region ($r > R$), it is assumed that the flow can be described by a potential flow field (incompressible, inviscid and irrotational) (*Alekseenko et al., 2007*) and is inversely proportional to the radial distance. Those assumptions enable the circumferential velocity component to be modelled via an expression of the form:

$$\overline{u_\theta}(\bar{r}) = \begin{cases} \bar{r} & for\ (\bar{r} < 1) \\ \frac{1}{\bar{r}} & for\ (\bar{r} > 1) \end{cases} \qquad (2.6)$$

where, $\overline{u_\theta}$ is the normalised circumferential velocity component ($=u_\theta/u_{\theta,max}$, where $u_{\theta,max}$ is the maximum value of u_θ) and $\bar{r}$ is the radial distance normalised by the core radius, R ($= r/R$). In equation (2.6), a discontinuity occurs at $\bar{r} = 1$. In order to avoid this, the model is occasionally modified as shown in equation (2.6.1). However, the most commonly used form is shown in equation 2.6 and hence, will be used in what follows.

$$\overline{u_\theta}(\bar{r}) = \frac{2\bar{r}}{(1 + \bar{r}^2)} \qquad (2.6.1)$$

Combining equation (2.6) with equation (2.5) and integrating, yields an expression for the normalised pressure distribution of the Rankine vortex model (Eq. 2.7):

$$\bar{p}(\bar{r}) = \begin{cases} \overline{p_{(\bar{r}=0)}} + \frac{1}{2}(\bar{r})^2 & for\ (\bar{r} < 1) \\ \overline{p_{\bar{r} \to \infty}} - \frac{1}{2}\left(\frac{1}{\bar{r}}\right)^2 & for\ (\bar{r} > 1) \end{cases} \quad (2.7)$$

where, $\bar{p}(\bar{r})$ is the normalised pressure ($=p(r)/\rho u_{\theta,max}{}^2$), $\overline{p_{\bar{r} \to \infty}}$ is the normalised static pressure, which is unaffected by the vortex and $\overline{p_{(\bar{r}=0)}}$ is the static pressure at the vortex centre.

2.4.2.   *Burgers-Rott vortex model*

The Burgers-Rott vortex model has been adopted by a number of authors (e.g., *Winn et al., 1999*; *Brown and Wood, 2004*; *Lee et al., 2004*; *Kosiba and Wurman, 2010*; *Wood and Brown, 2011* and *Wurman et al., 2013*) to model tornado-like flow behaviour. Explicit in the derivation of the model are the following assumptions:

- *The flow field is steady state, i.e., terms R1, C1 and Z1 are taken as zero.*
- *The viscosity is considered to be constant throughout the entire flow field.*
- *Body forces can be neglected, i.e., ($\vec{g} = 0$).*
- *The circumferential velocity component is assumed to be solely dependent on the radial distance ($u_\theta = u_\theta(r)$).*
- *The vertical velocity component is assumed to be solely and linearly dependent on the vertical distance ($u_z = u_z(z)$ and $u_z \propto z$).*
- *As a result of the last two assumptions, the radial velocity component is solely and linearly dependent on the radial distance ($u_r = u_r(r)$ and $u_r \propto r$).*

- *The static pressure is assumed to be solely dependent on radial and vertical distances (p=p(r,z)).*

Those assumptions reduce equations (2.1 – 2.4) to the following simplified versions:

$$\frac{1}{r}\frac{\partial(ru_r)}{\partial r} + \frac{\partial u_z}{\partial z} = 0 \tag{2.1*}$$

$$u_r\frac{\partial u_r}{\partial r} - \frac{u_\theta^2}{r} = -\frac{1}{\rho}\frac{\partial p}{\partial r} + \nu\left(\frac{1}{r}\frac{\partial}{\partial r}\left(r\frac{\partial u_r}{\partial r}\right) - \frac{u_r}{r^2}\right) \tag{2.2*}$$

$$u_r\frac{\partial u_\theta}{\partial r} + \frac{u_r u_\theta}{r} = \nu\left(\frac{1}{r}\frac{\partial}{\partial r}\left(r\frac{\partial u_\theta}{\partial r}\right) - \frac{u_\theta}{r^2}\right) \tag{2.3*}$$

$$u_z\frac{\partial u_z}{\partial z} = -\frac{1}{\rho}\frac{\partial p}{\partial z} \tag{2.4*}$$

Now, the Burgers-Rott vortex model acknowledges that the flow within a tornado-like vortex structure is likely to be subject to changing levels of vorticity, which in turn will have implications for the associated pressure field. Thus, it is assumed that the vertical velocity component changes with respect to height and the following relationship is adopted:

$$\overline{u_z}(\bar{z}) = 2\bar{a}\bar{z} \tag{2.8}$$

where, $\overline{u_z}(\bar{z})$ is the normalised vertical velocity $(=u_z(z)/u_{\theta,max})$, $\bar{z}$ is the normalised vertical height $(= z/R)$ and $\bar{a}$ is a constant, whose magnitude purports to account for the strength of

vortex stretching. It is also assumed that $\bar{a}$ is related to the viscous dissipation, v, via an expression of the form:

$$\bar{a} = \frac{2v}{Ru_{\theta,max}} \qquad (2.8.1)$$

Equation (2.8.1) implies that the viscous dissipation, v, continuously removes kinetic energy from the flow, which is continuously introduced by vortex stretching. Using equation (2.8) and integrating the simplified continuity equation (Eq. 2.1*), an expression for the normalised radial velocity component can be obtained (Eq. 2.9).

$$\overline{u_r}(\bar{r}) = -\bar{a}\bar{r} \qquad (2.9)$$

where, $\overline{u_r}(\bar{r})$ is the normalised radial velocity ($=u_r(r)/u_{\theta,max}$). Using equations (2.8) and (2.9), and solving the simplified *NSE* in the circumferential direction (Eq. 2.3*), an expression for the normalised circumferential velocity component, $\overline{u_\theta}$, can be found (Eq. 2.10).

$$\overline{u_\theta}(\bar{r}) = \frac{1}{\bar{r}}\left(1 - exp(-\bar{r}^2)\right) \qquad (2.10)$$

It is perhaps worth noting that $\overline{u_z}$ and $\overline{u_r}$ increase to infinity as $\bar{z}\rightarrow\infty$ and $\bar{r}\rightarrow\infty$, respectively, which, it is suggested, may not be representative of a tornado-like flow structure.

The pressure distribution of the Burgers-Rott vortex model can be obtained by solving the simplified *NSE* (Eq. 2.2* and Eq. 2.4*) using the model velocities (Eq. 2.8, Eq. 2.9, and Eq. 2.10). This leads to the following equation for the normalised pressure distribution (Eq. 2.11).

$$\bar{p}(\bar{r}, \bar{z}) = \bar{p}(0,0) + \int_0^{\bar{r}} \frac{\overline{u_\theta(\bar{r}\prime)}^2}{\bar{r}\prime} d\bar{r}\prime - \frac{\bar{a}^2}{2}(\bar{r}^2 + 4\bar{z}^2) \tag{2.11}$$

2.4.3.   *Sullivan vortex model*

The Sullivan vortex model has also been adopted by a few researchers (e.g., *Winn et al., 1999* and *Wood and Brown, 2011*) to model tornado-like flow behaviour. The assumptions for this vortex model are:

- *The flow field is steady state, i.e., terms R1, C1 and Z1 are taken as zero.*

- *The viscosity is considered to be constant throughout the entire flow field.*

- *Body forces can be neglected, i.e., ($\vec{g} = 0$).*

- *The circumferential velocity component is assumed to be solely dependent on the radial distance ($u_\theta = u_\theta(r)$).*

- *The vertical velocity component is assumed to be only dependent on radial and vertical distances. The dependence on the vertical distance is linear ($u_z = u_z(r,z)$ and $u_z \propto z$).*

- *As a result of the last two assumptions, the radial velocity component is solely dependent on the radial distance ($u_r = u_r(r)$).*

- *The static pressure is assumed to be solely dependent on radial and vertical distances ($p = p(r,z)$).*

Those assumptions reduce the continuity equation (2.1), radial and circumferential components of the *NSE* (2.2 – 2.3) to simplified versions shown in equations (2.1* – 2.3*). For the vertical component of the *NSE* (2.4) the following simplified version is obtained.

$$u_z \frac{\partial u_z}{\partial z} + u_z \frac{\partial u_z}{\partial z} = -\frac{1}{\rho} \frac{\partial p}{\partial z} + v \left(\frac{1}{r} \frac{\partial}{\partial r} \left(r \frac{\partial u_z}{\partial r} \right) \right) \qquad (2.4^{**})$$

One main difference of the Sullivan vortex model compared to the Burgers-Rott vortex model lies in the complexity of the model solution. While the Burgers-Rott vortex model only allows single-celled vortices to be generated, the Sullivan vortex model potentially enables solutions for single-celled and two-celled vortices to be obtained; this is obtained via the use of a shape parameter, b (Eq. 2.12 and Eq. 2.13). The effect of this parameter on the tornado-like flow field will be discussed in detail in section 3.1.2. Unless stated otherwise, $b = 3$. The required vortex stretching is generated by suction at relatively large heights and is achieved by a non-linear increase of the vertical velocity component with height, as illustrated in equation (2.12). The same normalisation used for the Burgers-Rott vortex model is applied for the Sullivan vortex model.

$$\overline{u_z}(\bar{r}, \bar{z}) = 2\bar{a}\bar{z}\big(1 - b \cdot exp(-\bar{r}^2)\big) \qquad (2.12)$$

Following the procedure described for the Burgers-Rott vortex model, expressions for $\overline{u}_r$ (Eq. 2.13) and $\overline{u}_\theta$ (Eq. 2.14) can be obtained.

$$\overline{u_r}(\bar{r}) = -\bar{a}\bar{r} + \frac{2b\bar{v}}{\bar{r}}\big(1 - exp(-\bar{r}^2)\big) \qquad (2.13)$$

$$\overline{u_\theta}(\bar{r}) = \frac{1}{\bar{r}} \frac{H(x)}{H(\infty)} \tag{2.14}$$

$$\textit{with } \ x = \bar{r}^2 \quad \textit{and } \ H(x) = \int_0^x exp\left(-x' + 3 \int_0^{x'} \frac{1}{x''}\left(1 - exp(-x'')\right)dx''\right)dx'$$

It is perhaps worth noting, that for $\bar{r} = 0$ and $\bar{z} \rightarrow \infty$ the magnitude of $\overline{u_z}$ increases to infinity. Furthermore, also $\overline{u_r}$ increases to infinity for $\bar{r} \rightarrow \infty$ (Eq. 2.13). Similar to the Burgers-Rott vortex model, it is suggested that this behaviour may be physically unrealistic for a tornado-like flow structure.

The pressure distribution of the Sullivan vortex model can be obtained by solving the simplified *NSE* (Eq. 2.2*, 2.3* and 2.4**) using the model velocities (Eq. 2.12 – 2.14). This leads to the following equation for the normalised pressure distribution:

$$\bar{p}(\bar{r}, \bar{z}) = \overline{p_{Burgers}}(\bar{r}, \bar{z}) - \frac{18\bar{v}^2}{\bar{r}^2}\left(1 - exp(-\bar{r}^2)\right)^2 \tag{2.15}$$

where, $\overline{p_{Burgers}}$ is the pressure distribution of the Burgers-Rott vortex model, which is given in equation (2.11).

2.4.4.   *Baker vortex model*

Baker and Sterling (2017) developed a vortex model, which can reproduce the flow and pressure characteristics of single-celled and two-celled vortices. For simplicity, only the

solution for the single-celled vortex with radial inflow and vertical updraft is analysed in what follows. The following assumptions are made in the derivation of the Baker vortex model:

- *The flow field is steady state, i.e., terms R1, C1 and Z1 are taken as zero.*

- *The flow is inviscid, i.e., terms R8 - R12, C8 - C12 and Z7 - Z9 can be disregarded.*

- *Body forces can be neglected, i.e., ($\vec{g} = 0$).*

- *The circumferential velocity component is assumed to be dependent on radial and vertical distance ($u_\theta = u_\theta(r,z)$).*

- *The radial velocity component is assumed to be only dependent on radial and vertical distances ($u_r = u_r(r,z)$).*

- *As a result of the last two assumptions, the vertical velocity component is solely dependent on radial and vertical distances ($u_r = u_r(r,z)$).*

- *The static pressure is assumed to be solely dependent on radial and vertical distances ($p = p(r,z)$).*

Those assumptions reduce the continuity equation (2.1) to the simplified version shown in equation (2.1*) and the *NSE* (Eq. 2.2 – 2.4) to the following simplified versions:

$$u_r \frac{\partial u_r}{\partial r} - \frac{u_\theta^2}{r} + u_z \frac{\partial u_r}{\partial z} = -\frac{1}{\rho} \frac{\partial p}{\partial r} \tag{2.2***}$$

$$u_r \frac{\partial u_\theta}{\partial r} + \frac{u_r u_\theta}{r} + u_z \frac{\partial u_\theta}{\partial z} = 0 \tag{2.3***}$$

$$u_r \frac{\partial u_z}{\partial r} + u_z \frac{\partial u_z}{\partial z} = -\frac{1}{\rho} \frac{\partial p}{\partial z} \tag{2.4***}$$

In addition, the Baker vortex model assumes that the radial velocity component takes the following form:

$$\overline{u_r}(\bar{r},\bar{z}) = \frac{-4\bar{r}\bar{z}}{(1+\bar{r}^2)(1+\bar{z}^2)} \tag{2.16}$$

One of the potential advantages of this model compared to the Rankine, the Burgers-Rott and the Sullivan vortex model is that the radial velocity component is assumed to show a more realistic flow behaviour (Eq. 2.16), i.e., rather than increasing to infinity for large radial distances, a maximum value is reached at $r = r_m$ and for $r = 0$ and $r = \infty$ the radial velocity falls to zero. In the vertical direction, the radial velocity distribution shows an attempt to replicate the tornado boundary layer by assuming a maximum in the radial velocity component at a known distance above the ground $(z = z_m)$ and for $z = 0$ and $z = \infty$ the radial velocity falls to zero. Since the Baker vortex model focuses on the distribution of the radial velocity component, different parameters have been chosen by *Baker and Sterling (2017)* for the normalisation of velocities and distances. Velocities are normalised by the maximum radial velocity $(u_r(r_m,z_m)=u_{r,max})$ and radial and vertical distances are normalised by r_m and z_m, respectively.

Using equation (2.16) and integrating the simplified continuity equation (2.1*), an expression for the normalised vertical velocity component, $\overline{u_z}$, can be obtained as follows:

$$\overline{u_z}(\bar{r},\bar{z}) = \frac{4\delta\, ln(1+\bar{z}^2)}{(1+\bar{r}^2)^2} \tag{2.17}$$

where, δ is the ratio z_m/r_m. Using equations (2.16) and (2.17), and solving the simplified *NSE* in the circumferential direction (Eq. 2.3***), the following expression for the normalised circumferential velocity component, $\overline{u_\theta}$, can be obtained:

$$\overline{u_\theta}(\bar{r}, \bar{z}) = \frac{K\bar{r}^{\gamma-1}\left[ln(1+\bar{z}^2)\right]^{\gamma/2}}{(1+\bar{r}^2)^{\gamma/2}} \tag{2.18}$$

where, γ is a shape parameter, which can be used to adjust the shape of the circumferential velocity profile. K is a constant and is related to Baker's definition of the swirl ratio, $S_{Baker} = 0.347\ K$. The swirl ratio in the Baker vortex model is defined as the ratio of $u_\theta(r_m,z_m)$ to $u_r(r_m,z_m)$. It is perhaps worth noting that $\overline{u_\theta}$ increases to infinity for $z\rightarrow\infty$. This increase is assumed to be realistic for the lowest heights, relatively close to the surface, where surface roughness affects the velocities, but becomes physically unrealistic for larger heights.

The pressure distribution of the Baker vortex model can be obtained by solving the simplified *NSE* (Eq. 2.2*** and Eq. 2.4***) using the model velocities (Eq. 2.16 – 2.18). In order to obtain equation (2.19) a shape parameter of $\gamma = 2$ was assumed.

$$\bar{p}(\bar{r}, \bar{z}) = -\frac{8\bar{r}^2\bar{z}}{(1+\bar{r}^2)^2(1+\bar{z}^2)^2} - \frac{4.15S_{Baker}^2\left(ln\left(1+\bar{z}^2\right)\right)^2}{(1+\bar{r}^2)} - \frac{4ln\left(1+\bar{z}^2\right)\left(1-\bar{z}^2\right)}{(1+\bar{r}^2)^2(1+\bar{z}^2)^2} \tag{2.19}$$

where, $\bar{p}(\bar{r},\bar{z})$ is the normalised pressure ($=p(r,z)/\rho u_r(r_m,z_m)^2$).

It is worth noting that the surface pressure distribution equals zero for $z = 0$. This behaviour is physically unrealistic for a tornado and is discussed in *Baker and Sterling (2017)*. It is assumed that pressure variations in the vertical direction can be neglected within the boundary layer ($z < z_m$) and consequently, it is assumed that $\bar{p}(\bar{r},\bar{z}<1)=\bar{p}(\bar{r},\bar{z}=1)$ (*Baker and Sterling, 2017*).

2.5. Physical simulation of tornado-like vortices

The lack of full-scale data has also driven the need to model tornado-like vortices experimentally in physical tornado-like vortex simulators. Those simulators by their very nature are also simplified models, but arguably more realistic than some analytical vortex models. The use of physical simulators results in a number of advantages compared to full-scale measurements since it allows us to measure surface pressure and flow characteristics easily and safely and to obtain data sets, which are statistically representative due to controlled boundary conditions.

The general aim of tornado-like vortex simulators is to simplify the tornado flow field by mechanically forcing a vortex to occur (*Davies-Jones, 1976*). The main forcing mechanisms involve the introduction of vorticity and its subsequent convergence (*Davies-Jones, 1976*). Typically, in tornado simulators, vorticity is introduced mechanically by means of guide vanes, rotating screens or fans. This is necessary because neither thermally introduced buoyancy, nor vertical wind shear are present to introduce a rotating updraft as outlined in section 2.1. Resulting from those simplifications, physical simulators generate axisymmetric vortices, which are stationary in time and space with respect to their time-averaged flow characteristics (unless translation is taken into account).

Ward (1972) was the first to be acknowledged to have simplified the physical processes in a thunderstorm in a mechanical way that enabled the simulation of tornado-like vortices (*Davies-Jones, 1976*). For that reason, the design of currently used physical tornado-like vortex generators is still based on the design introduced by *Ward (1972)*. The simulator by *Ward*

(1972) consists of a convergence region of height H_1 and diameter D_1 (Figure 2.6), which is characterised by radial inflow and corresponds to the atmospheric sub-cloud inflow layer. Rotating screens surrounding the convergence chamber introduce vertical vorticity, which is responsible for the generation of a swirling flow. A fan on top generates a negative pressure difference, which encourages the air to move vertically through the system and stretches the vortex towards the convection region of height H_2 and diameter D_2 (Figure 2.6). This area is assumed to represent convective process in a cumulus cloud. A flow rectifier on top removes any vorticity at the upper boundary of the simulator and provides a uniformly distributed vorticity sink. The surface between convergence and convection chamber prevents convection from outside the central updraft region of diameter D_3 (Figure 2.6).
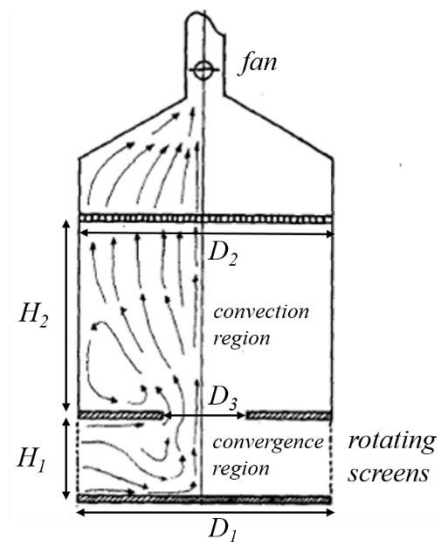
Figure 2.6: Basic schematic of the tornado-like vortex simulator based on the design introduced by *Ward (1972)*, illustrating the major components of the apparatus. H_1 and D_1 are the height and diameter of the convergence chamber, H_2 and D_2 are the height and diameter of the convection chamber and D_3 is the diameter of the updraft hole (adapted from *Church et al., 1979*).

2.5.1. *Parameters governing the flow characteristics and flow field similitude*

This degree of simplicity, lends itself to easily examining which parameters of the simulator influence the generated flow field the most. Dimensional analysis is a powerful tool to reduce the degree of freedom of a physical system by grouping together parameters, which affect the system, solely based on their dimensions in order to form non-dimensional numbers (e.g., *Gibbings, 2011*). In order to simulate similar flow characteristics in different systems, e.g., different physical tornado simulators, geometric, kinematic and dynamic similarity between those systems needs to be ensured (*Munson et al., 2012*). This means that the ratio of corresponding length scales (geometric similarity), velocity scales (kinematic similarity) and forces acting on the fluid (dynamic similarity) have to be equal. The degree to which those requirements are satisfied determines the extent to which conclusions drawn from one system apply to another system (*Davies-Jones, 1976*).

Davies-Jones (1973) undertook a dimensional analysis and reported that six non-dimensional numbers describe the flow characteristics in a tornado simulator based on the design introduced by *Ward (1972)*. Of those, four define the geometric similarity of the simulator. *Davies-Jones (1973)* chose the following set (Eq. 2.20). Geometric length scales are defined as depicted in figure 2.6

$$H_1 / \tfrac{1}{2}D_3; \quad H_2 / \tfrac{1}{2}D_1; \quad \tfrac{1}{2}D_2 / \tfrac{1}{2}D_1; \quad \tfrac{1}{2}D_3 / \tfrac{1}{2}D_1 \qquad (2.20)$$

It is noted that a different set of parameters could have been chosen. Table 2.2 outlines all possible geometric relations in a tornado-like vortex simulator based on the design introduced

by *Ward (1972)*. Geometric similarity between simulators is assured if four independent geometric relations are identical, since this guarantees that all lengths scales are determined and scaled in proportion. Furthermore, it needs to be highlighted here that there are geometric parameters that have not been taken into account, such as the geometric design of rotating screens, guide vanes or fans that introduce vorticity to the flow field. This issue is addressed in more detail in section 3.2.2. Furthermore, it is noted that the ratio between convergence chamber height (H_1) and updraft radius ($\frac{1}{2}D_3$) is defined as the aspect ratio (*a*).

Table 2.2: All possible geometric relations in a tornado-like vortex simulator based on the design introduced by *Ward (1972)*.

H_1/H_2	$H_1/\frac{1}{2}D_1$	$H_1/\frac{1}{2}D_2$	$H_1/\frac{1}{2}D_3$	$H_2/\frac{1}{2}D_1$	$H_2/\frac{1}{2}D_2$	$H_2/\frac{1}{2}D_3$	$\frac{1}{2}D_1/\frac{1}{2}D_2$	$\frac{1}{2}D_1/\frac{1}{2}D_3$	$\frac{1}{2}D_2/\frac{1}{2}D_3$

In addition to geometric parameters, the flow field is also a function of the flow rate through the simulator and the circulation at a certain location in the simulator (*Davies-Jones, 1973*). Therefore, two additional non-dimensional numbers describe the effect of rotational (Eq. 2.21) and viscous (Eq. 2.22) forces on the flow field. *Davies-Jones (1973)* defined them in the following way:

$$\frac{\Gamma(r,z)H_1}{Q} \tag{2.21}$$

$$\frac{Q}{\nu H_1} \tag{2.22}$$

where, *Q* is the flow rate through the system and *Γ(r,z)* is the circulation at a certain location in the simulator, which is defined as:

$$\Gamma(r,z) = 2\pi r \cdot u_\theta(r,z) \tag{2.23}$$

Assuming that no losses occur between the simulator's inlet and outlet, the following assumption can be made.

$$Q = \pi D_1 H_1 u_{r,inlet} \equiv \pi \left(\frac{1}{2}D_3\right)^2 u_{z,outlet} \tag{2.24}$$

where, $u_{r,inlet}$ ($u_{z,outlet}$) is a representative radial (vertical) velocity component at the simulator's inlet (outlet).

If Γ and Q are both defined at the circumference of the convergence chamber, where guide vanes are potentially in place ($r = D_1$), the non-dimensional number described by equation (2.21) can be transformed into the following equation (*Davies-Jones, 1973*):

$$\frac{\Gamma_{inlet} H_1}{Q_{inlet}} = \frac{\pi D_1 H_1 u_{\theta,inlet}}{\pi D_1 H_1 u_{r,inlet}} = \frac{u_{\theta,inlet}}{u_{r,inlet}} \equiv \tan(\alpha) \tag{2.25}$$

where, α is the guide vane angle with respect to the radial distance.

Very frequently, this parameter is found in combination with the aspect ratio, thereby forming a dependent non-dimensional number, which is defined as the swirl ratio, S. (Eq. 2.26, *Davies-Jones, 1973*).

$$S = \frac{\tan(\alpha)}{2a} \tag{2.26}$$

The swirl ratio has been found to be of significant importance for the flow field transformation

from a single-celled vortex to multiple vortices as outlined in section 2.2. The effect of the swirl ratio on flow characteristics of simulated vortices is well understood and has been examined in detail (e.g., *Wan and Chang, 1971*; *Ward, 1972*; *Davies-Jones, 1973*; *Jischke and Parang, 1974*; *Church et al., 1977 and 1979*; *Rotunno, 1977 and 1979*; *Monji, 1985*; *Haan et al., 2008*; *Hangan and Kim, 2008*; *Hashemi Tari et al., 2010*; *Liu and Ishihara, 2012*; *Zhang and Sarkar, 2012; Refan and Hangan, 2016 and 2018* and *Tang et al., 2018*). The factor of 2 in the denominator of equation (2.26) was introduced by *Davies-Jones (1973)* in order to form a parameter, which is supposed to apply more specifically to atmospheric vortices (*Church et al., 1979*).

The non-dimensional number defined in equation (2.22) is known as the Reynolds number, *Re*, and describes the ratio of inertial to viscous forces in the fluid (*Reynolds, 1883*). Similar to traditional wind tunnel experiments, the full-scale Reynolds number cannot be matched in a tornado generator because unfeasibly high wind speeds would be required to compensate for the geometric down scaling. For that reason, similar to wind tunnel simulations, the Reynolds number similarity needs to be relaxed when comparing experimentally simulated tornado-like vortices to atmospheric tornadoes. However, above a critical Reynolds number, the fluid dynamics are assumed to be similar within a fully developed turbulent flow and therefore, independent from the Reynolds number. This assumption originates from the connection of the inverse of the Reynolds number to the momentum exchange by molecular motion in the dimensionless Reynolds-Averaged-Navier-Stokes-equation (e.g., *Doering and Gibbon, 1995*). Since the effect of molecular motion decreases in a turbulent flow field (at large Reynolds numbers) it can be argued that flow characteristics become independent of the Reynolds number if the Reynolds number is sufficiently large. However, only if this independence is proven at

critical measurement positions (e.g., locations of relatively low wind speed) over a reasonably large range of Reynolds numbers, generated data can be considered to be representative. With respect to the simulation of tornado-like vortices, this issue was address by *Ward (1972)*, *Davies-Jones (1976)* and *Church et al. (1979)*, who found that above a critical Reynolds number, the overall vortex flow structure remains only marginally dependent on the Reynolds number. *Tang et al. (2018)* showed that the first four moments of surface pressure measurements are independent from the Reynolds number. However, it is noted that for the latter study, the range of Reynolds numbers is relatively small ($2.4 \times 10^5 < Re < 3.9 \times 10^5$). *Refan and Hangan (2017a)* analysed the effect of the Reynolds number on time-averaged surface pressure measurements over a larger range ($1.6 \times 10^4 < Re < 2.0 \times 10^6$) and reported that time-averaged surface pressure measurements are independent from the Reynolds number above a critical Reynolds number.

A detailed discussion regarding the design and geometric similarity of currently used tornado-like vortex simulators can be found in section 3.2.1 and 3.2.2, respectively. The dynamic similarity, including the definition of swirl ratio and Reynolds number, plus their application and use in current tornado research is discussed in section 3.2.3 and 3.2.4.

3. *LITERATURE REVIEW*

It is noted that the majority of section 3.1 has been published in *Gillmeier et al. (2018)* and is reproduced with the permission of the co-authors.

3.1. *A reflection on analytical tornado-like vortex models*

In this section, the flow and surface pressure characteristics of the Rankine, the Burgers-Rott, the Sullivan and the Baker vortex model, are reviewed in detail.

3.1.1. *The circumferential velocity component*

Unlike the Rankine, the Burgers-Rott and the Sullivan vortex model, the Baker vortex model has a shape parameter, γ, which enables the shape of the circumferential velocity profile to be varied. The effect of this parameter on the circumferential velocity field is illustrated in figure 3.1 and table 3.1. It is perhaps worth noting that γ is related to the normalised radial distance ($\bar{r}$) in the following way ($\bar{r}^2 = \gamma - 1$) (*Baker and Sterling, 2017*). Thus, to ensure results, which

describe the behaviour of a forced vortex at the centre, and a free vortex at larger radial distances, *Baker and Sterling (2017)* recommend setting $\gamma = 2$.
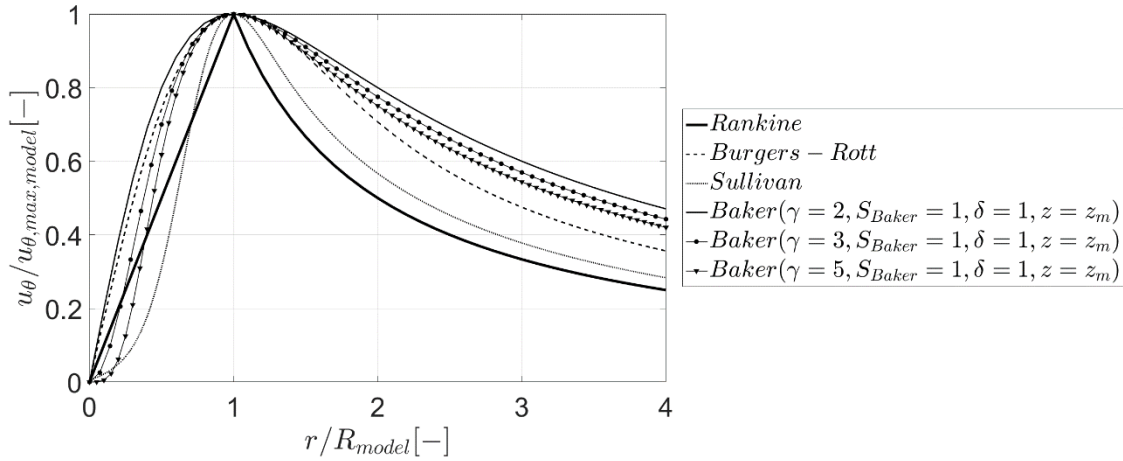
Figure 3.1: Circumferential velocity component of the Rankine, the Burgers-Rott, the Sullivan and the Baker vortex model.

Table 3.1: Ratios of $u_{\theta,max}$ and R of the corresponding vortex model compared to the Rankine vortex model.

	$\dfrac{u_{\theta,max,x}}{u_{\theta,max,Rankine}}$	$\dfrac{R_x}{R_{Rankine}}$
x=Rankine	1.00	1.00
x=Burgers	0.64	1.12
x=Sullivan	0.32	2.29
x=Baker (γ=2, $z=z_m$)	1.00	1.00
x=Baker (γ=3, $z=z_m$)	0.64	1.41
x=Baker (γ=5, $z=z_m$)	0.33	2.00

Table 3.1 illustrates the ratio of $u_{\theta,max}$ and R of the corresponding vortex model compared to the Rankine vortex model with input parameters of $R = 10$m and $u_{\theta,max} = 10$m/s. For the Baker vortex model a swirl ratio of $S_{Baker} = 1$ is assumed and readings for the maximum circumferential velocity component are taken at $z = z_m$. Table 3.1 shows that the Burgers-Rott and the Sullivan vortex model underestimate the actual input velocity by a factor of *0.64* and

0.32, respectively, and overestimate the core radius position, *R*, by a factor of *1.12* and *2.29,* respectively. For the Baker vortex model with a shape parameter of $\gamma = 2$, the radius at which $\bar{u}_r$ attains a maximum, is identical to the core radius of the Baker vortex model and is also identical to the actual input core radius ($r_m = R_{Baker} = R$). Hence, model parameters of the Rankine vortex model and the Baker vortex model for $\gamma = 2$ are identical (Table 3.1). With increasing γ, R_{Baker} increases and the magnitude of $u_{\theta,max,Baker}$ decreases (Table 3.1). For $\gamma = 3$, *R* and $u_{\theta,max}$ of the Baker and the Burgers-Rott vortex model are similar and show a decrease in $u_{\theta,max}$ by about 1/3 $u_{\theta,max,Rankine}$ (Table 3.1). For $\gamma = 5$, *R* and $u_{\theta,max}$ of the Baker and the Sullivan vortex model are similar and show a core radius, which is about 2 $R_{Rankine}$ and a decrease in $u_{\theta,max}$ by about 2/3 $u_{\theta,max,Rankine}$ (Table 3.1). Thus, in what follows, care has been taken to normalise, by the relevant model values of each vortex model as opposed to a standard value; hence, radial distances are normalised by the corresponding core radius (R_{model}), velocity components are normalised by the corresponding circumferential velocity maximum ($u_{\theta,max,model}$) and surface pressures are normalised by the corresponding surface pressure minimum ($p_{min,model}$).

Figure 3.1 shows that among the four vortex models, large differences in the circumferential velocity are found for $r < R_{model}$ between the Sullivan and the Baker vortex model with a shape parameter of $\gamma = 2$ (Figure 3.1). This is not surprising as those vortex models represent two entirely different tornado flow types. The Sullivan vortex model represents a two-celled vortex, whereas the Baker vortex model, as shown here, shows a single-celled vortex structure. In a two-celled vortex, the downdraft reaches the ground and therefore, decreases $\bar{u}_\theta$ close to $r = 0$, whereas the structure of a single-celled vortex shows a strong non-linear increase of $\bar{u}_\theta$ inside the vortex core ($r < R_{model}$) (Figure 3.1).

For the Baker vortex model, close to the vortex core, $\bar{u}_\theta$ increases at a slower rate with increasing γ, and the circumferential velocity profile tends towards the shape of a two-celled vortex structure (Figure 3.1). For larger radial distances ($r > R_{model}$), $\bar{u}_\theta$ of the Baker vortex model decreases at a slower rate compared to the other three models and largest differences are found between the Rankine vortex model and the Baker vortex model ($\gamma = 2$). Differences in the circumferential velocity of all vortex models decrease as $r \rightarrow \infty$.

The effect of γ on the circumferential velocity component with height is shown in Figure 3.2. For relatively small vertical distances from the surface, $\bar{u}_\theta$ increases at a slower rate the larger γ is. With increasing vertical distance, this behaviour reverses and $\bar{u}_\theta$ increases faster with height as γ increases (Figure 3.2). Furthermore, figure 3.2 shows that independent from γ, $\bar{u}_\theta$ increases to infinity for $z \rightarrow \infty$, albeit at different rates. It is noted that the Baker vortex model is the only model that takes a height dependence of the circumferential velocity component into account. However, it does not represent the vertical profile of the circumferential velocity observed in simulated tornado-like vortices or full-scale. For instance, *Tang et al. (2018)* showed that the circumferential velocity increases rapidly in the lowest heights with the maximum circumferential velocity occurring relatively close to the ground. With further increasing height, u_θ was found to decrease and to remain relatively uniform in even greater heights. *Refan et al. (2017b)* showed that a similar behaviour was observed in five different full-scale tornadoes of different intensity and flow structure.
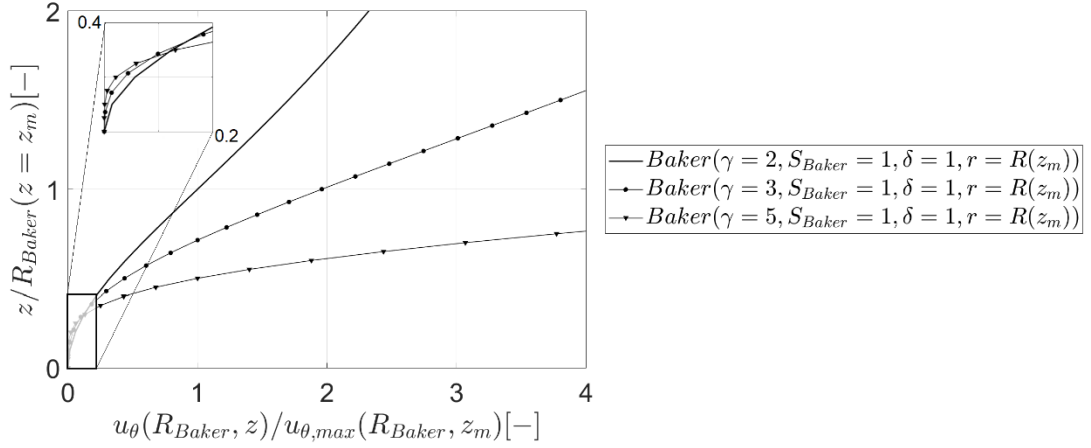
Figure 3.2: Circumferential velocity component of the Baker vortex model in different heights for different γ values.

Another parameter that influences the shape of the circumferential velocity profile of the Baker vortex model is the swirl ratio, S_{Baker}. The magnitude of u_θ increases as the value of S_{Baker} increases. The position of the core radius and the shape of the circumferential velocity profile are independent from the chosen swirl ratio. For that reason, the effect of S_{Baker} on the circumferential velocity profile cannot be seen when normalising u_θ with $u_{\theta,max,Baker}$.

3.1.2.   Radial and vertical velocity components

The Baker vortex model is not the only model to employ a shape component. As shown in equation (2.8) and (2.12), both, the Burgers-Rott and the Sullivan vortex model also include a 'constant' to 'adjust' the vertical velocity component. In addition, both models have a 'viscosity' parameter explicitly included in the circumferential velocity component (which is not evident in equations (2.10) and (2.14) due to the normalisation adopted and assuming the relationship given in equation (2.8.1)). If it is assumed that the viscosity parameter corresponds

to the kinematic viscosity of air (i.e., $v \sim 10^{-5}$ m^{2}s^{-1} at 20 °C), then the calculated radial and vertical velocity components of the Burgers-Rott and the Sullivan vortex model are small. Hence, to ensure reasonable magnitudes of the velocity components (Figures 3.3 and 3.4), the viscosity needs to be increased by several orders of magnitude (*Davies-Jones and Kessler, 1974*). Thus, in this context, the 'viscosity' parameter is essentially nothing more than a 'simple' shape parameter.

Figure 3.3 and figure 3.4 show the effect of the 'viscosity' parameter on velocity and pressure distributions of the Burgers-Rott and the Sullivan vortex model. For the Burgers-Rott vortex model, a larger 'viscosity' parameter results in larger vertical and radial velocities (Figure 3.3). Hence, the larger the value of v becomes, the greater the radial inflow towards the vortex centre becomes and the stronger the vertical updraft gets (Figure 3.3). For the Sullivan vortex model, an increase in v results in larger negative vertical velocities for $r < R_{Sullivan}$, and larger positive vertical velocities for $r > R_{Sullivan}$ (Figure 3.4). For the radial velocity, the larger v is, the stronger the radial outflow at $r < R_{Sullivan}$ becomes, and the stronger the radial inflow for $r < R_{Sullivan}$ gets (Figure 3.4). The radial distance at which radial and vertical velocity components change sign is not affected by changes in the 'viscosity' parameter (Figure 3.4). This means that the size of the downdraft region close to $r = 0$ is independent of v.
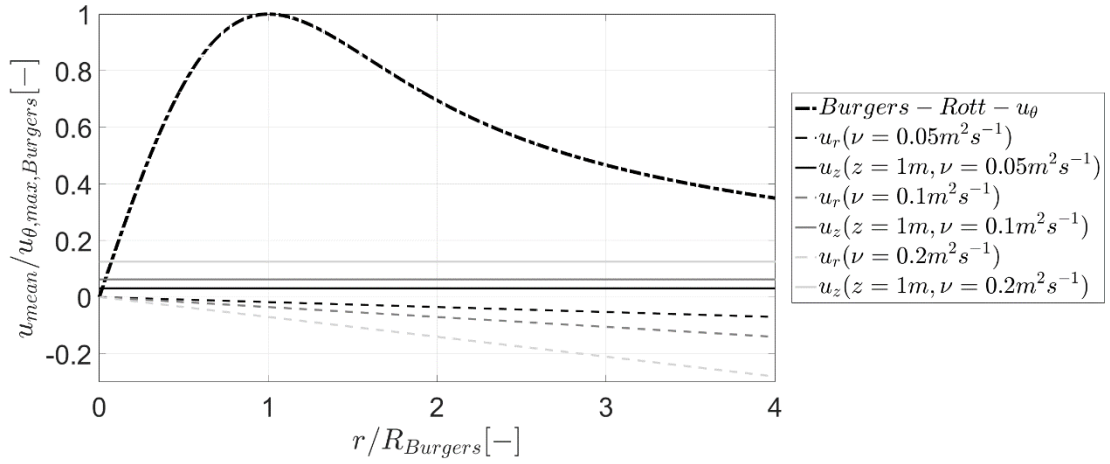
Figure 3.3: Velocity components of the Burgers-Rott vortex model for different 'viscosity' values.
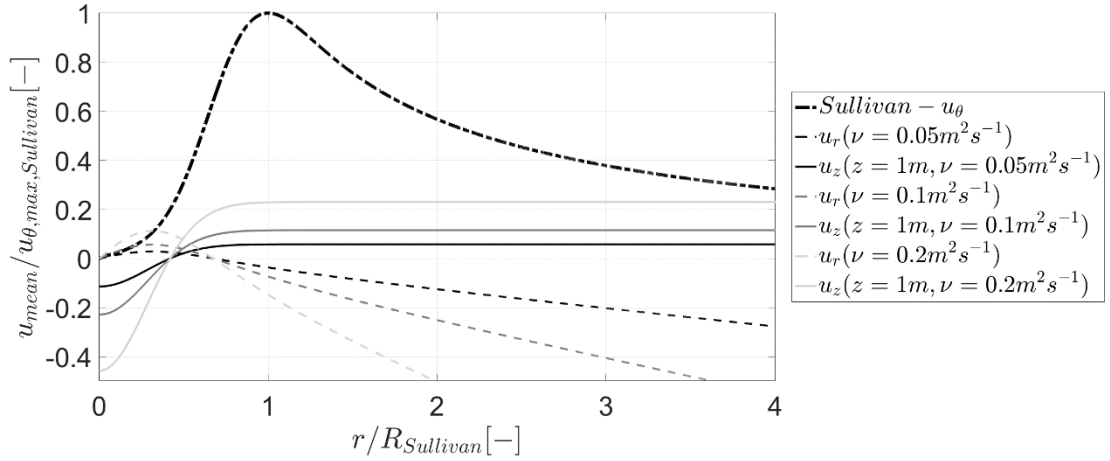
Figure 3.4: Velocity components of the Sullivan vortex model for different 'viscosity' values.

An additional shape parameter contained in the Sullivan vortex model is denoted as *b*. This parameter influences the distribution of radial and vertical velocity components and can be adjusted to model solutions for single-celled and two-celled vortices. Figure 3.5 illustrates the effect of *b* on the radial and vertical flow field of the Sullivan vortex model. For *b = 0*, radial and vertical velocity components of the Sullivan vortex model are identical to the solutions obtained from the Burgers-Rott vortex model. For *b > 1*, a two-celled flow structure can be obtained, which is indicated by negative vertical velocities close to the vortex centre. The

greater the magnitude of *b* gets, the larger the magnitude of the central downdraft becomes, and additionally, the further the downdraft region extends in the radial direction. For $r > R_{Sullivan}$, the vertical velocity converges to a value, which is independent of *b,* but dependent on the height. Radial outflow velocities inside the vortex core are larger for larger *b* values, and the larger *b* gets, the larger the region of radial outflow extends radially (Figure 3.5). Radial inflow velocities obtained with a lower *b* value increase slightly faster in magnitude close to the vortex core, but converge for larger radial distances (Figure 3.5). Hence, differences of *b* are only significant inside the vortex core.
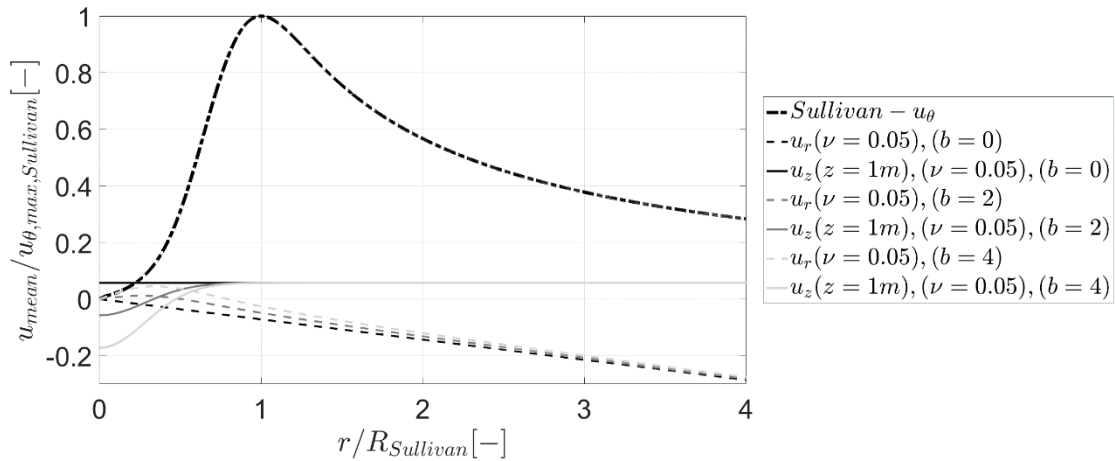
Figure 3.5: Velocity components of the Sullivan vortex model for different *b* values.

The vertical velocity component of the Baker vortex model depends on the value of δ. The vertical velocity component at the vortex centre increases with increasing δ (Figure 3.6a). Additionally, figure 3.6b shows that the vertical velocity component increases faster with height as δ increases.

a)

b)
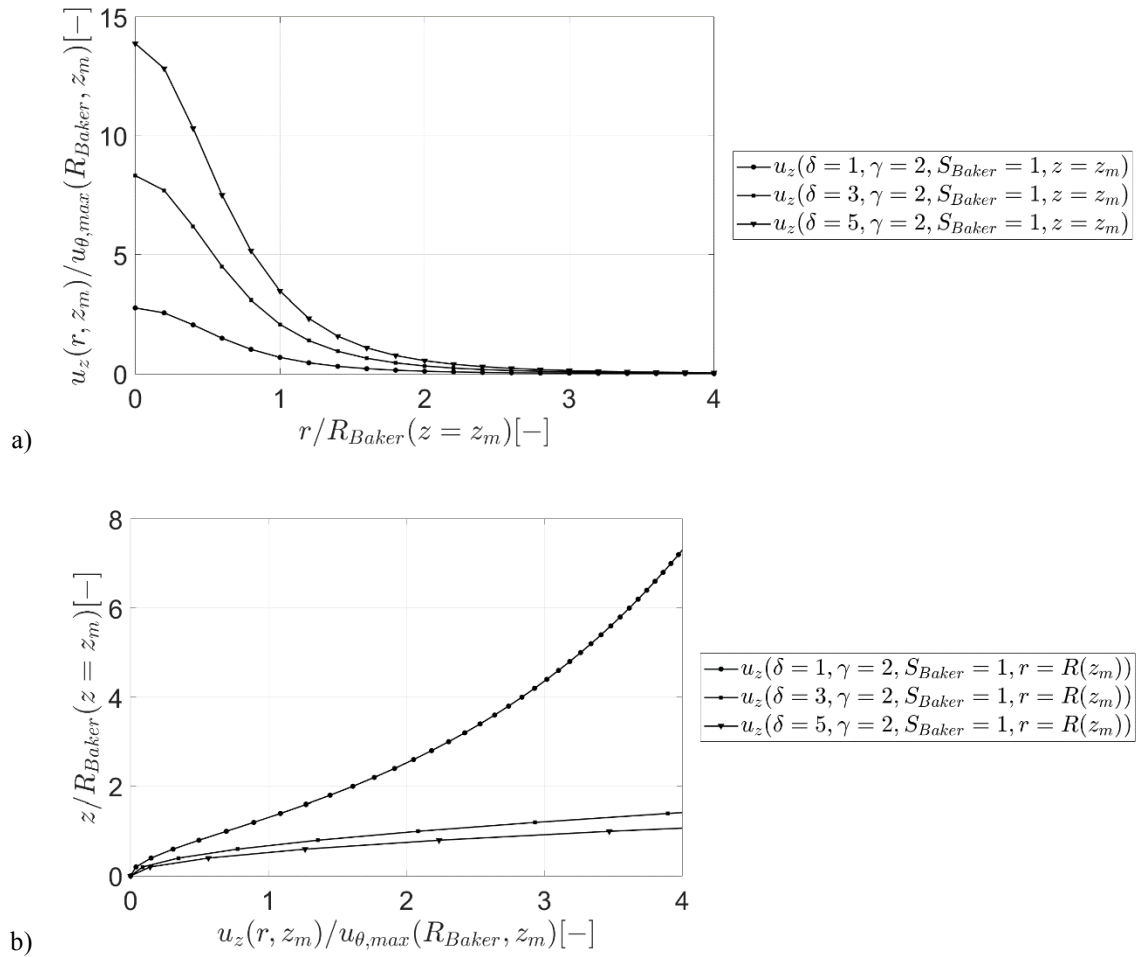
Figure 3.6: The effect of δ on the vertical velocity component of the Baker vortex model for different radial distances (a) and different heights (b).

3.1.3.   The static surface pressure distribution

The surface pressure distribution of the Rankine, the Burgers-Rott and the Sullivan vortex model are shown in figure 3.7 for the case of $v = 0$. This restriction implies that the surface pressure distributions are solely dependent on the circumferential velocity profile of the corresponding vortex model and equations (2.11) and (2.15) simplify to:

$$\bar{p}(\bar{r}, \bar{z}) = \bar{p}(0,0) + \int_0^{\bar{r}} \frac{\overline{u_\theta}(\bar{r}\prime)^2}{\bar{r}\prime} \, d\bar{r}\prime \qquad\qquad (3.1)$$

The last term on the right-hand side gives the largest contribution to the entire pressure distribution of those models. Thus, its value defines the magnitude of the surface pressure increase from the vortex centre towards larger radial distances and is determined by the area underneath the corresponding circumferential velocity profile shown in figure 3.1. For that reason, this term is largest for the Burgers-Rott vortex model and results in what maybe a physically unrealistic surface pressure increase from the vortex centre (Figure 3.7). For the Sullivan vortex model, the magnitude of this term is of the same order as that one of the Rankine vortex model.

The entire pressure distribution of the Burgers-Rott and the Sullivan vortex model, depend on the contribution of the circumferential, radial and vertical velocity (Eq. 2.11 and Eq. 2.15) and therefore, is dependent on the 'viscosity' parameter. Also shown in Figure 3.7, is the effect of v on the pressure distribution. The decrease in surface pressure with increasing radial distance originates from a combination of the vertical updraft and the potentially unrealistic increase in radial velocity, i.e., $\frac{\bar{a}^2}{2}\left(\bar{r}^2 + 4\bar{z}^2\right)$. Those terms are identical in the Burgers-Rott and the Sullivan vortex model; however, the different magnitudes of this decrease shown in figure 3.7 arise due to the normalisation, since $R_{Sullivan} > R_{Burgers}$.

The additional term in the surface pressure distribution of the Sullivan vortex model (i.e., $-\frac{18\bar{v}^2}{\bar{r}^2}\left(1 - exp\left(-\bar{r}^2\right)\right)^2$) describes the effect of the non-linear behaviour of radial and vertical velocity components inside the vortex core on the pressure distribution. The downdraft close to

the centre of the vortex increases the surface pressure and places the minimum pressure at the radial position where vertical and radial velocity components are zero (Figure 3.7).
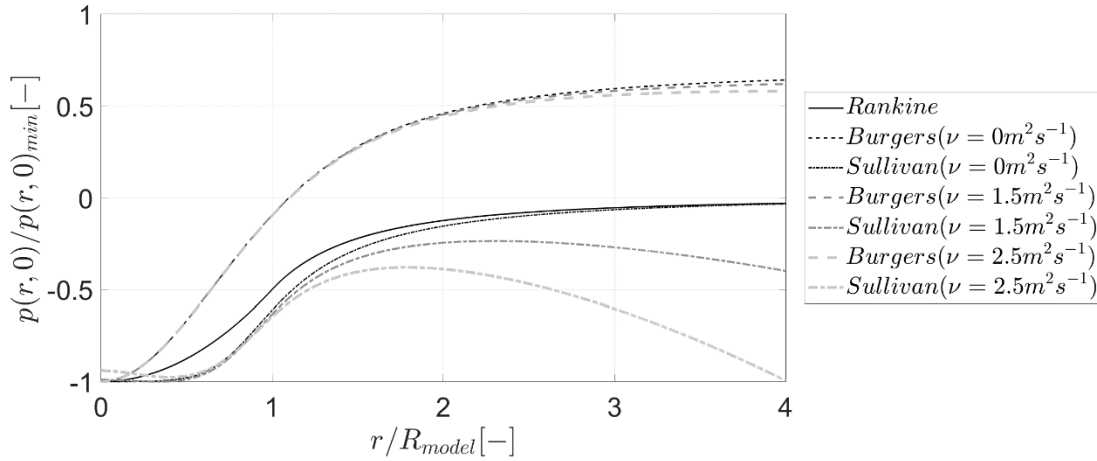
Figure 3.7: Surface pressure distribution of the Rankine, the Burgers-Rott and the Sullivan vortex model for different 'viscosity' values.

In order to enable a meaningful comparison of surface pressure distributions, the 'viscosity' parameter (v) and the 'vortex stretching' parameters ($\bar{a}$) need to be adjusted in the circumferential velocity distribution and the surface pressure distribution of the Burgers-Rott vortex model. This ensures that the increase in surface pressure with increasing radial distance of the Burgers-Rott vortex model is of similar order to the one of the Rankine and the Sullivan vortex model. Thus, equation (2.10) needs to be modified by means of the relation given in equation (2.8.1) in the following way (Eq. 3.2) to obtain a circumferential velocity distribution of the Burgers-Rott vortex model, which is dependent on v and $\bar{a}$.

$$\overline{u_\theta}(\bar{r}) = \frac{1}{\bar{r}}\left(1 - exp\left(-\frac{r\bar{a}\ u_{\theta,max}}{2v}\right)^2\right) \qquad (3.2)$$

Now, in order to ensure a physically reasonable surface pressure distribution, v and $\bar{a}$ need to be chosen independent from one another, which has the consequence that the input parameters, R and $u_{\theta,max}$ vary (see Eq. 2.8.1). Unquestionably, this is physically not consistent, but seems to be the only way for the Burgers-Rott vortex model to generate a physically meaningful surface pressure increase with increasing radial distance.

Figure 3.8 shows the surface pressure distribution for input parameters of $R = 10$m and $u_{\theta,max} = 10$m/s for the Rankine, the Burgers-Rott and the Sullivan vortex model. It is worth noting that the 'viscosity' and 'stretching' parameter differ for different input parameters. The two-celled structure of the Sullivan vortex model and hence, the decreased circumferential velocity component close to the vortex core result in a relatively flat pressure distribution close to the vortex centre (Figure 3.8). The surface pressure distribution of the Burgers-Rott vortex model increases at a faster rate close to the vortex centre due to a rapid increase of the circumferential velocity in this region (Figure 3.8). The largest differences in the surface pressure distribution of the vortex models can be found inside the vortex core ($r < R_{model}$) and for radial distances around $r/R_{model} = 1.5$. This arises due to the relative difference between the circumferential velocity profiles predicted by the analytical vortex models (Figure 3.1).
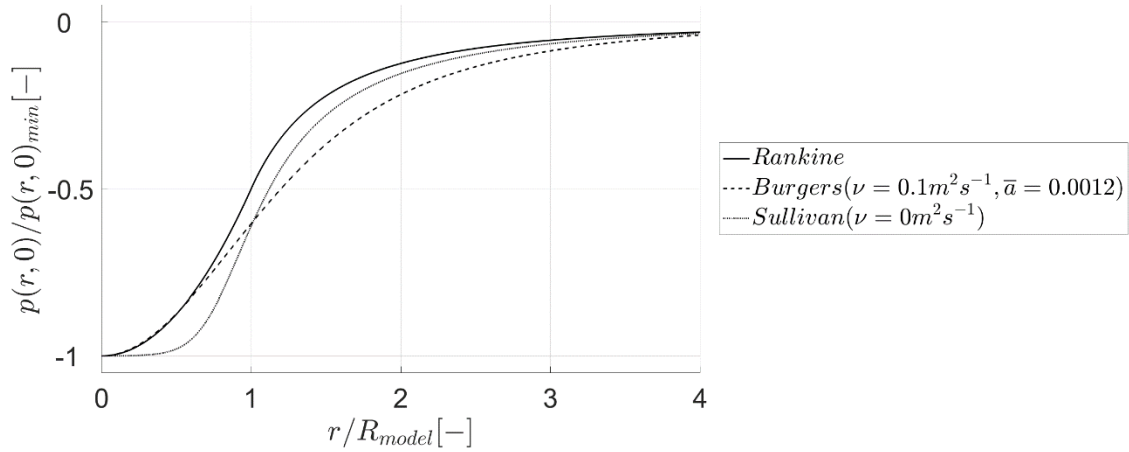
Figure 3.8: Surface pressure distribution of the Rankine, the adjusted Burgers-Rott and the Sullivan vortex model.

The static 'surface pressure' distribution and the effect of the swirl ratio on the shape of the distribution of the Baker vortex model is shown in figure 3.9. The 'surface pressure' distribution of the Baker vortex model falls to zero for $r \to \infty$; however, the 'surface pressure' minimum is not bounded for the Baker vortex model and decreases with increasing swirl ratio as shown in figure 3.9 from -1.99 $\rho u_r(r_m,z_m)^2 \text{Nm}^{-2}$ to -17.94 $\rho u_r(r_m,z_m)^2 \text{Nm}^{-2}$ for $S_{Baker} = 1$ to 3 due to the

term $-\dfrac{4.15 S_{Baker}{}^2 \left(ln\left(1+\bar{z}^2\right)\right)^2}{\left(1+\bar{r}^2\right)}$ (c.f. equation (2.19)). The effect of this on the 'surface pressure' distribution is masked in figure 3.9 due to normalising the pressure distribution additionally with $p(r,z_m)_{min}$ of the corresponding swirl ratio. This additional normalisation is applied to force all pressures to tend to -1 as r/R tends to 0. It is noted that some numerical and experimental data such as *Natarajan and Hangan (2012)* and *Haan et al. (2008)* show that the central surface pressure deficit decreases with increasing swirl ratio, which has been associated with a transition from a single-celled to a two-celled vortex as outlined in section 2.2. Although, the Baker vortex model in its two-celled form (*Baker and Sterling, 2017*) is able to represent this behaviour, for simplicity this is not incorporated here.
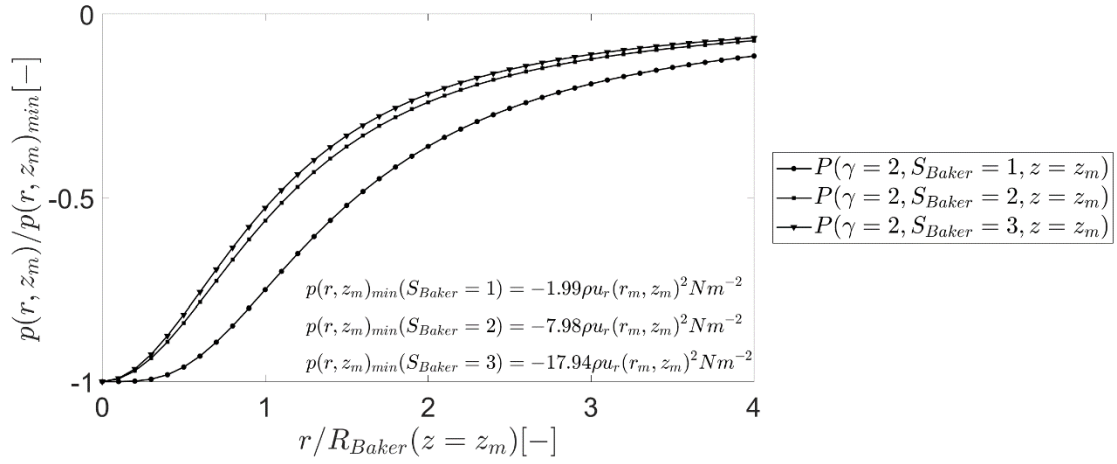
Figure 3.9: 'Surface pressure' distribution of the Baker vortex model for different swirl ratios (S_{Baker}).

The effect of the radial velocity profile on the 'surface pressure' (i.e., $-\dfrac{8\bar{r}^2\bar{z}}{(1+\bar{r}^2)^2(1+\bar{z}^2)^2}$, c.f. equation (2.19)) is largest at the core radius (R_{Baker}) since this is where the radial velocity attains its maximum for $\gamma = 2$. When this term is normalised by the value of $p(r,z_m)_{min}$ for each corresponding swirl ratio, its magnitude decreases with increasing S_{Baker}. As a consequence, figure 3.9 shows that with increasing S_{Baker}, the 'surface pressure' increases at a faster rate with increasing radial distance. It is noted that this is also an artefact of normalising radial distances with the core radius (R_{Baker}), which in the Baker vortex model is independent of S_{Baker} and therefore, remains constant even though the swirl ratio changes. The last term in equation (2.19) represents the effect of vertical advection of radial velocity on the 'surface pressure' distribution (i.e., $-\dfrac{4\ln(1+\bar{z}^2)(1-\bar{z}^2)}{(1+\bar{r}^2)^2(1+\bar{z}^2)^2}$). When $z = z_m$, this term reduces to zero.

3.2. A reflection on physical tornado-like vortex models

In this section, the physical simulation of tornado-like vortices is examined and is evaluated with respect to the geometric and dynamic similarity of the generated flow fields. Physical simulators based at the University of Western Ontario, Texas Tech, Iowa State and Purdue are examined because those simulators cover the variety of physical simulators that are currently used to assess tornado-like flow fields experimentally. All of those simulators are based on the principle introduced by *Ward (1972)*, i.e., a tornado-like wind is created by generating vorticity in the presence of a suction updraft (as outlined in section 2.5). For that reason, in addition to the previously mentioned simulators, the original Ward simulator (*Ward, 1972*) is presented. It is noted that physical tornado research is also conducted at other institutes; however, the design of their simulators is similar to either one of those, which will be presented in the following. For all simulators, the central suction updraft is introduced in a similar way; however, the way how vorticity is introduced to the generated flow fields differs.

3.2.1. Existing physical tornado-like vortex generators

A variety of large-scale (> 10m), medium-scale (1m - 5m) and small-scale (< 1m) physical tornado simulators have been built over the last years. The currently largest facility to generate tornado-like vortices is the large-scale WindEEE Dome at the University of Western Ontario (*Refan and Hangan, 2018*; Figure 3.10a). The large size of this facility is helpful in order to

simulate tornado-like vortices with a relatively large geometric scale. This is particularly important when detailed wind field measurements or wind load analyses are of interest because the spatial resolution of velocity / surface pressure measurements can increase with decreasing geometric scaling factor. Furthermore, assuming similar velocity magnitudes, a lower geometric scaling factor results in larger Reynolds numbers, still significantly lower than in the atmosphere, but more similar to full-scale tornadoes than in other simulators (*Refan and Hangan, 2018*).

In WindEEE, rotation is introduced by means of adjustable louvers, which are installed in front of fans surrounding the convergence chamber ($H_1 = 0.8$m, $D_1 = 25$m). The introduced vorticity is concentrated and stretched vertically in the convection chamber ($H_2 = 4$m, $D_2 = D_1$) by an updraft, which is generated by fans on top of a bell-mouth. It is at present unclear how the rotation and the associated flow disturbance introduced by the fans surrounding the convergence chamber affects the characteristics of generated vortices. To allow changes of the aspect ratio, the diameter of the bell mouth can be altered from $D_3 = 1.6$m - 4.5m. Furthermore, the generated vortex can be translated over a distance of 5m with a translation speed of up to 2m/s.

VorTECH is a large-scale tornado-like vortex simulator at Texas Tech University (*Tang et al., 2018*; Figure 3.10b). Fans on top generate a central updraft through an updraft hole ($D_3 = 4$m) and guide vanes surrounding the convergence chamber are used to introduce rotation. In order to minimise any possible unwanted flow disturbance, guide vanes have been designed based on the shape of an aerofoil (*Mayer, 2009*). The aspect ratio can be changed by moving the upper

cylinder ($H_2 \sim 4m$, $D_2 = 4m$) into the lower one ($D_1 = 10.2m$) and thereby changing H_1 from 1m to 2m.

TTU-VSII is a small-scale tornado-like vortex simulator at Texas Tech (Figure 3.10c) and is described in *Mishra et al. (2008a)*. A fan on top draws air through the simulator, generating an updraft through the updraft hole ($D_3 = 0.38m$), which is defined in-between the height-adjustable convergence chamber ($H_1 = 0.06m - 0.19m$) and the convection chamber. Rotation is introduced by means of slotted jets, equally spaced around the convergence chamber. A vortex blower is blowing air through the slotted jets; hence, circulation can be controlled independent from the updraft intensity. At present it is not known how the velocity of those jets and the associated flow disturbance affects the characteristics of generated vortices. A flow rectifier in front of the fan on top of the simulator removes any vorticity potentially introduced into the simulator's chamber.

The design and construction of the medium-scale tornado simulator at the Iowa State University (WIST, Figure 3.10d) is explained in *Haan et al. (2008)*. A rotating forced downdraft technique is used to introduce rotation to the flow field. This technique introduces rotation in greater heights by means of guide vanes in a pipe system, which guides the introduced rotation downwards to the simulator's inlet. This technique is supposed to replicate the potentially important role of the rear flank downdraft close to the surface when the tornado forms (*Haan et al., 2008*). However, the air transported through the guide vanes seems to be affected by the fan's rotation and thereby possibly affects the rotation introduced at the simulator's inlet. The potential effect of this on the generated vortex has not been investigated.

The simulator consists of a convergence region, which is adjustable in height ($H_1 \sim 0.23$m –
1.52m, $D_1 = 5.2$m) and a fixed convection region ($H_2 \sim 1$m, $D_2 \sim 4.9$m). The updraft diameter
(D_3) is 1.83m and a flow rectifier is installed at the outlet of the convection chamber to remove
vorticity introduced by the rotating fan. Similar to the design of the WindEEE simulator also
the design of WIST allows the simulation of translating vortices with a translation speed of up
to 0.61m/s for a distance of 3.35m along the ground plane.

In order to evaluate if simulated translation speeds in WindEEE and WIST are similar to what
has been observed in atmospheric tornadoes, an additional velocity ratio needs to be introduced.
In the following, the translation velocity is assessed in relation to the circumferential velocity
maximum of the corresponding vortex. Despite the large variability of circumferential velocity
maxima and translation speeds observed in atmospheric tornadoes, averaged values were found
to be roughly around 60m/s and 15m/s, respectively (*Alexander and Wurman, 2008*). In other
words, on average, the translation velocity of full-scale tornadoes is about four times smaller
than the circumferential velocity maxima. The design of WindEEE seems to allow the
simulation of translating vortices with a similar velocity ratio only for relatively low swirl ratios
(*Refan and Hangan, 2018*). In WIST, circumferential velocity maxima seem to be too large /
translation velocities are not large enough in order to comply with the atmospheric velocity
scales (*Haan et al., 2008*). Therefore, it is questionable if the simulated translation has a similar
effect on the generated vortex than what is found in full-scale.

Another medium-scale simulator was developed at Purdue University (*Church et al., 1977*;
Figure 3.10e). It introduces rotation by means of a rotating mesh screen surrounding the
convergence chamber, which is adjustable in height ($H_1 = 0.17$m – 0.61m, $D_1 = 3.04$m).

Introduced vorticity is concentrated and stretched vertically by a fan on top of the convection chamber ($H_2 \sim 1.66$m, $D_2 = 2.84$m). A flow rectifier on top is used to remove any unwanted vorticity introduced by the fan. The updraft hole is defined between the convergence and convection chamber and has an adjustable diameter of $D_3 = 0.40$m – 1.22m.

The design of the simulator at Purdue University is very similar to the original medium-scale simulator introduced by *Ward (1972)* (Figure 3.10f). The general working principle of the Ward tornado-like vortex generator is outlined in section 2.5. In the following, relevant additional information is provided. The convection chamber has a diameter of 1.83m (D_2) and a height of 0.92m (H_2). The convergence region is 2.44m wide (D_1). The aspect ratio can be varied by changing the height of the convergence chamber (H_1) from 0.31m to 0.61m and the updraft radius (D_3) from 0.62m – 1.24m (*Jischke and Parang, 1974*).
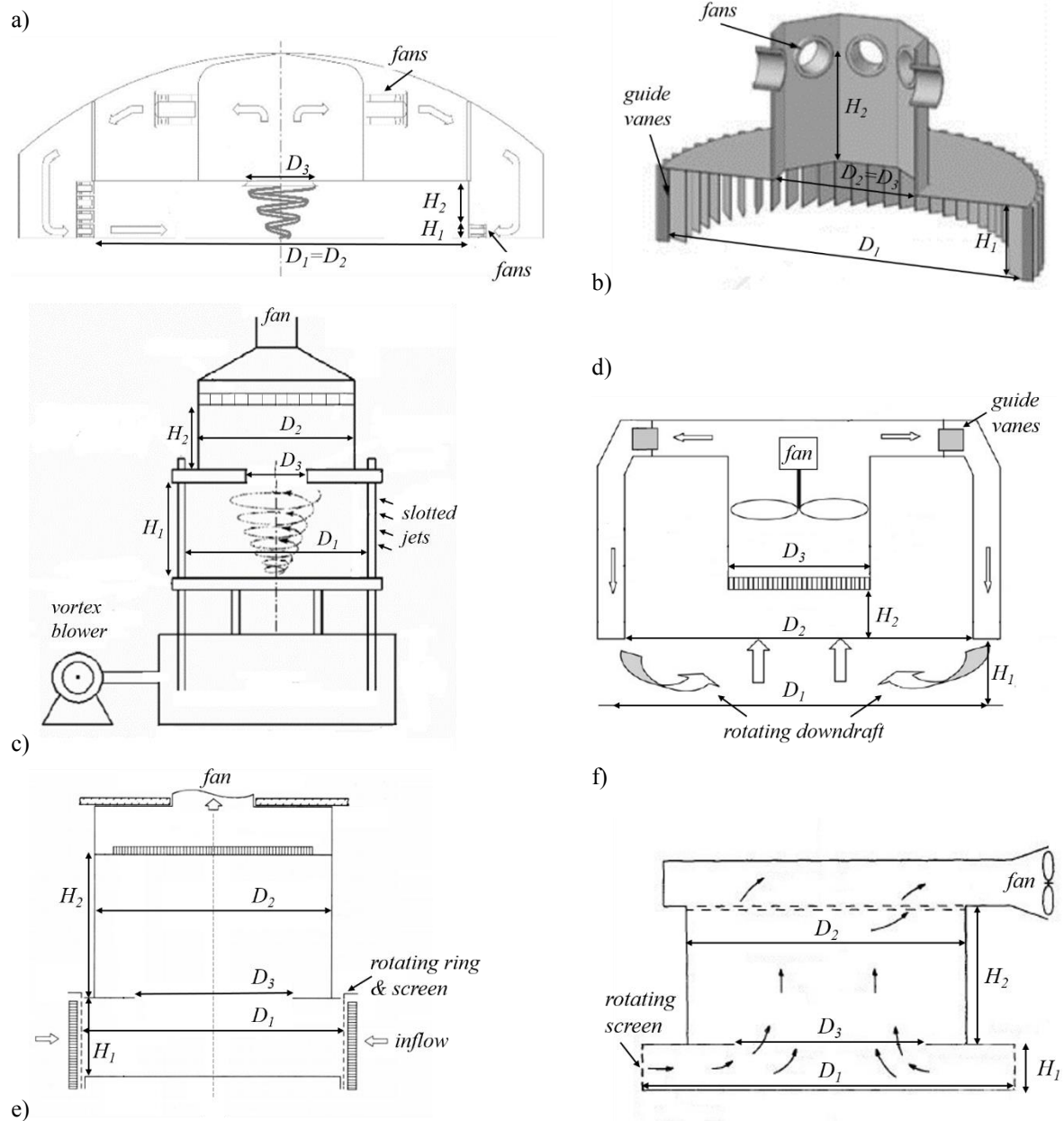
Figure 3.10: Illustration of existing physical tornado-like vortex generators. WindEEE and VorTECH are shown in a) and b), respectively, whereas, TTU-VSII, WIST and Purdue are illustrated in c), d) and e). The original Ward simulator is illustrated in f). Corresponding illustrations have been adapted from corresponding references referred to in the text.

One of the biggest differences between the updraft generation in different simulators seems to be the axis alignment of fans, which is horizontal in WindEEE and VorTECH (Figure 3.10a and 3.10b) and vertical in TTU-VSII, WIST and Purdue (Figure 3.10c -3.10e). In the Ward simulator, a single fan with horizontal axis is responsible for the vertical air movement (Figure

3.10f). This design is assumed to represent an overlying straight-line cross flow (*Church et al., 1979*) and therefore, potentially simulates conditions similar to what might prevail at the top of atmospheric tornadoes (*Ward, 1972*). As a result, the generated pressure deficit on top of the convection chamber is not uniform and therefore, the flow is encouraged to move towards the direction of the fan as illustrated in figure 3.10f. With a design like this, it is suggested that simulated vortex characteristics might depend significantly on H_2 as this length defines the distance between the non-uniform pressure deficit and the generated vortex.

The design and arrangement of the fan or fans in other simulators (Figure 3.10a-3.10e) suggests the intention of the generation of a uniform pressure deficit across the top of the convection chamber. This would consequently result in a uniform flow updraft. However, a potential problem arising for fans with horizontal axis alignment could be that the generated surface pressure deficit is not uniformly distributed and instead largest pressure deficits are potentially sifted towards the individual location of fans, which in turn would result in a slightly tilted updraft, directed towards the fans.

In view of the relatively different geometric designs of those simulators, it is surprising how little information there is concerning the design's impact on the generated flow field. An important question to ask is whether vortices simulated in different simulators can be compared. In order to reflect on this question, the geometric similarity between introduced simulators will be discussed in detail in the following section.

3.2.2.   Geometric similarity

None of the previously introduced tornado simulators have the same design or controlling geometric boundary conditions, which consequently leads to differences in their non-dimensional parameters. For that reason, a meaningful comparison of results obtained in different simulators is challenging. Table 3.2 illustrates values / ranges of non-dimensional geometric parameters introduced in table 2.2 for the presented simulators.

Table 3.2: Geometric non-dimensional relations for WindEEE, VorTECH, TTU-VSII, WIST, Purdue and Ward.

	H_1/H_2	$H_1/\frac{1}{2}D_1$	$H_1/\frac{1}{2}D_2$	a	$H_2/\frac{1}{2}D_1$	$H_2/\frac{1}{2}D_2$	$H_2/\frac{1}{2}D_3$	$\frac{1}{2}D_1/\frac{1}{2}D_2$	$\frac{1}{2}D_1/\frac{1}{2}D_3$	$\frac{1}{2}D_2/\frac{1}{2}D_3$
WindEEE	0.2	0.1	0.1	0.4 – 1.0	0.3	0.3	1.8 – 5.0	1.0	5.0 - 15.6	5.0 - 15.6
VorTECH	0.3 – 0.5	0.2 – 0.4	0.5 – 1.0	0.5 – 1.0	0.8	2.0	2.0	2.6	2.6	1.0
TTU-VSII	-	-	-	0.3 – 1.0	-	-	-	-	-	-
WIST	0.2 – 1.5	0.1 – 0.6	0.1 – 0.6	0.3 – 1.7	0.4	0.4	1.1	1.1	2.8	2.7
Purdue	0.1 – 0.4	0.1 – 0.4	0.1 – 0.4	0.3 – 3.1	1.1	1.2	2.7 - 8.3	1.1	2.5 – 7.6	2.3 – 7.1
Ward	0.3 – 0.7	0.3 - 0.5	0.3 – 0.7	0.5 – 2.0	0.8	1.0	1.5 – 3.0	1.3	2.0 – 3.9	1.5 – 3.0

Ward (1972) showed that the generated vortex structure can depend on the aspect ratio, *a*. Maybe for that reason, the aspect ratio is the geometric relation, which received most attention when designing physical tornado-like vortex simulators. The design of all simulators presented in table 3.2 allows the simulation of vortices with a similar aspect ratios ($0.5 < a < 1$), whereas values of other geometric relations are widely spread and the effect of those geometric differences on the generated vortex flow field are to date largely unknown. In all simulators,

the aspect ratio can either be varied by changing the convergence chamber height (e.g., VorTECH, TTU-VSII and WIST) or the updraft diameter (e.g., WindEEE). Solely, the design of the simulator at Purdue University and the Ward simulator allow individual changes of both length scales and thereby enable the simulation of vortices with a relatively large aspect ratio range (Table 3.2).

It also needs to be noted that the location of the updraft radius (D_3) is defined at different locations in different simulators. For example, if the design of the simulator includes a surface between convergence and convection chamber, D_3 is defined at the surface opening. This is the case for TTU-VSII (Figure 3.10c), Purdue (Figure 3.10e) and the Ward simulator (Figure 3.10f). For other simulators, the updraft diameter is defined as the diameter at the outlet on top of the convection chamber (e.g., WindEEE, Figures 3.10a; VorTECH, Figures 3.10b and WIST, Figures 3.10d). This highlights the necessity of clarifying specific requirements for the simulation of vortices, which are supposed to be geometrically similar. A uniform definition for the location of geometric parameters is required to make results obtained in different simulators comparable. Relatively large differences in the geometric design of different simulators (Table 3.2) give reason to discuss if similar flow characteristics can be generated in those geometrically different simulators.

The intention of the simulator designed by *Ward (1972)* was to simulate the sub-cloud inflow layer in the lowest chamber and convective processes in a thunderstorm in the top chamber. The chambers are separated by a surface, which prevents convection from outside the central updraft region and acts similar to a stable layer of air in the atmosphere (*Church et al., 1979*). However, as outlined in section 2.1, significant vertical motion occurs everywhere in a

thunderstorm. Therefore, stable atmospheric conditions as proposed by *Ward (1972)* do not exist at this location in the thunderstorm. For simulators without this surface the question arises, if a convection chamber is essential for the simulation of tornado-like vortices or if it is enough to 'simply' provide a pressure deficit on top of the convergence chamber? (This question is formally addressed in section 6.3.2).

Furthermore, it was noted in section 2.5.1 that there are more geometric length scales in those physical tornado-like vortex generators, which could potentially have an effect on the simulated flow field. For instance, another open question is whether the shape and number of guide vanes affect the simulated flow field. Appendix A briefly addresses the latter. Findings presented in appendix A suggest that in addition to quantifiable geometric differences illustrated in table 3.2, it also seems likely that the chosen way of mechanically introducing rotation to the flow may potentially affect the flow structure of the generated vortices. For instance, *Zuh et al. (2016)* analysed the effect of the rotating downdraft on the flow field by comparing simulations conducted in WIST with simulations conducted in a simulator based on the design introduced by *Ward (1972)* and found out that dynamic vortex structures depend significantly on the way of how rotation is introduced to the flow field.

3.2.3.   Dynamic similarity

As outlined by *Davies-Jones (1973)* and discussed in previous sections, the flow field is also a function of the swirl ratio, *S*, and the Reynolds number, *Re*. Table 3.3 shows the definition of Reynolds numbers and swirl ratios used to describe the dynamic non-dimensional properties of

simulations conducted in the previously introduced physical tornado simulators. Although, the swirl ratio is acknowledged as an important parameter for the characterisation of tornado-like flow field structures, its definition is based on the simulator's design and therefore, is dependent on the specific geometric configuration of the corresponding simulator (*Refan and Hangan, 2016*).

Table 3.3: Definitions of Reynolds numbers and swirl ratios for WindEEE, VorTECH, TTU-VSII, WIST, Purdue and Ward.

Simulator	Reference	Re	S
WindEEE	Refan and Hangan (2016 and 2018)	$Re = \dfrac{Q_{outlet}}{2\pi H_1 \nu}$	$S = \dfrac{\Gamma_{max} \frac{1}{2} D_3}{2 Q_{outlet}} =$
VorTECH	Tang et al. (2018)	$Re = \dfrac{Q_{r=\frac{1}{2}D_3}}{2\pi H_1 \nu}$	$S = \dfrac{\Gamma_{r=\frac{1}{2}D_3} \frac{1}{2} D_3}{2 Q_{r=\frac{1}{2}D_3}}$
TTU-VSII	Mishra et al. (2008a)	-	$S = \dfrac{u_\theta(r,z)}{2a\, u_r(r,z)}$
WIST	Haan et al. (2008 and 2017)	$Re = \dfrac{Q_{outlet}}{2\pi H_1 \nu}$	$S = \dfrac{\Gamma_{max} R}{2 Q_{outlet}}$
Purdue	Church et al. (1977 and 1979)	$Re = \dfrac{Q_{inlet}}{2\pi H_1 \nu}$	$S = \dfrac{\Gamma_{inlet} \frac{1}{2} D_3}{2 Q_{inlet}} = \dfrac{u_{\theta,inlet}}{2a\, u_{r,inlet}} = \dfrac{tan(\alpha)}{2a}$
Ward	Jischke and Parang (1974)	-	$S = tan(\alpha)$

Reynolds numbers and swirl ratios defined in table 3.3 are based on equations (2.21) and (2.22), respectively; however, slightly different definitions are adopted for each simulator. Differences in formulae largely originate from different measurement locations in those simulators to estimate the flow rate through the simulator, Q, and the circulation at a certain radial distance, Γ. However, generated vortices in different simulators can only reveal similar flow characteristics if swirl ratios are similar and have been defined in the same way. In return, this means that vortices simulated in different simulators can reveal completely different flow structures even though swirl ratios are identical. To the best of the author's knowledge, this

important result has hitherto not been formally acknowledged. This can result in the transition of flow characteristics from, e.g., a single-celled vortex to a two-celled vortex, to occur at significantly different swirl ratio values. *Liu and Ishihara (2012)* showed that swirl ratios obtained for the same vortex can differ by a factor of 3.6 if swirl ratios are defined at different locations in the flow field. This highlights how important it is to document in detail, not only the geometric design of the simulator, but also the methodology how Γ and Q are estimated in the flow field in order to allow a reasonable comparison between vortices generated in different simulators.

Keeping differences arising due to different flow rate definitions aside, swirl ratios presented in table 3.3 differ because of different radial distances from the vortex centre at which the circulation is estimated. Large differences in the circulation can be expected for different radial distances due to a strong dependence of the circumferential velocity component on the radial distance. Therefore, the swirl ratio is strongly dependent on the radial distance from the vortex centre. In order to form a non-dimensional parameter with Q and Γ, the circulation needs to be multiplied with a geometric length scale. It is noted that any geometric length scale in the simulator could have been chosen in the numerator of the swirl ratio. At Purdue and in VorTECH, D_3 was chosen in order to include the aspect ratio in the definition of the swirl ratio. Evaluating the swirl ratio defined by *Tang et al. (2018)* at any radial / vertical position in the simulator, the equation given by *Mishra et al. (2008a)* is obtained. If the swirl ratio is defined at the circumference of the convergence chamber, the equation given in *Mishra et al. (2008a)* transforms into the equation provided by *Church et al. (1977)* and the guide vane angle relative to the radial direction can be used instead of the ratio of circumferential to radial velocity component (*Davies-Jones, 1973*). A similar approach is followed in the Ward simulator where

a wind vane, installed at the simulator's inlet, is used in order to evaluate the horizontal inflow angle (α) and therefore, the swirl ratio.

In WindEEE and WIST, the circulation is defined at the position where the circumferential velocity component attains its maximum (Γ_{max}). This introduces a new vortex dependent length scale to the swirl ratio – the vortex core radius, R, which is not necessarily needed to guarantee geometric / dynamic similarity. There are circumstances where a definition based on the core radius is of benefit, for instance, when a comparison to atmospheric tornadoes is of interest, as the core radius is a parameter, which can at least be measured / estimated in an atmospheric vortex, whereas the equivalent for corresponding simulator length scales may not be that straightforward to determine. However, with the flow rate being defined at the updraft hole, swirl ratios in WindEEE and WIST become also dependent on D_3.

All of the above highlights how strongly the swirl ratio depends on the geometric design of the corresponding simulator. Therefore, flow field similitude of vortices simulated in different physical tornado-like vortex simulators can only be achieved if geometric and dynamic similarity is guaranteed. This is not possible for any of the previously introduced simulators.

Furthermore, it is noted that the circulation is not only dependent on the radial distance, but also the height, which raises the question of how representative the definition of the swirl ratio based on a single measurement position is in order to guarantee dynamic similarity between two flow systems?

Swirl ratios of some flow fields simulated for this work are calculated in appendix B and associated challenges are discussed in detail.

Differences in the definition of Reynolds numbers presented in table 3.3 originate from differences in the location where measurements were taken in order to estimate the flow rate through the system. In WindEEE and WIST for example, the flow rate is estimated by a spatial average of vertical velocities through the updraft hole, whereas in VorTECH, an estimation of the flow rate is provided by a height average of radial velocity components in the convergence chamber at a radial distance equal to the radius of the updraft hole ($r = \frac{1}{2}D_3$). At Purdue, the flow rate was estimated by measuring the radial inflow velocity at the circumference of the convergence chamber.

In theory, the flow rate through the system is assumed to be constant due to mass conservation and therefore, in theory, should be independent from the measurement position in the simulator (assuming that no losses occur); however, *Zhang and Sarkar (2012)* observed a decrease in flow rate with increasing swirl ratio, which gives reason to suggests that friction losses occur somewhere between the fan and the measurement position. Therefore, positions where measurements are taken to estimate Q need to be chosen wisely and documented precisely. A potentially complex interaction between the fans introducing vorticity and the fans generating the suction updraft may be expected for those simulators where two forcing mechanisms are installed (e.g., WindEEE, TTU-VSII and Purdue). In those simulators, estimations of the flow rate might depend even more on the measurement location than in other simulators with only one forcing mechanism. Furthermore, it is noted that instead of H_1 in the denominator of the

Reynolds number (Table 3.3), any length scale in the simulator could have been chosen in order to form a non-dimensional Reynolds number.

3.2.4. *Full-scale equivalents to geometric and dynamic model parameters*

In order to reproduce full-scale tornado flows in a geometrically scaled physical simulator, geometric and dynamic similarity needs to be ensured in order to draw meaningful conclusions from model results. However, it is extremely difficult to define equivalent length scales, a flow rate and circulation that are representative to naturally occurring tornadoes. Nevertheless, *Church et al. (1979)* published 'typical' values for the required parameters, which are 'most likely' to occur (Table 3.4a and 3.4b). The expressions 'typical' and 'most likely' are misleading given the high variability in naturally occurring tornadoes. Table 3.4c illustrates the possible atmospheric range of non-dimensional geometric relations introduced in table 2.2 based on values presented in table 3.4a, assuming that either smallest values or largest values occur together, whilst figure 3.11 shows an attempt to illustrate the approximate corresponding locations of geometric length scales in a full-scale tornado / thunderstorm. It is acknowledged that the scaling in figure 3.11 is highly subjective.

Table 3.4: Typical geometric (a) and dynamic scales (b) and geometric relations (c) of atmospheric tornadoes.

a)

geometric scales (Church et al., 1979)	length [km]
H_1	0.5-2
H_2	5-16
D_1	10-20
D_2	6-12
D_3	2-6

b)

dynamic scales (Church et al., 1979)	[-]
Re	$10^9\text{-}10^{11}$
S	0.05-2

c)

H_1/H_2	$H_1/\frac{1}{2}D_1$	$H_1/\frac{1}{2}D_2$	a	$H_2/\frac{1}{2}D_1$	$H_2/\frac{1}{2}D_2$	$H_2/\frac{1}{2}D_3$	$\frac{1}{2}D_1/\frac{1}{2}D_2$	$\frac{1}{2}D_1/\frac{1}{2}D_3$	$\frac{1}{2}D_2/\frac{1}{2}D_3$
0.1	0.1 – 0.2	0.2 – 0.3	0.5-0.7	1.0 – 1.6	1.7 – 2.7	5.0 – 5.3	1.7	3.3 – 5.0	2.0 – 3.0
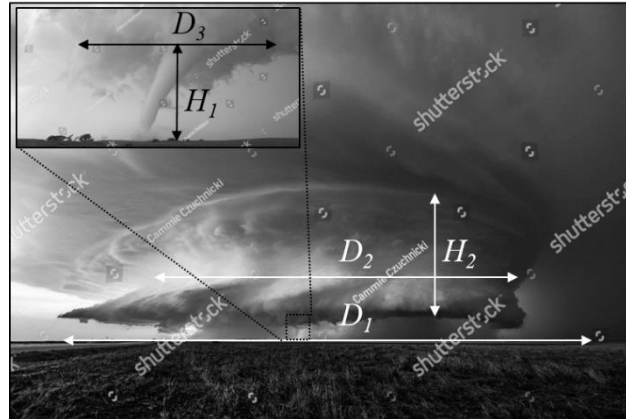
Figure 3.11: Illustration of a supercell storm in Kansas, *US* and a tornado in Colorado, *US*. In addition, potential locations of corresponding geometric length scales are illustrated. Pictures were taken by Cammie Czuchnicki and Justin Hobson and are adapted from *shutterstock image ID 470220380 and 303480896*, respectively.

3.2.4.1.   Geometric similarity and scaling

In order to match the atmospheric ratios given by *Church et al. (1979)*, H_2 needs to be approximately 6.7, 0.6, 0.7 and 2 times larger than H_1, D_1, D_2, and D_3, respectively. In a small

or medium-scale physical simulator, this is only feasible if H_1, and D_3 are relatively small. If those parameters are relatively small, this also means that the generated vortex is likely to be of relatively small size, which consequently results in a relatively large geometric scaling factor in the order of 1000 - 5000, which is about an order of magnitude larger than what is usually used in wind tunnel simulations. For that reason, in most physical simulators ratios related to H_2 are out of range and consequently, most simulators underestimate the extent of H_2 given by *Church et al. (1979)* (Table 3.2 and Table 3.4c).

Due to challenges in determining full-scale geometric parameters and the unlikelihood of all geometric parameters in a physical simulator scaling up to a specific atmospheric tornado, the core radius, R, is frequently used to geometrically scale the flow field (e.g., *Hangan and Kim, 2008*; *Mishra et al., 2008a*; *Haan et al., 2008*; *Zhang and Sarkar, 2012*; *Sarkar et al., 2014*; *Refan et al., 2014* and *Refan and Hangan, 2018*). By using the core radius to normalise radial and vertical distances, it is assumed that R is a function of all other geometric lengths scales in a simulator. However, it is noted that geometric similarity as defined by *Davies-Jones (1973)* is not guaranteed in those simulations. Nevertheless, those simulations have demonstrated that it is possible to generate vortices that appear to possess some similar characteristics to those found in atmospheric tornadoes.

Hangan and Kim (2008) introduced a geometric scaling method based on two length scales closely related to the flow field of the tornado – the core radius, R, and height, Z, which are defined at the radial distance and height from the vortex centre where the circumferential velocity component attains its overall (global) maximum. This approach has the advantage of relying on parameters, which could theoretically be measured in real tornadoes; however,

determining R and Z is not without difficulties because a detailed knowledge of a significant component of the flow field is required in order to determine the overall velocity maximum and typically, in full-scale tornadoes, only a couple of heights are measured. Hence, uncertainties in the definition of R and Z are difficult to quantify, but are reflected in the geometric scale. Furthermore, *Alexander and Wurman (2008)* highlighted a relatively large uncertainty associated with the measurement height of mobile Doppler radar data, which introduces an additional uncertainty to those values. Especially for wind load analyses, an accurate representation of the geometric scaling factor is crucial, as it has to match both, the geometric scale of the tornado and the geometric scale of the modelled structure. When the size of the core radius of naturally occurring tornadoes is used to geometrically scale the modelled flow structure, large geometric scaling factor between 1550 and 5000 are obtained (e.g., *Mishra et al., 2008a and 2008b*; *Yang et al., 2011* and *Refan et al., 2014*). The large geometric scaling factor makes it impossible to measure wind loads on common size houses as the model equivalent to a full-scale structure of approximately $10 \times 10 \times 10$ metres would only be about $4 \times 4 \times 4$ millimetres in the simulator. This small size makes a sensible assessment of the wind field around the structure and wind loads on the structure impossible. A different scaling approach was adapted by *Haan et al. (2008 and 2010), Hu et al. (2011), Sabareesh et al. (2012 and 2013a)* and *Case et al. (2014)*. In this approach, the size of the simulated vortex core is used to geometrically up-scaled the simulated flow field to a hypothetical atmospheric tornado, assuming a more reasonable geometric scaling factor of ~100. The problem with this approach is that it potentially leads to the simulation of hypothetical atmospheric vortices, which are relatively small.

In order to allow the simulation of tornado-like vortices with a more acceptable geometric scale, larger testing facilities have been built in recent years. In the currently largest physical tornado-like vortex simulator – the WindEEE Dome at the University of Western Ontario, tornado-like vortices of approximately 4.5m width and 4m height can be simulated (*Refan and Hangan, 2018*). This leads to geometric scaling factors of approximately $10 - 100$ for atmospheric vortices with core radii between 45m - 450m.

The geometric scale of some simulations conducted for this work and associated challenges are addressed in detail in appendix C.

3.2.4.2.   Dynamic similarity

Particularly challenging is also the definition of a full-scale swirl ratio (Table 3.4b) because extensive information of the flow field is required in order to estimate the flow rate and circulation in a similar way to how it is done in physical simulators. Different to modelled tornado-like vortices, those parameters can change drastically within the lifetime of a tornado because of its transient and unsteady nature. With respect to different swirl ratio definitions presented in table 3.3, defining the circulation and flow rate at the core radius would allow a swirl ratio definition based on a parameter, which can at least be measured in atmospheric tornadoes.

The combination of geometric and dynamic differences between model-scale and full-scale is reflected in the Reynolds number. According the *Church et al. (1979)*, the atmospheric Reynolds number is approximately in the order of $10^9 - 10^{11}$ (Table 3.4b), whereas model

Reynolds numbers are roughly in the order of 10^4 - 10^6 (e.g., *Refan and Hangan, 2018*). This once more highlights the Reynolds number issue addressed in section 2.5.1.

In addition to the geometric and dynamic similarity as defined by *Davies-Jones (1973)*, it is noted that parameters such as surface roughness and the tornado's translation speed strongly influence the near surface flow field (e.g., *Lewellen et al., 2000*; *Sarkar et al., 2006*; *Sengupta et al., 2008*; *Dessens, 1971*; *Leslie, 1977*; *Monji and Yunkuan, 1989*; *Natarajan and Hangan, 2012* and *Sabareesh et al., 2012 and 2013b*).

3.3. The research gap

In recent years, analytical calculations and physical simulations have been undertaken in order to analyse tornado flow fields. With the variety of atmospheric conditions present in real tornadoes, it is not surprising that physical tornado generators with different geometric designs have been built. Due to the limited amount of full-scale data available for validation, but also due to the limitations associated with existing full-scale data sets, evaluating the performance of those models is difficult. Maybe for that reason, it has tended to been forgotten that results obtained from simplified models are restricted by their assumptions and controlling boundary conditions. In order to recall this dependence in the context of tornado research, this work critically reviews the assumptions made in order to model tornadoes analytically and experimentally. A critical comparison of results obtained from both modelling techniques is shown in section 5 and the extent to which experimental results depend on certain geometric specifications of the simulator is presented in section 6.

4. *EXPERIMENTAL TORNADO SIMULATION AT UoB*

It is noted that parts of section 4.1 and 4.3 have been published in *Gillmeier et al. (2016 and 2018)*. Different normalisation methods (section 4.2) have been presented by the author in *Gillmeier et al. (2016)* and the majority of section 4.4 has been published in *Gillmeier et al. (2018)*. For all cases, the work is reproduced with the permission of the authors.

4.1. Physical tornado simulators

Two tornado-like vortex simulators of different size have been built at the University of Birmingham (*UoB*). The medium-scale simulator, hereafter referred to as *M1*, is illustrated in figure 4.1a and has an approximate size of 3m × 3m. The small-scale simulator, hereafter referred to as *S1*, is illustrated in figure 4.1b and is approximately 1m × 1m. Both simulators are based on the design introduced by *Ward (1972)*. The geometric design of both simulators results in an aspect ratio of $a = 2$, although, it is noted that other relative sizes are not constant (Table 4.1). In addition, similar to the geometric design of the simulators introduced in section 3.2.1, the length of the convection chamber (H_2) is underestimated compared to its 'typical' atmospheric length provided by *Church et al. (1979)* (Table 3.4a). Furthermore, it is highlighted

that the aspect ratio is relatively large compared to the previously introduced simulators (Table 4.1). Only the design of the simulator at Purdue University and the Ward simulator allow the simulation of tornado-like vortices with a similar aspect ratio (Table 3.2).
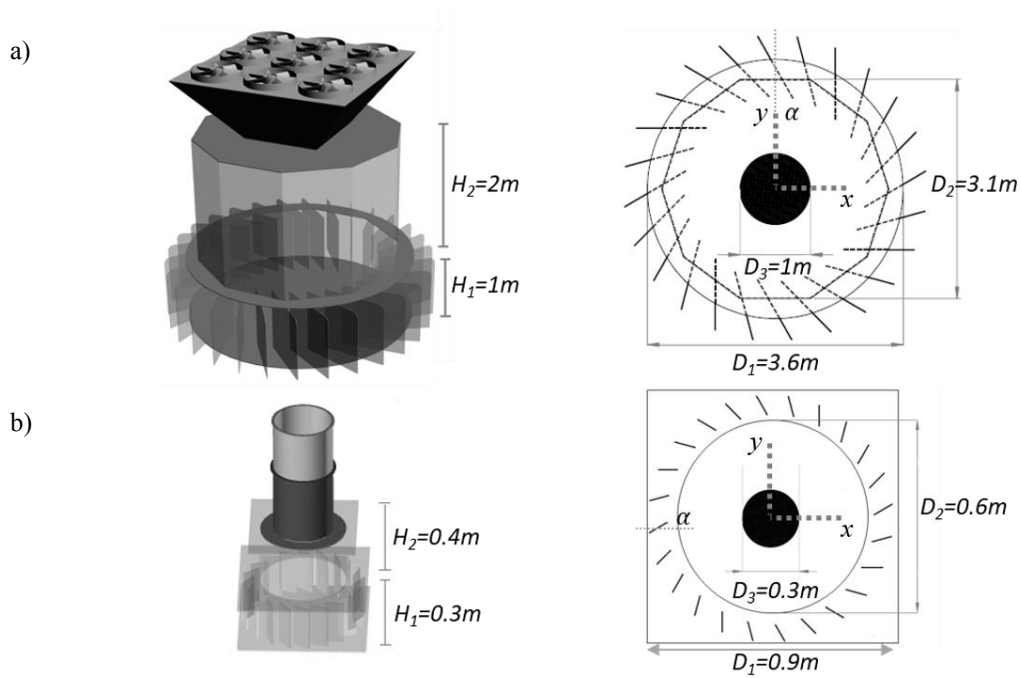
Figure 4.1: An illustration of the medium-scale (*M1*) (a) and small-scale (*S1*) (b) tornado-like vortex generator at *UoB*.

In order to analyse the effect of certain geometric parameters on the generated vortex flow characteristics, the design of simulator *S1* was modified in the following way:

- The convection chamber height (H_2) was reduced from $H_2 = 0.40$m (*S1*) to $H_2 = 0.25$m (*S2*) to $H_2 = 0.10$m (*S3*), whilst all other geometric lengths were kept constant.

- The convergence chamber height (H_1) was reduced from $H_1 = 0.30$m (*S1*) to $H_1 = 0.225$m (*S4*), whilst all other geometric lengths were kept constant. The reduction of H_1 results in an aspect ratio of 1.5 in *S4*.

Corresponding geometric length scales for simulators *S2*, *S3* and *S4* are proved in table 4.1.

Table 4.1: Geometric non-dimensional relations of the medium-scale simulator *M1* and the small-scale simulators *S1 − S4*.

	H_1/H_2	$H_1/\frac{1}{2}D_1$	$H_1/\frac{1}{2}D_2$	a	$H_2/\frac{1}{2}D_1$	$H_2/\frac{1}{2}D_2$	$H_2/\frac{1}{2}D_3$	$\frac{1}{2}D_1/\frac{1}{2}D_2$	$\frac{1}{2}D_1/\frac{1}{2}D_3$	$\frac{1}{2}D_2/\frac{1}{2}D_3$
M1	0.5	0.6	0.7	2.0	1.1	1.3	4.0	1.2	3.6	3.1
S1	0.8	0.7	1.0	2.0	0.9	1.3	2.7	1.5	3.0	2.0
S2	1.2	0.7	1.0	2.0	0.6	0.8	1.7	1.5	3.0	2.0
S3	3.0	0.7	1.0	2.0	0.2	0.3	0.7	1.5	3.0	2.0
S4	0.6	0.5	0.8	1.5	0.9	1.3	2.7	1.5	3.0	2.0

As outlined in section 2.5.1, the dynamic similarity of simulated vortices is controlled by the Reynolds number, *Re*, and the swirl ratio, *S*. In this work, the following definitions have been adopted for the Reynolds number (Eq. 4.1) and the swirl ratio (Eq. 4.2), respectively.

$$Re = \frac{2Q}{\nu D_3} \tag{4.1}$$

$$S = \frac{tan(\alpha)}{2a} \tag{4.2}$$

The diameter of the updraft hole was chosen as geometric length scale in the denominator of equation (4.1) because the flow rate was estimated at the updraft hole (Eq. 4.3). Therefore, the updraft radius is assumed to be the most characteristic length scale to determine the Reynolds number.

$$Q = \pi \left(\frac{1}{2}D_3\right)^2 u_{z,outlet} \tag{4.3}$$

where, $u_{z,outlet}$ was calculated based on a spatial average of velocity measurements taken across the diameter of the updraft hole (D_3).

Whilst it is acknowledged that a number of definitions exist for the swirl ratio, equation (4.2) is adopted in this research since it is the version, which has been widely used in 'Ward-type' simulators and thus is helpful in undertaking relative comparisons between such simulators. For the sake of completeness, values of swirl ratios defined at different locations in the flow fields measured in $M1$ and $S1$ are presented and briefly discussed in appendix B.

For this work, velocity and surface pressure fields have been measured for three vortices of different swirl ratio (i.e., $S = 0.14$, $S = 0.30$ and $S = 0.69$) in simulator $M1$ and $S1$, and for two vortices of different swirl ratio (i.e., $S = 0.30$ and $S = 0.69$) in simulator $S2$, $S3$ and $S4$.

4.2. Normalisation of results

It has been shown in section 2.5.1 that the flow field in a tornado-simulator depends amongst other parameters on the flow rate through the simulator. For that reason, the obtained results have to be normalised in order to allow a reasonable comparison between flow structures obtained in different simulators. Normalised results show the behaviour of a certain measured quantity in relation to a chosen parameter by forming a non-dimensional ratio. The parameter chosen for the normalisation needs to be sensitive to the normalised quantity and vice versa. Typically, in tornado research, surface pressures, velocity components and radial / vertical

distances are normalised by the minimum pressure (p_{min}), the maximum circumferential velocity ($u_{\theta,max}$) and the core radius (R), respectively. This approach was also followed in this work.

By adopting p_{min}, $u_{\theta,max}$ and R for the normalisation it is assumed that those parameters are functions of dynamic and geometric parameters identified in section 2.5.1. A benefit of using those parameters is that they can be determined in simulated vortices and atmospheric vortices supposedly with a higher accuracy than the flow rate and other geometric length scales. However, this does not mean that the determination of $u_{\theta,max}$ and R is straightforward. For example, a 'global' definition of R (R_{global}) and $u_{\theta,max}$ ($u_{\theta,max,global}$) can be used. These 'global' values correspond to the radial distance from the vortex centre up to the position where the overall circumferential velocity maximum occurs. An alternative approach is to focus on 'local' values, i.e., core radii and circumferential velocity maxima at each measurement height can be determined as the radial distance from the vortex centre to the position where the circumferential velocity maximum at each height occurs (R_{local} and $u_{\theta,max,local}$). The difficulty in using 'global' parameters is the strong dependence on the chosen measurement location (as has been demonstrated in appendix C), whereas 'local' values only provide a good representation of the core radius at each height (which can vary significantly depending on vertical elevation).

A compromise between the two approaches is to use 'averaged' quantities for R and $u_{\theta,max}$, as defined in equation (4.4) and (4.5), respectively.

$$R_{average} = \frac{1}{N}\sum_{i=1}^{N} R_{local_i} \qquad (4.4)$$

$$u_{\theta,max,average} = \frac{1}{N}\sum_{i=1}^{N} u_{\theta,max,local_i} \qquad\qquad (4.5)$$

where, N is the number of measurement heights in the corresponding simulator.

However, this approach still requires a detailed knowledge of a significant component of the flow field. An alternative approach is to calculate R based on the cyclostrophic equation (Eq. 2.5), thus eliminating the need for any velocity data. Based on equation (2.5), $R_{cyclostrophic}$ can be considered to be given by the location where the radial pressure gradient is the largest. However, the estimation of $R_{cyclostrophic}$ is not without its own challenges since a fine resolution of pressure measurements is required. Furthermore, by assuming the validity of equation (2.5), the same assumptions as presented for the derivation of the Rankine vortex model are made (section 2.4.1). Therefore, it is assumed that the radial profile of the circumferential velocity component is solely responsible for the size of the core radius.

Noting the above, the use of averaged quantities was considered to give the best indication of the core radius and the maximum circumferential velocity because the averaging process makes those parameters relatively independent from the measurement positions as has been shown in *Gillmeier et al. (2016)*. Therefore, in the following, surface pressures, velocity component and radial / vertical distances have been normalised by p_{min}, $u_{\theta,max,average}$ and $R_{average}$, respectively. To unify vertical (radial) distances, in what follows, a further degree of normalisation is undertaken, i.e., each height (radial distance) is normalised by the corresponding maximum of $z/R_{average}$ ($r/R_{average}$) for each swirl ratio. The actual maxima used are given in either the figure's captions or additional tables.

4.3. Measurement techniques

4.3.1. Surface pressure measurements

Surface pressure is measured with a Multi-Channel-Pressure-System manufactured by *Solution for Research Ltd*. The device consists of 64 pressure transducers distributed in eight separate boxes. By means of 0.3m long polyvinyl chloride (*PVC*) tube connections, pressure transducers were connected to surface pressure taps. The inner/outer diameter of the *PVC* tube was 0.001m/0.002m. The method used to correct the effect of the tube's length on the pressure signal is based on the method presented by *Irwin et al. (1979)* and is shown in appendix D. In addition, each pressure transducer was connected to a reference port. The reference pressure (p_∞) is measured outside the vortex chamber and therefore, is not influenced by the generated vortex and represents the ambient atmospheric pressure. The static pressure measured at the transducer (p) is the difference between the measured surface pressure at the tap (p_{tap}) and the reference pressure. Pressure transducers measure pressure differences as an electrical signal. By means of an Analog-to-Digital-Converter, the electrical signal is transformed. A software developed by *Solution for Research Ltd*. converts the digital signal back to pressure difference by means of a previously generated calibration file. Collected surface pressure time series were then saved to a file for further post-processing.

Surface pressure distributions were measured instantaneously on the ground plane of all simulators along two perpendicular lines denoted *x* and *y* (Figure 4.2) every 0.01s for a period of 60 seconds. In *M1*, pressure taps are distributed at a spacing of 0.05m from the chamber's

centre up to a distance of 0.75m. In *S1 − S4*, surface pressure is mapped with a spacing of 0.01m from the chamber's centre up to a distance of 0.15m. Additionally, pressure taps were arranged in a circular pattern surrounding the corresponding simulator's centre up to a radial distance of 0.04m and 0.20m as illustrated in figure 4.2a and figure 4.2b for *S1 − S4* and *M1*, respectively.

a)

b)
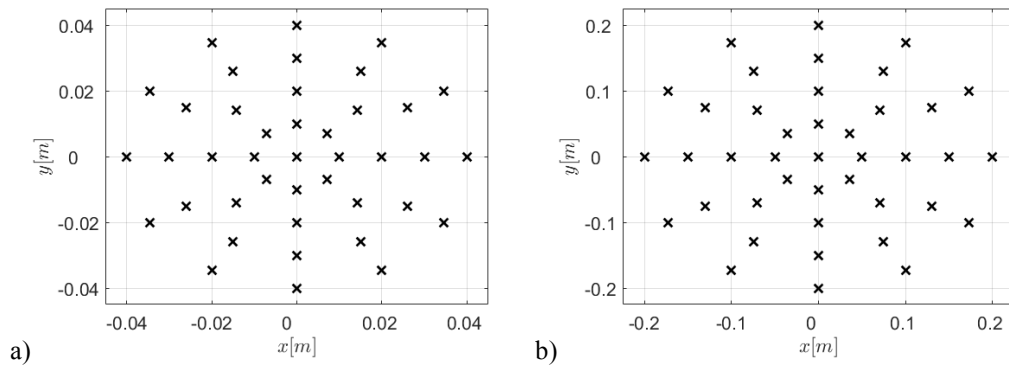
Figure 4.2: Circular arrangement of surface pressure taps in *S1 − S4* (a) and *M1* (b).

4.3.2.   *Velocity measurements*

A two-axis traverse system inside the simulators allows the positioning of measurement devices with an accuracy of 1mm. For point velocity measurements, a Cobra Probe (*TFI Manual: Series 100 Cobra Probe, 2011)* was mounted to the traverse system. The Cobra probe is a multi-hole pressure probe that provides the dynamic pressure in three components. An internal data acquisition system converts the analogue signal from the Cobra Probe to a digital signal before sending it to a computer. By means of the TFI Device Control software, the digital signal is converted to three-component velocity data using a pre-determined calibration (*TFI Manual: Series 100 Cobra Probe, 2011*). Sampling time and frequency can be defined in the software and the velocity time series can be saved to a file for further post-processing.

Point velocity measurements were obtained every 0.01s for a period of 80 seconds at nine heights above the surface of simulators *S1 – S4* (0.01m, 0.03m, 0.05m, 0.07m, 0.10m, 0.13m, 0.15m, 0.17m and 0.20m) and ten heights above the surface of simulator *M1* (0.01m, 0.05m, 0.10m, 0.15m, 0.20m, 0.25m, 0.30m, 0.40m, 0.50m, 0.60m). The corresponding radial spacing of measurement positions from the centre of each simulator up to a distance of 0.18m and 0.55m for *S1 – S4* and *M1* was 0.010m and 0.025m, respectively.

It is acknowledged that a Cobra Probe is an intrusive measurement device and therefore, a potential effect of the probe on the flow field cannot be avoided entirely; however, it is also noted that non-intrusive measurement techniques have their limitations (*Church et al., 1979* and *Refan and Hangan, 2016*).

Section 4.4 provides detailed information regarding the experimental measurement uncertainty. Where appropriate, experimental measurement uncertainties have been illustrated in order to enable the reader to immediately comprehend the importance (or otherwise) of the data and the conclusions. Furthermore, it is noted that the size of the probe is more than 10^6 times smaller than the convergence chamber of simulator *M1* and more than 10^4 times smaller than the convergence chamber of *S1*. In addition, the influence of the traverse system on surface pressure measurements was found to be smaller than the experimental measurement uncertainty. Therefore, it is argued that within the limits indicated, the Cobra probe is appropriate to be used.

4.4. Data quality

In order to provide sensible information and in order to evaluate potential differences between the simulations, it is of crucial importance to acknowledge the experimental measurement uncertainty associated with the measurements. The experimental measurement uncertainty is a combination of uncertainties due to measuring a finite time series (statistical uncertainty), operator errors such as probe and guide vane angle positioning (repeatability) and the uncertainty of the measurement device itself. In this study, pressure transducers (type: *HCLA12X5DB*) with a typical uncertainty of ± 5 Nm^{-2} were used. The Cobra Probe is accurate to within ± 0.5m/s for the velocity vector up to a turbulence intensity of ~30%. Therefore, positions with a turbulence intensity greater than 30% were excluded from the analysis. Furthermore, the Cobra Probe can measure velocity data greater than 2m/s within a cone of influence of $\pm 45°$. Those limitations can have a direct influence on the measured data. For example, if the recorded data quality (percentage of velocity samples of a measured time series, which are > 2m/s and have an angle of attack < $\pm 45°$) is less than 100% then this can introduce a bias in the calculated velocity vector – the lower the data quality the greater the potential bias. To minimize the bias in time-averaged velocities, only those positions with a data quality of greater than 80% were accepted for further analysis. This threshold is assumed to provide a suitable compromise between data quality and quantity.

4.4.1.   Statistical uncertainty

The statistical uncertainty is a measure of uncertainty of the time average with respect to the unsteadiness of the flow or surface pressure field. Therefore, it is highly important to verify that the time average of a statistically, stationary stochastic process converges towards the mean value of all possible realisations within the chosen measurement duration. In order to address the statistical uncertainty, convergence tests were undertaken for all simulations at the corresponding core radius at the lowest measurement height for velocity measurements, and at the surface in the centre of the simulators for pressure measurements. For the convergence tests, time series were measured for a duration of 600 seconds and running averages (*RA*) with increasing sampling durations (from 10 seconds – 600 seconds) were calculated. Figure 4.3 shows examples of convergence tests carried out for (a) the circumferential velocity component and for (b) surface pressure measurements in *M1* for $S = 0.69$.
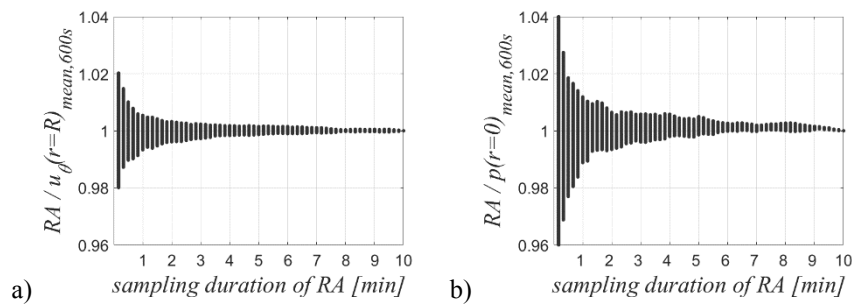
Figure 4.3: Convergence tests of (a) the circumferential velocity component and (b) surface pressures for $S = 0.69$ in *M1*.

Based on all convergence tests conducted, a sampling duration of 80 seconds for velocities was found to be long enough in order to determine the time average of circumferential and vertical velocity components with an uncertainty below ±2% for all simulations. Statistical uncertainties of radial velocity components were found to be below ±6%, ±3% and ±0.5% for

$S = 0.14$, $S = 0.30$ and $S = 0.69$, respectively. Gaining a reduction in uncertainty after 80 seconds is extremely time-consuming. Percentages given for statistical uncertainties relate to the corresponding time-averaged circumferential velocity component ($u_{\theta,mean,600s}$) and surface pressure ($p_{mean,600s}$), which were obtained after sampling for 600 seconds (Table 4.2). The decreasing uncertainty with increasing swirl ratio for the radial velocity component can therefore, partly be explained by the increase in $u_{\theta,mean,600s}$ with increasing swirl ratio (Table 4.2).

Table 4.2: Time-averaged circumferential velocity components and surface pressures after sampling for 600 seconds.

	$u_{\theta,mean,600s}$ [m/s]			$p_{mean,600s}$ [Nm^{-2}]		
	$S = 0.14$	$S = 0.30$	$S = 0.69$	$S = 0.14$	$S = 0.30$	$S = 0.69$
M1	5.31	9.39	10.51	-136.30	-224.22	-164.44
S1	4.97	7.34	8.49	-115.43	-188.66	-153.12
S2	-	8.14	9.22	-	-189.36	-148.94
S3	-	8.21	10.01	-	-191.59	-145.69
S4	-	7.11	8.06	-	-193.85	-153.06

For all surface pressure convergence tests, a sampling duration of 60 seconds was found to be long enough in order to determine the time average to approximately $\pm27\%$, $\pm6\%$ and $\pm1\%$ for $S = 0.14$, $S = 0.30$ and $S = 0.69$, respectively. The statistical uncertainty of surface pressure measurements at the centre of the corresponding simulator seems to be swirl ratio dependent, and, similar to the statistical uncertainty of velocity measurements, uncertainties seem to decrease with increasing swirl ratio. However, for pressure measurements, this cannot be explained with an increasing central surface pressure deficit ($p_{mean,600s}$) with increasing swirl ratio because the smallest surface pressure deficit was observed for the largest swirl ratio in all simulators (Table 4.2). Therefore, larger statistical uncertainties of central surface pressures for

the lowest swirl ratio could be an indication for a more transient vortex behaviour in time for relatively low swirl ratios compared to larger swirl ratios. A potential reason why this is not reflected in statistical uncertainties of velocity measurements could be that transient effects potentially occur at locations relatively close to the vortex centre, where surface pressure gradients are relatively large, especially for the lowest swirl ratio, and that core radius positions are not that strongly affected by this potentially unstable vortex behaviour.

The effect of non-stationary processes in tornado-like vortices is analysed in detail in section 7. Thereby, some light is shed upon the question why temporally averaged surface pressures for relatively low swirl ratios have larger uncertainties close to the simulator's centre than at larger radial distances and for larger swirl ratios.

4.4.2.   Repeatability

The repeatability is the degree to which repeated measurements under unchanged boundary conditions show the same results. Surface pressure measurements and the radial profile of velocities in the lowest measurement height were repeated five times for each simulation. The measurement repeatability is analysed in the form of a distribution of all possible differences of the corresponding repetitions. For example, figures 4.4a and 4.4b show the measurement repeatability distribution of circumferential velocity components and surface pressures for $S = 0.69$ in *M1*.
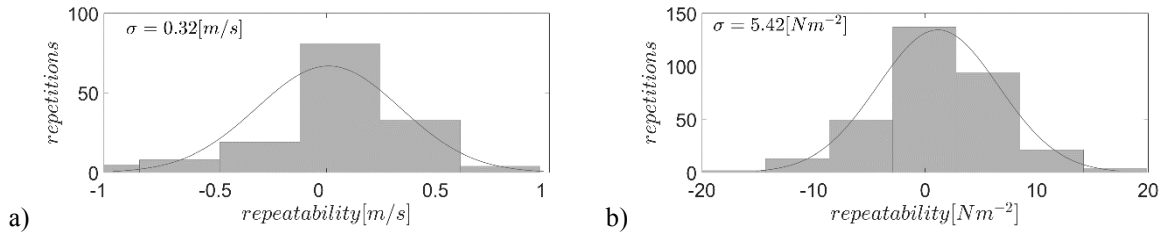
Figure 4.4: Distributions of the repeatability of circumferential velocity components (a) and surface pressures (b) for $S = 0.69$ in $M1$.

The standard deviation, σ, of the corresponding distribution was chosen as representative measure to evaluate the repeatability. Percentages given for the repeatability in table 4.3 relate to the corresponding values of $u_{\theta,mean,600s}$ and $p_{mean,600s}$, presented in table 4.2. Similar to the statistical uncertainty, overall smaller uncertainties are observed with increasing swirl ratio (Table 4.3). Table 4.3b also shows that the repeatability of surface pressure measurements is dependent on the swirl ratio. Furthermore, for $S = 0.14$ and $S = 0.30$ the repeatability is not only dependent on the swirl ratio, but also on the radial distance. For that reason, a repeatability dependent on r is introduced for those cases because a uniform value would highly underestimate the repeatability for measurement positions close to the vortex centre, and highly overestimate the repeatability for positions further away from the vortex centre. Therefore, in table 4.3b, the repeatability of surface pressure measurements for $S = 0.14$ is given for normalised radial locations $(r/R_{average}) / (r/R_{average})_{max} < 0.2$, equal to 0.2 and larger than 0.2. For $S = 0.30$, no difference in the repeatability was observed for radial positions ≤ 0.2, and no significant dependence on the radial distance was found for the repeatability of surface pressure measurements for $S = 0.69$ and all velocity measurements. Consequently, a uniform measurement repeatability independent from r is used for those cases (Table 4.3).

Table 4.3: Repetition uncertainties for velocity components (a) and surface pressures (b) in *M1* and *S1 - S4*.

a)

	S = 0.14		
	u_θ [%]	u_r [%]	u_z [%]
M1	∓9.6	∓8.7	∓3.2
S1	∓10.2	∓9.3	∓3.5

	S = 0.30			S = 0.69		
	u_θ [%]	u_r [%]	u_z [%]	u_θ [%]	u_r [%]	u_z [%]
M1	∓4.7	∓6.2	∓1.7	∓3.0	∓2.1	∓0.8
S1	∓8.2	∓7.9	∓3.1	∓1.6	∓2.9	∓2.1
S2	∓3.3	∓9.7	∓3.3	∓4.1	∓1.7	∓1.2
S3	∓1.8	∓5.6	∓1.9	∓3.3	∓5.9	∓1.9
S4	∓1.4	∓8.4	∓2.0	∓2.5	∓4.3	∓1.5

b)

	S = 0.14		
	$p_{(<0.2)}$ [%]	$p_{(=0.2)}$ [%]	$p_{(>0.2)}$ [%]
M1	∓39.3	∓9.5	∓1.4
S1	∓41.0	∓11.4	∓1.8

	S = 0.30		S = 0.69
	$p_{(\leq0.2)}$ [%]	$p_{(>0.2)}$ [%]	p [%]
M1	∓ 7.7	∓1.7	∓3.3
S1	∓ 4.6	∓1.7	∓1.7
S2	∓10.6	∓3.4	∓2.2
S3	∓ 3.2	∓1.3	∓1.7
S4	∓ 4.2	∓1.4	∓1.2

The relatively low repeatability close to the vortex centre for $S = 0.14$ and $S = 0.30$ is not surprising because the statistical uncertainty found at those positions is limiting the repeatability. Therefore, large uncertainties for $S = 0.14$ and $S = 0.30$ close to the vortex core, can partly be explained by the large statistical uncertainty at those positions. Furthermore, repeatability percentages presented in table 4.3b suggest that positions close to the simulator's centre for relatively low swirl ratios are more sensitive to small variations in boundary conditions such as the guide vane angle positioning.

4.4.3. *Experimental measurement uncertainty*

The associated experimental measurement uncertainty of velocity and surface pressure measurements, illustrated in later figures is based on the measurement repeatability because both, statistical and device uncertainties are assumed to be reflected within the uncertainty defined by the repeatability. Therefore, the repeatability is assumed to provide a reasonable range for experimental measurement uncertainties.

Furthermore, it is noted that an uncertainty is introduced to $R_{average}$. The uncertainty of $R_{average}$ is dependent on the radial spacing of measurement locations and consequently is ∓ 0.0050m for simulations conducted in *S1*, *S2*, *S3* and *S4* and ∓ 0.0125m for simulations conducted in *M1*. This uncertainty corresponds to $\mp ½$ of the corresponding radial spacing of velocity measurements outline in section.4.3.2.

5. COMPARISON OF ANALYTICAL AND PHYSICAL MODEL RESULTS

In this section, flow fields and surface pressure data of vortices obtained for three different swirl ratios ($S = 0.14$, $S = 0.30$, and $S = 0.69$) in the medium-scale tornado-like vortex generator (*M1*) are analysed and the capability of the Rankine, the Burgers-Rott, the Sullivan and the Baker vortex model to replicate the experimental results is evaluated. The majority of this section has been published in *Gillmeier et al. (2018)* and is reproduced with the permission of the co-authors.

5.1. The flow structure

In order to address the complex nature of the analysed flow fields, the 3-D velocity fields obtained for $S = 0.14$, $S = 0.30$ and $S = 0.69$ are shown in figure 5.1. Also shown are results of selected analytical vortex models, which for the sake of brevity are not repeated for all swirl ratios. Experimentally obtained $R_{average}$ and $u_{\theta,max,average}$ (shown in figure 5.2) are used to calculate the flow field of the Rankine, the Burgers-Rott, the Sullivan and the Baker vortex model for corresponding swirl ratios. The 'viscosity' parameter in the Burgers-Rott and the

Sullivan vortex model is assumed to be $v = 0.05 \text{ m}^2\text{s}^{-1}$. It is noted that for the analysis presented in figure 5.1b, the actual 'viscosity' value is not that crucial because this comparison focuses on the flow structure rather than on the actual velocity magnitude, which is affected by the 'viscosity'. Due to the restrictions when measuring with the Cobra probe, the velocity field close to the vortex centre for all swirl ratios, and near the surface at larger radial distances for $S = 0.14$ could not be captured. Inside the vortex core ($r < R_{average}$), velocity vectors are only shown at positions where absolute values of time-averaged radial and vertical velocities are larger than the corresponding experimental measurement uncertainty. Hence, only positions for which a clear directionality can be defined are presented in figure 5.1.
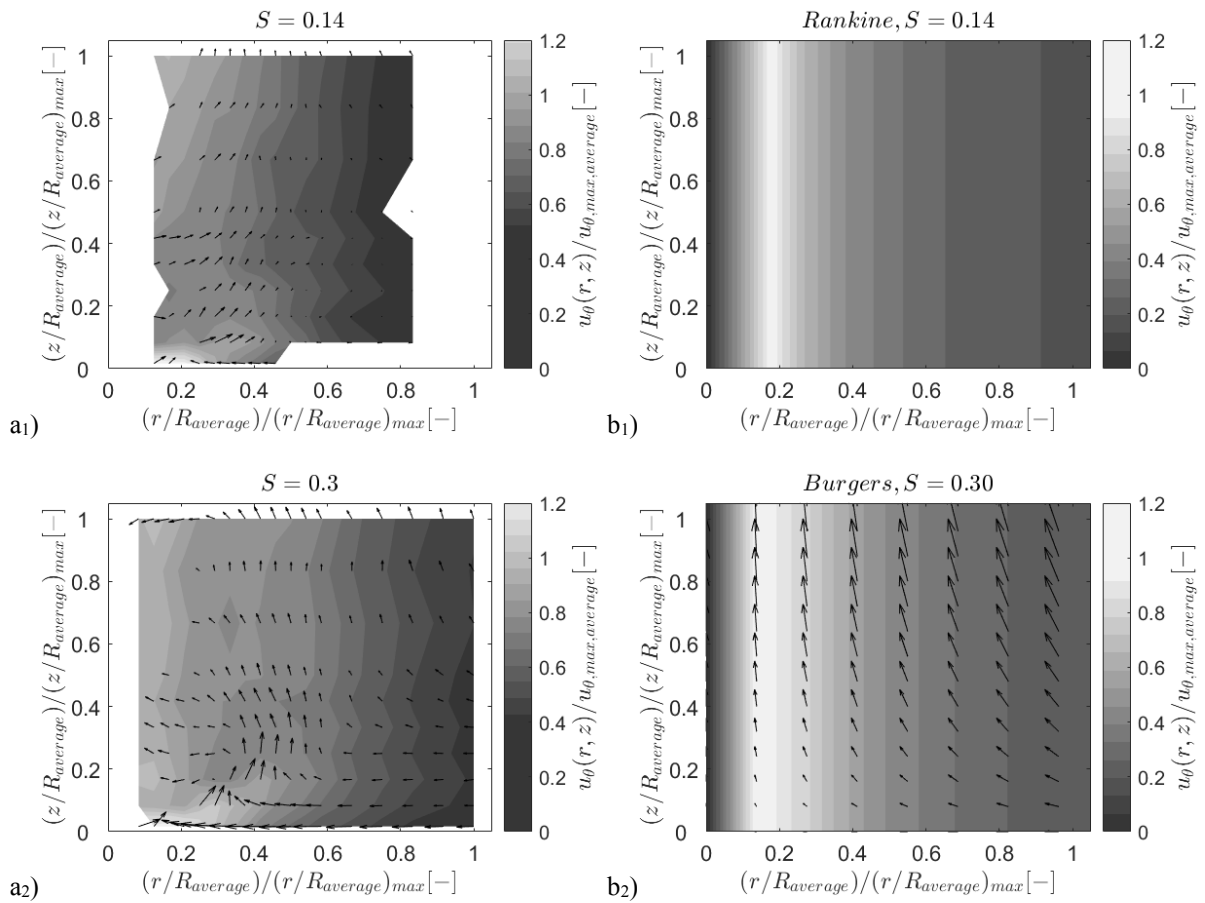
Figure 5.1: continued on the following page.
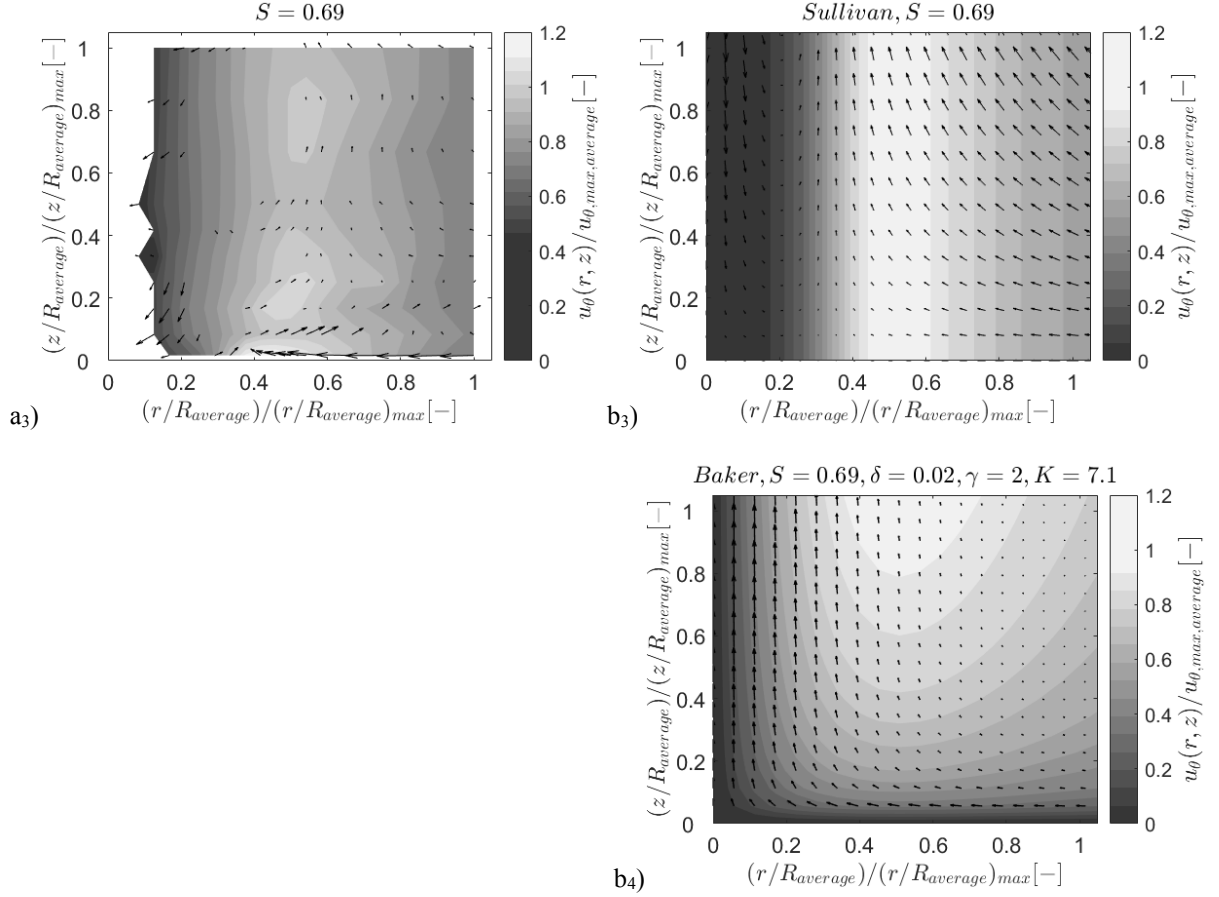
Figure 5.1: Experimental results of the 3-D velocity field are shown in a_1 ($S = 0.14$), a_2 ($S = 0.30$) and a_3 ($S = 0.69$). Corresponding results of the Rankine, the Burgers-Rott, the Sullivan and the Baker vortex model are shown in b_1, b_2, b_3 and b_4, respectively. The normalised circumferential velocity component is shown as contour and radial and vertical velocity components are shown as 2-D vector field. To normalise heights and distances, maximum values of experimentally obtained *(z/$R_{average}$)max* and *(r/$R_{average}$)max* are used. For $S = 0.14$, $S = 0.30$ and $S = 0.69$, *(r/$R_{average}$)max* = 5.00, 6.63, 1.80 and *(z/$R_{average}$)max* = 5.45, 7.23 , 1.97, respectively.

In general, experimentally obtained flow characteristics reveal flow patterns, which are significantly more complex compared to the suggested flow structure of the vortex models (Figure 5.1). The measured circumferential velocity component for all swirl ratios increases towards the core radius and reaches the overall maximum close to the surface. Furthermore, a strong decrease in circumferential velocity can be observed with height in the lower heights for all swirl ratios (Figure 5.1a). The circumferential velocity components of the Rankine, the Burgers-Rott and the Sullivan vortex model (Figure 5.1b$_1$, Figure 5.1b$_2$, and Figure 5.1b$_3$) are

not a function of height and consequently, cannot represent the height dependence found in the simulator (Figure 5.1a). The circumferential velocity of the Baker vortex model is height dependent and increases with increasing height from the ground (Figure 5.1b$_4$), which is also not obtained experimentally. Strong radial inflow velocities for all swirl ratios close to the simulator's surface were obtained (Figure 5.1a), and can theoretically be explained by an imbalance of the cyclostrophic equation (Eq. 2.5) due to friction (*Trapp, 2000*). Surface friction causes the circumferential velocity component to decrease. The, therefore, unbalanced radial pressure gradient drives the strong radial inflow up to the position, where the overall maximum circumferential velocity occurs (Figure 5.1a). At this position, the radial velocity decreases drastically and the vertical velocity increases significantly. The Rankine, the Burgers-Rott and the Sullivan vortex model cannot replicate this flow behaviour due to either a non-existing radial velocity component (the Rankine vortex model) or radial velocity components, which are height-independent and increase with increasing radial distance (the Burgers-Rott and the Sullivan vortex model). The Baker vortex model on the other hand seems to be able to capture this phenomenon and places largest radial velocity components at a height (z_m) close to the surface.

Contrary to what may be expected, Figure 5.1a$_1$ shows a radial outflow from the vortex centre. However, this is supported by the work of *Mishra et al. (2008a)* and *Haan et al. (2008)*, where tentative evidence of a radial outflow close to the vortex centre can be inferred for low swirl ratios. Various possible reasons for this behaviour (including vortex core unsteadiness with respect to height) seem possible; however, firm conclusions as to why this may be the case cannot, at present, be drawn.

The 3-D velocity field obtained for $S = 0.30$ (Figure 5.1a$_2$) shows tentative evidence to suggest the presence of a counter-clockwise rotating cell near the surface close to the vortex centre, covering a normalised area of approximately 0.25×0.25. At greater heights, the vortex core is dominated by radial inflow and an updraft, which turns into a downdraft at a normalised height of ~1. This could suggest the presence of a second counter-clockwise rotating cell in the vortex core. The central radial outflow at $z = 0.01$m could suggest a narrow central downdraft, which penetrates all heights and feeds into the outflow caused by the near surface cell.

With increasing swirl ratio ($S = 0.69$), a downdraft is detected close to the centre of the simulator (Figure 5.1a$_3$). This flow structure is expected for a two-celled vortex, such as the Sullivan vortex model (Figure 5.1c$_3$). However, the downdraft is directed slightly towards the simulator's centre, which was also observed by *Haan et al. (2008)* for a high swirl ratio. The lack of detailed, fine scale, experimental data at the centre of the vortex, make further conclusions difficult.

Due to non-existing radial and vertical velocity components, none of the described radial and vertical flow characteristics can be represented with the Rankine vortex model (Figure 5.1b$_1$). Notwithstanding the more complex structure of the Burgers-Rott, the Sullivan and the Baker vortex model, the experimentally captured flow patterns are far more complex than suggested by any of the analytical models.

A more detailed analysis of the flow field can be found in figures 5.2 – 5.4, illustrating the circumferential, radial and vertical velocity components for $z = 0.01$m, $z = 0.10$m, $z = 0.20$m and $z = 0.40$m, for $S = 0.14$ (a), $S = 0.30$ (b) and $S = 0.69$ (c).

Experimentally obtained results for $\overline{u}_\theta$ (Figure 5.2) show that for all swirl ratios, the overall maximum of $\overline{u}_\theta$ occurs at the lowest measurement height ($z = 0.01$m, Figure 5.2). The distribution of circumferential velocity components obtained for $z > 0.01$m shows a behaviour, which seems to be relatively independent from height and observed differences mostly lie within the experimental measurement uncertainty outlined in section 4.4 (Figure 5.2). The lowest height reveals an entirely different flow structure compared to the rest of the generated vortex. This suggests a similar vertical profile of circumferential velocity components as observed by *Kosiba and Wurman (2013)*. Figure 5.2 also outlines differences in the circumferential velocity profile for different swirl ratios. Figure 5.2 shows that $u_{\theta,max,average}$ increases with increasing swirl ratio from $3.65 - 8.75$m/s. In addition, $R_{average}$ increases with increasing swirl ratio from $0.11 - 0.31$m. Results obtained for $S = 0.30$ do not follow this trend and reveal an averaged core radius of 0.08m, which is smaller than the one observed for $S = 0.14$. This finding is an artefact of the complex flow field of the simulated vortices, particularly at greater heights for $S = 0.30$, where relatively large circumferential velocities occur at relatively small radial distances (Figure 5.1a$_2$) and therefore, cause a relatively small $R_{average}$. Most commonly in tornado research, R_{global} is used in order to determine a representative vortex size (e.g., *Haan et al., 2008*; *Sabareesh et al., 2012*; *Refan et al., 2017b* and *Refan and Hangan, 2018*). However, results presented in this study reveal that this size might not be representative for the entire flow field. For the sake of completeness, it is noted that if the core radius of flow fields presented in figure 5.1 had been defined based on the overall (global) circumferential maximum, the vortex radius would increase with increasing swirl ratio from $R_{global} \sim 0.075$m to 0.100m to 0.250m for $S = 0.14$, $S = 0.30$ and $S = 0.69$, respectively.

In general, the Rankine, the Burgers-Rott and the Sullivan vortex model appear to underestimate the trend of $\bar{u}_\theta$ for $S = 0.14$ (Figure 5.2a), although, differences around the core radius are close to or within the experimental measurement uncertainty in most cases. However, the Baker vortex model appears to predict the trend reasonably well for this swirl ratio. Due to the relatively complex flow structure observed for $S = 0.30$, all models appear to fail to capture the distribution of $\bar{u}_\theta$ (Figure 5.2b). Inside the vortex core, a comparison between experimentally obtained results and vortex models is difficult due to the lack of good experimental data for $S = 0.14$ and $S = 0.30$ (Figure 5.2a and Figure 5.2b). The circumferential velocity component of the Burgers-Rott and the Baker vortex model match the experimental data obtained for $S = 0.69$ relatively well (Figure 5.2c). Results of the Rankine and the Sullivan vortex model, again underestimate the magnitude of obtained circumferential velocities for the highest swirl ratio.

a)

b)

c)
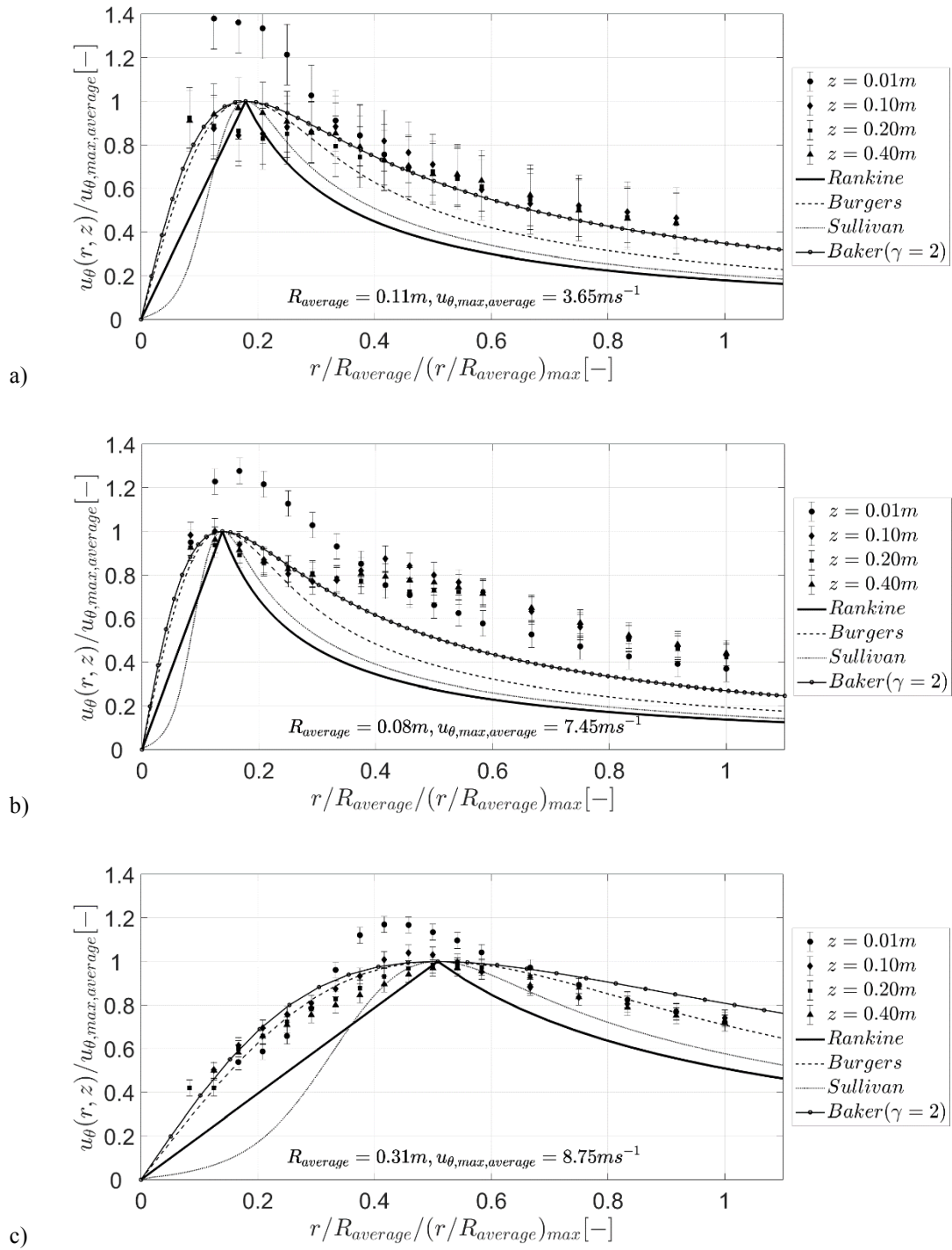
Figure 5.2: Measured circumferential velocity component for $S = 0.14$ (a), $S = 0.30$ (b) and $S = 0.69$ (c). Additionally, results of the circumferential velocity component of the Rankine, the Burgers-Rott, the Sullivan, and the Baker vortex model are shown. To normalise the radial distance, maximum values of experimentally obtained $(r/R_{average})_{max}$ are used. For $S = 0.14$, $S = 0.30$ and $S = 0.69$, $(r/R_{average})_{max} = 5.00$, 6.63, 1.80, respectively.

Figure 5.3 illustrates the radial distribution of $\bar{u}_r$ for $z = 0.01$m, $z = 0.10$m, $z = 0.20$m and $z = 0.40$m. Additionally a height average is calculated and shown for all velocities obtained for $z > 0.01$m. It is noted that the swirl ratio (S) defined in equation (4.2) is, unlike the definition adopted in the Baker vortex model (S_{Baker}), solely a function of the tornado generator's characteristics. For that reason, values of S and S_{Baker} differ for the same flow field in the following figures. As illustrated in figure 5.3a and 5.3b, the Baker vortex model fits the data obtained reasonably well close to the surface, whereas the Sullivan and the Burgers-Rott vortex model are a better fit for experimental data obtained in greater heights. This is perhaps not too surprising given the assumptions embedded in the models. However, for the largest swirl ratio (Figure 5.3c), the Baker vortex model only represents the trend in the lowest height for normalised radial distances greater than 0.6, whereas the Sullivan vortex model performs better for lower normalised radial distances at the lowest height.

For $S = 0.14$, the radial outflow inside the vortex core suggests the structure of a (limited height) two-celled vortex. Thus, in general, the height-averaged structure of $\bar{u}_r$ appears to be reasonably represented by the Sullivan vortex model (Figure 5.3a). Even though one feature of a two-celled vortex is present for $S = 0.14$, the vertical downdraft suggested by the Sullivan vortex model at the vortex centre was not capture (Figure 5.4a). For the vertical velocity component obtained with $S = 0.14$, none of the vortex models is capable of replicating the maximum updraft just outside the vortex core (Figure 5.4a). However, for larger radial distances, results of the Burgers-Rott and the Sullivan vortex model can be used to reproduce height-averaged vertical velocities (Figure 5.4a). Certainly, it needs to be noted that for this case, the vortex models fail to replicate the complex behaviour observed experimentally. Although, there are only few positions available for a comparison in the lowest height, radial and vertical velocity component

of the Baker vortex model are in relatively good agreement with the experimental data (Figure 5.3a and Figure 5.4a).

For $S = 0.30$, radial velocities are mainly directed towards the vortex centre (radial inflow). The magnitude of radial velocities in greater heights $z > 0.01$m is relatively low compared to radial velocities obtained in the lowest height ($z = 0.01$m). The best fit for this 'single-celled' flow behaviour is achieved with the Burgers-Rott vortex model with a relatively low 'viscosity' parameter ($v = 0.0015$m^{2}s^{-1}), to minimise the increase of radial inflow from the vortex centre towards larger radial distances. Similar to the vertical velocity component for $S = 0.14$, also here, the maximum updraft outside the vortex core (Figure 5.4b) cannot be replicated by any of the introduced vortex models. However, for larger radial distances the Burgers-Rott vortex model can be used to model the height-averaged behaviour (Figure 5.4b). Nevertheless, the complex vertical flow structure cannot be captured. Radial and vertical velocity component of the Baker vortex model on the other hand are in good agreement with the experimental data for $z = 0.01$m (Figure 5.3b and Figure 5.4b).

For $S = 0.69$, radial velocities (Figure 5.3c) are found to be directed inwards, towards the vortex centre (radial inflow), even though a downdraft close to the vortex centre is found (Figure 5.4c). In terms of vortex models, this means that the radial velocity shows a 'single-celled' behaviour with radial inflow (the Burgers-Rott and the Baker vortex model), whereas the vertical velocity illustrates a 'two-celled' structure with downdraft (the Sullivan vortex model). None of the presented vortex models are capable of representing both of the observed flow patterns. For $S = 0.69$, the obtained flow field is far more complex than the assumed flow structure of a single-celled or a two-celled vortex. In this case, the flow reveals a 'multi-celled' structure with a weak

radial inflow and updraft outside the vortex core and a relatively strong radial inflow and downdraft inside the vortex core (Figure 5.3c and Figure 5.4c).

For radial and vertical velocity components of $S = 0.69$, an attempt is shown to use the Sullivan and the Baker vortex model to replicate some of the flow patterns observed in the lowest height ($z = 0.01$m). For the radial velocity component in the lowest height (Figure 5.3c), the Baker vortex model captures the radial inflow outside the vortex core, but overestimates velocities inside the vortex core. The decrease in radial inflow around the core radius can be replicated with the Sullivan vortex model; however, close to the vortex centre, the Sullivan vortex model is not able to replicate the flow field, and also for larger radial distances the Sullivan vortex model fails due to its increasing radial velocity component with increasing radial distance (Figure 5.3c).

For the vertical velocity (Figure 5.4c), the Sullivan vortex model can represent parts of the observed results. By means of the shape parameter, b, the downdraft region around the vortex centre of the Sullivan vortex model can be extended in the radial direction, so that for $b = 12$, results of the Sullivan vortex model show some similarity with the increase in radial inflow from the vortex core towards the vortex centre (Figure 5.4c). However, increasing b also results in an increasing downdraft at the vortex centre, which for $S = 0.69$ is highly overestimated. The Baker vortex model, in its single-celled form (as shown here) is not able to replicate the downdraft close to the vortex centre and the relatively strong vertical updraft around the core radius (Figure 5.4c).

a)

b)

c)
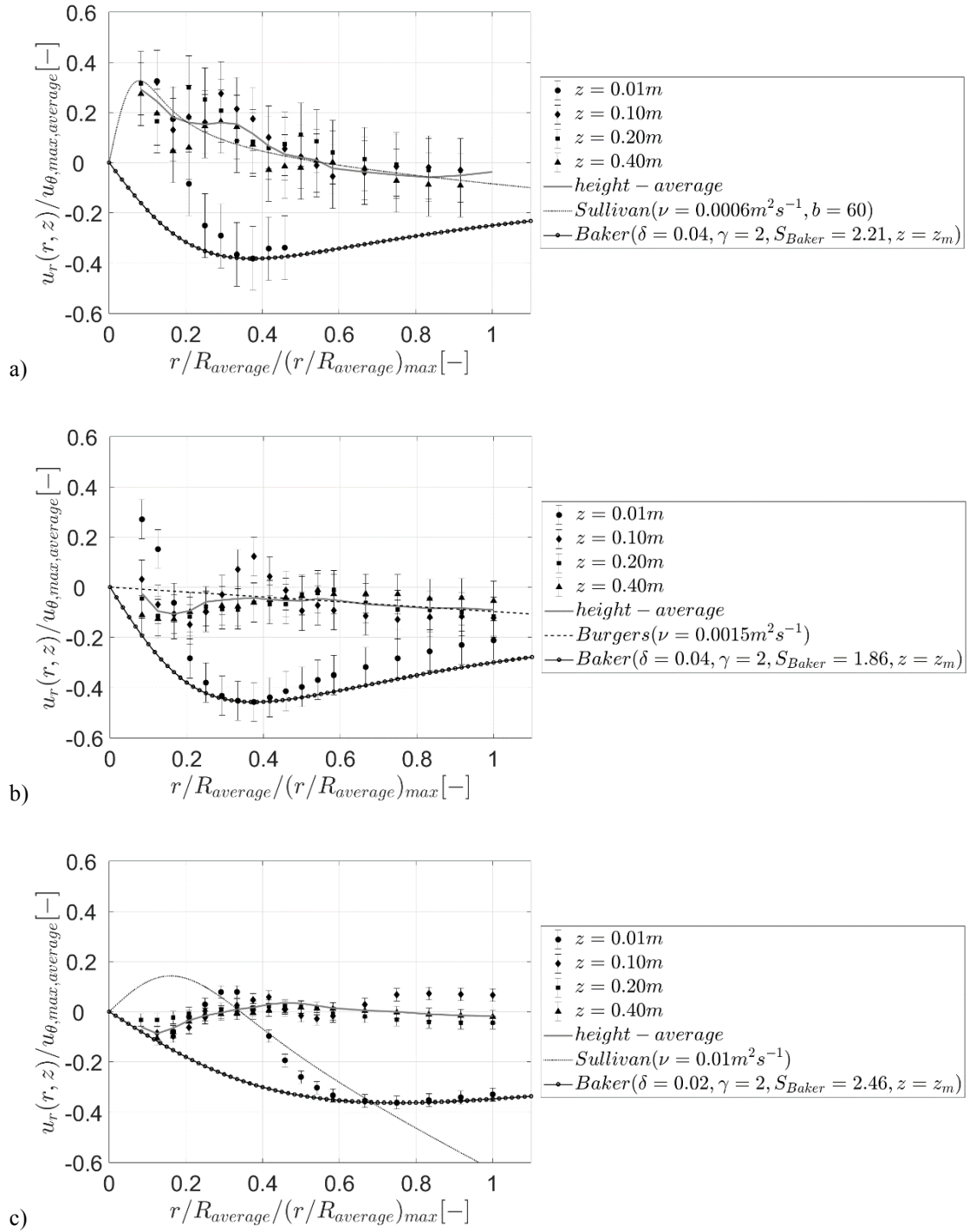
Figure 5.3: Measured radial velocity component for $S = 0.14$ (a), $S = 0.30$ (b) and $S = 0.69$ (c). Additionally, results of the radial velocity component of the Burgers-Rott (b) and the Sullivan vortex model (a and c) are shown. Results of the Baker vortex model are shown for the lowest height ($z = 0.01$). To normalise the radial distance, maximum values of experimentally obtained $(r/R_{average})_{max}$ are used. For $S = 0.14$, $S = 0.30$ and $S = 0.69$, $(r/R_{average})_{max} = 5.00$, 6.63, 1.80, respectively.
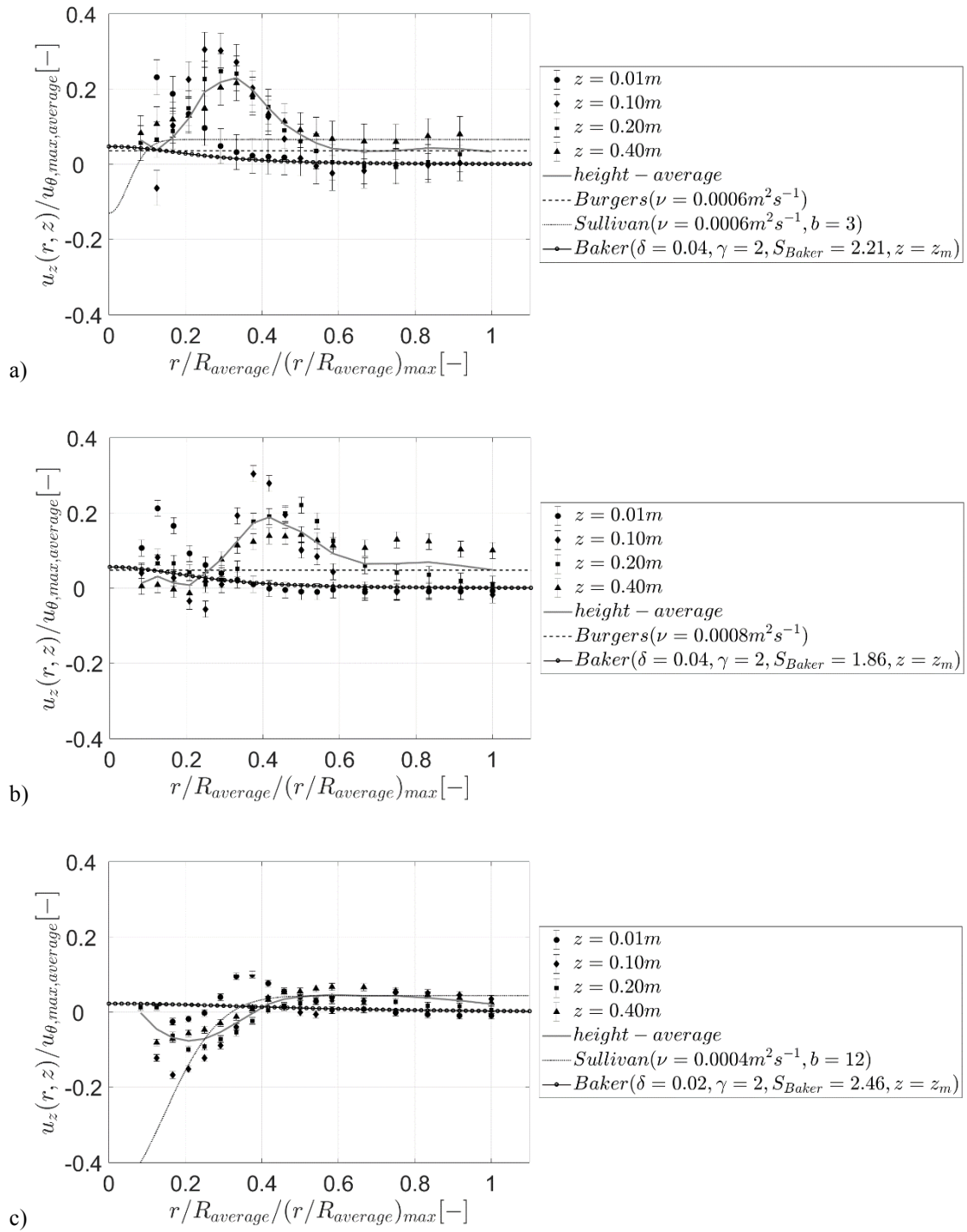
Figure 5.4: Measured vertical velocity component for $S = 0.14$ (a), $S = 0.30$ (b) and $S = 0.69$ (c). Additionally, results of the vertical velocity component of the Burgers-Rott (a and b) and the Sullivan vortex model (a and b) are shown. Results of the Baker vortex model are shown for the lowest height ($z = 0.01$). To normalise the radial distance, maximum values of experimentally obtained $(r/R_{average})_{max}$ are used. For $S = 0.14$, $S = 0.30$ and $S = 0.69$, $(r/R_{average})_{max}$ = 5.00, 6.63, 1.80, respectively.

5.2. Surface pressure distribution

Figure 5.5 shows the surface pressure distributions for $S = 0.14$, $S = 0.30$, and $S = 0.69$. The corresponding surface pressure distributions of the Rankine, the Burgers-Rott, the Sullivan and the Baker vortex model are illustrated in figures 5.5(a-d), respectively. Analytical surface pressure distributions are calculated based on core radii and maximum circumferential velocities embedded in figure 5.2. For the Burgers-Rott vortex model, v and $\bar{a}$ are adjusted for each swirl ratio to guaranty a physically reasonable surface pressure increase with increasing radial distance (Figure 5.5b). To avoid an unphysical decrease in surface pressure with increasing radial distance, the 'viscosity' parameter of the Sullivan vortex model is chosen to be zero (Figure 5.5c). The swirl ratio of the Baker vortex model (S_{Baker}) is responsible for differences in the surface pressure distribution as outlined in section 3.1.3. To allow a more flexible surface pressure model, the shape parameter, γ, in the Baker vortex model needs to be treated as a variable when deriving the static pressure distribution (Eq. 19). However, in this work, a shape parameter of $\gamma = 2$ is assumed. Consequently, differences of calculated surface pressure distributions of the Baker vortex model are largely caused by the different core radii for $S = 0.14$, $S = 0.30$ and $S = 0.69$ (Figure 5.5d).

Looking at figures 5.5, it could be concluded that differences in the measured surface pressure distribution depend significantly on the swirl ratio. The fastest increase in surface pressure from the vortex centre towards larger radial distances is observed for $S = 0.14$. Consequently, the smallest vortex would be expected for this swirl ratio; however, the smallest height-averaged core radius was found for $S = 0.30$ ($R_{average,(S=0.30)} = 0.08$m), compared to $R_{average}$ of $S = 0.14$

and $S = 0.69$ ($R_{average,(S=0.14)} = 0.11$m and $R_{average,(S=0.69)} = 0.31$m). Consequently, all vortex models suggest that the surface pressure distribution for $S = 0.30$ results in the smallest vortex, and as a result, underestimate / overestimate the radial surface pressure gradient for $S = 0.14$ / $S = 0.30$ (Figure 5.5). This finding suggests that $R_{average}$ for $S = 0.30$ might not be representative for the vortex core radius at the surface of the simulator. This, once more, highlights the difficulty of defining a core radius value, which is representative for the entire highly complex vortex structure. The only vortex model, which seems to capture the surface pressure distribution for $S = 0.30$, is the Baker vortex model (Figure 5.5d). This seems to be the case because of the additional effect of S_{Baker} on the surface pressure distribution, and since S_{Baker} was found to be the smallest for $S = 0.30$ (Figure 5.5d), the surface pressure distribution is affected as outlined in section 3.1.3 and therefore, compensates the effect $R_{average}$ has on the normalised surface pressure distribution.

The Burgers-Rott vortex model fails for $S = 0.14$ and $S = 0.30$ at larger radial distances from the vortex centre due to a physically unrealistic decrease in surface pressure, which is also explained in section 3.1.3.

The surface pressure distribution of the largest vortex ($S = 0.69$) illustrates the smallest radial pressure gradient (Figure 5.5). The best fit for the experimentally obtained surface pressure distribution of the larges swirl ratio ($S = 0.69$) is found for the Rankine vortex model (Figure 5.5a). The Burgers-Rott and the Baker vortex model underestimate the radial surface pressure gradient (Figure 5.5b and 5.5d). The Sullivan vortex model shows good agreement for normalised radial distances > 0.75 (Figure 5.5c); however, for smaller normalised radial distances ($(r/R_{average}) / (r/R_{average})_{max} < 0.75$), the Sullivan vortex model overestimates the

experimentally obtained surface pressure deficit due to its two-celled flow structure. Even though a downdraft is present close to the vortex centre for $S = 0.69$, the effect of it is not visible in the experimentally obtained surface pressure distribution.
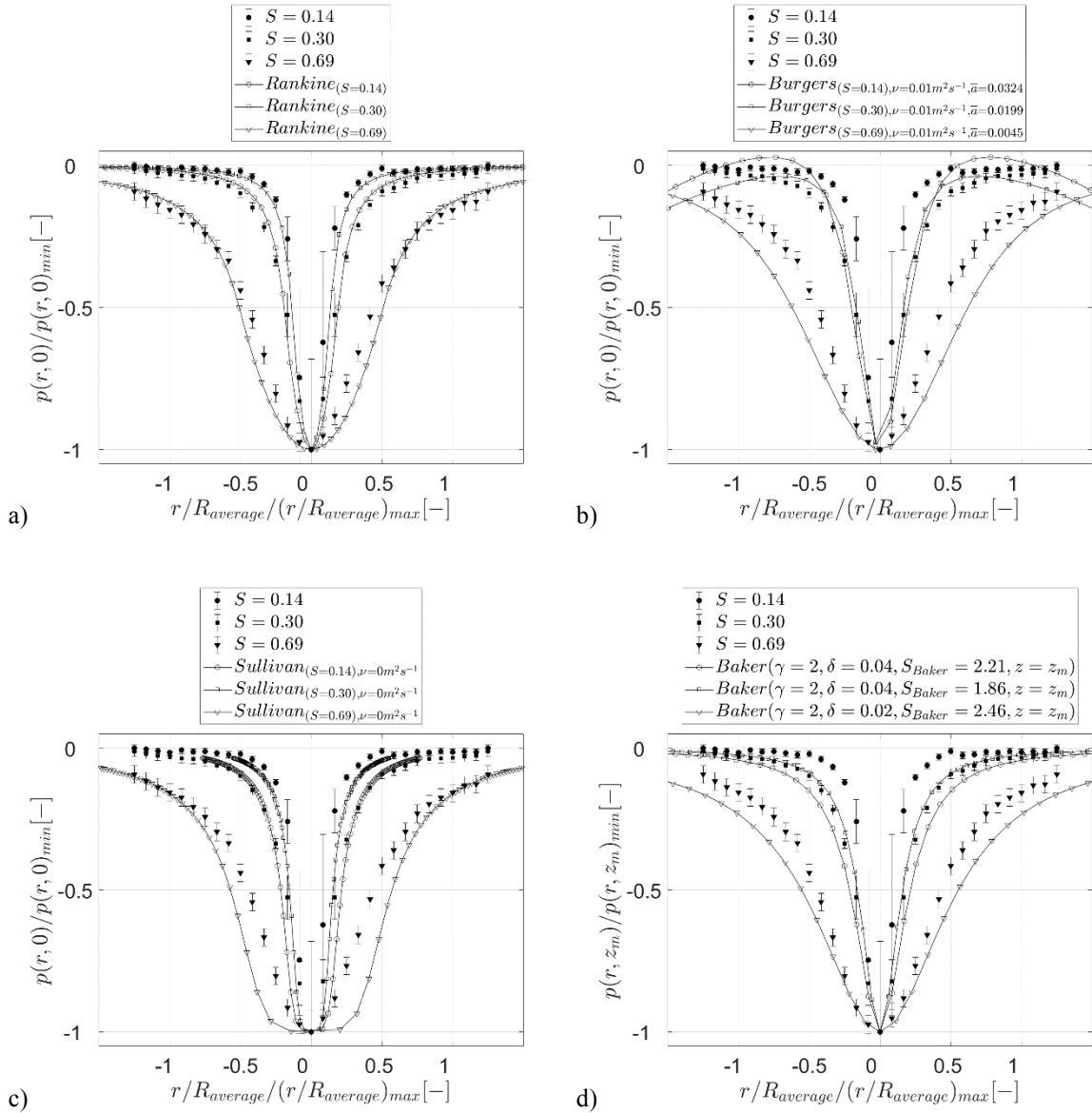
Figure 5.5: Measured surface pressure distributions for $S = 0.14$, $S = 0.30$, and $S = 0.69$ and corresponding surface pressure distributions of the Rankine (a), the Burgers-Rott (b), the Sullivan (c) and the Baker (d) vortex model. To normalise the radial distance, maximum values of experimentally obtained $(r/R_{average})_{max}$ are used. For $S = 0.14$, $S = 0.30$ and $S = 0.69$, $(r/R_{average})_{max} = 5.00$, 6.63, 1.80, respectively.

5.3. Concluding remarks

Based on this analysis, the following main conclusions can be drawn:

- Despite the simplicity of all the models examined, it has been shown that this area of research is highly complex, largely due to the interpretation of the different parameters involved.

- Measured flow pattern are far less structured and organised than the pattern suggested by any of the vortex models. Consequently, none of the presented models can be used to represent the three-dimensional vortex structures of experimentally generated tornado-like vortices.

- The Burgers-Rott and the Sullivan vortex model are able to replicate some parts of the flow field. However, parameters, which need to be chosen to make the model results fit the experimental data (v, $\bar{a}$ and b) differ for surface pressure and different velocity components of the same vortex.

- The Baker vortex model seemed to be the best model to replicate the radial inflow close to the ground. However, it fails for larger heights over the range tested.

- The Rankine, the Burgers-Rott, the Sullivan and the Baker vortex model are able to replicate certain parts of the surface pressure distribution, but, due to their limitations, those models are not adequate enough to replicate a variety of differently shaped pressure distributions, especially when the distribution is influenced by more parameters than just the location of the core radius.

- It is noted that the comparison presented relates to simulations conducted in only one simulator and that there are a variety of ways in which distances, pressure and velocity data could be normalised. It is possible that different normalisations could mask or exaggerate differences between both modelling techniques.

6. THE EFFECT OF THE SIMULATOR'S GEOMETRY ON THE SIMULATED FLOW FIELD

Using the medium-scale simulator (*M1*) of fixed geometry and the small-scale simulator (*S1*) of variable geometry, this section investigates the influence that the simulator's scale and geometric design can have on the simulation of tornado-like vortices. The majority of this section has been submitted for publication to the Journal of Wind Engineering and Industrial Aerodynamics and is reproduced with the permission of the co-authors.

6.1. Experimental methodology

Ten simulations have been undertaken (details of which are given in table 6.1), in order to evaluate:

T1)   the effect of the simulator's scale with constant aspect ratio and swirl ratio. In this case, the aspect ratio was fixed at 2 and the medium-scale (*M1*) and the small-scale simulator (*S1*) were used.

T2) the effect that the convection chamber may have on the simulation. In this case, the convection chamber height (H_2) of the small-scale simulator (*S1*) was reduced from $H_2 = 0.40$m to $H_2 = 0.25$m (*S2*) to $H_2 = 0.10$m (*S3*), whilst all other geometric lengths were kept constant.

T3) the effect that the convergence chamber may have on the simulation. In this case, H_1 in the small-scale simulator (*S1*) was reduced to 0.225m (*S4*).

In all cases, the flow fields of two swirl ratios ($S = 0.30$ and $S = 0.69$) are investigated and where necessary, the guide vane angles were adjusted to guarantee constant swirl ratios. Over the small range of Reynolds numbers investigated (Table 6.1), no Reynolds number dependence was found and as such is not considered further.

Table 6.1: Overview of non-dimensional dynamic parameters for the three comparison test cases.

Test case	*Simulator*	*α [°]*		*S*		*Re · 10⁵*	
T1	*M1*	*50*	*70*	*0.30*	*0.69*	*10*	*10*
	S1					*3*	*3*
T2	*S1*	*50*	*70*	*0.30*	*0.69*	*3*	*3*
	S2					*3*	*3*
	S3					*3*	*3*
T3	*S1*	*50*	*70*	*0.30*	*0.69*	*3*	*3*
	S4	*41.8*	*64.1*			*3*	*3*

The very nature of the experimental equipment and the scale of the simulator prevents in some cases a detailed knowledge of the flow structure across the entire flow field. As a result, for some simulations presented in the following, the complex flow structure inside the vortex could not be captured in detail. However, sufficient data has been gathered to undertake a relative

comparison of flow fields, and as a result, an insight into the question at hand is provided, i.e., does the geometry of the simulator influence the generated tornado-like flow field?

6.2. Simulations in the small-scale simulator (S1)

6.2.1.   The flow field

The 3-D velocity fields obtained in $S1$ for $S = 0.30$ and $S = 0.69$ are shown in figure 6.1. In addition, the location of the height-averaged core radius ($R_{average}$) is illustrated as solid vertical line. Due to the restrictions when measuring with the Cobra probe, the velocity field close to the vortex centre for both swirl ratios could not be captured. Inside the vortex core ($r < R_{average}$), velocity vectors are only shown at positions where absolute values of time-averaged radial and vertical velocities are larger than the corresponding experimental measurement uncertainty. Hence, the analysis is restricted to positions where a clear velocity vector was observed.
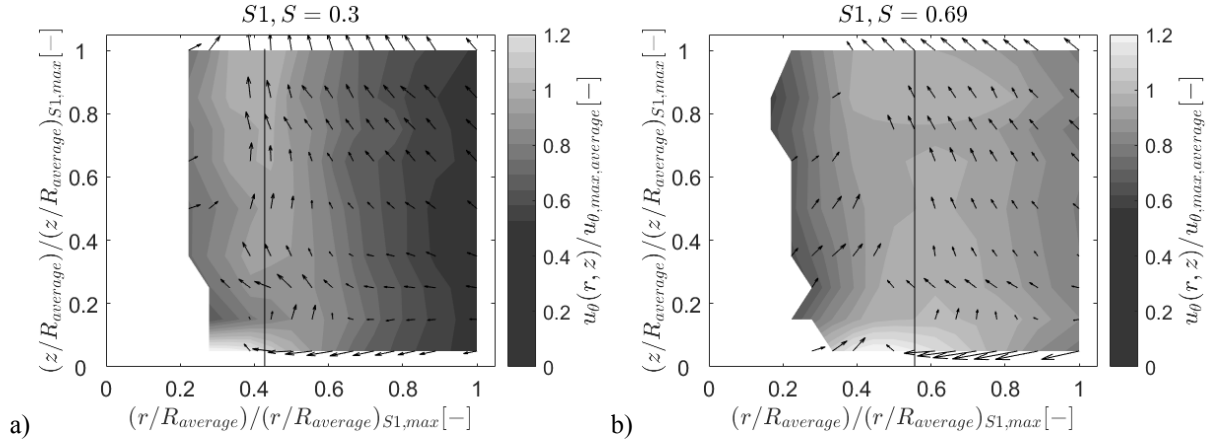
Figure 6.1: 3-D velocity fields in *S1* for *S* = 0.30 (a) and *S* = 0.69 (b). The normalised circumferential velocity component is shown as contour and the 2-D vector field indicates the vector based on the radial and vertical velocity component. The vertical solid black line indicates the corresponding location of the height-averaged core radius. For *S = 0.30* and *S = 0.69*, $(r/R_{average})_{max,S1}$ = 2.34 , 1.80 and $(z/R_{average})_{max,S1}$ = 2.60 , 2.00, respectively.

Figures 6.1 illustrates that for both swirl ratios in *S1*, the behaviour of the circumferential velocity component is, in general, as expected and as such is not discussed further. Figure 6.2a shows the radial profile of radial velocities at the lowest measurement height and illustrates a strong radial inflow with largest radial inflow velocities occurring just outside the vortex core for both swirl ratios. For *S* = 0.69, the radial inflow turns into an outflow at a normalised radial distance of ~0.45 (Figure 6.2a), whereas for *S* = 0.30, only radial inflow velocities are detected at the lowest height (Figure 6.2a). Additionally, figure 6.1a and 6.2c show that for *S* = 0.30 radial inflow is dominant inside the vortex core for normalised heights < 0.4. This finding, in combination with the radial outflow inside the vortex core at larger normalised heights > 0.4 (Figure 6.1a and 6.2c) could lead to the conclusion of a flow structure similar to what might be expected for a 'vortex breakdown'. For the larger swirl ratio, a central outflow, which seems to be independent from height, is present (Figure 6.1b and 6.2c). This is a flow behaviour similar to what is expected in a two-celled vortex structure. With increasing radial distance and heights > 0.01m, a radial inflow is detected for both swirl ratios, which seems to be height independent

and slightly larger (relative to the corresponding $u_{\theta,max,average}$, shown in table 6.2) for the lower swirl ratio (Figure 6.2b and 6.2d).
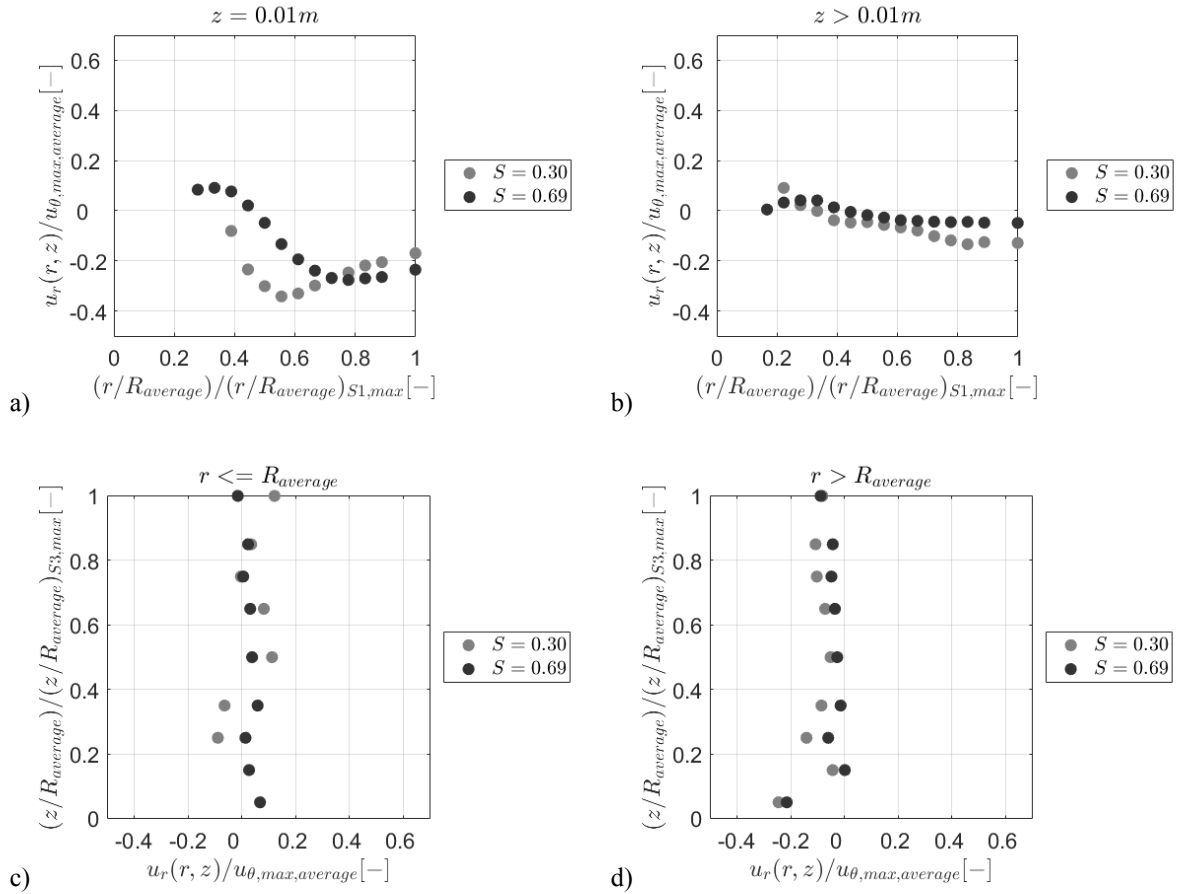
Figure 6.2: Radial velocity component in *S1* for $S = 0.30$ and $S = 0.69$. The radial profile of the lowest height is shown in (a), whereas the radial profile of height-averaged results is shown in (b). The vertical profile of radially averaged results inside and outside the vortex are illustrated in (c) and (d), respectively.

The radial profile of vertical velocities illustrates negative vertical velocities close to the simulator's surface for radial distances outside the corresponding vortex core (Figure 6.3a). This describes the downward directed inflow visible in figure 6.1a and 6.1b. With decreasing radial distance, the vertical velocity at the lowest height increases and becomes positive for both swirl ratios, which corresponds to a near-surface updraft inside the corresponding vortex core (Figure 6.3a). At greater heights ($z > 0.01$m), largest updraft velocities occur at an approximate

~ 110 ~

radial distance equal to the corresponding core radius, e.g., ~0.43 for $S = 0.30$ and ~0.55 for $S = 0.69$ (Figure 6.3b). For both swirl ratios, a weak height dependence can be inferred for vertical velocities outside the vortex core (Figure 6.3d). The vertical velocity increases with increasing height. Inside the vortex core, no clear height dependence is observed (Figure 6.3c). In general, normalised vertical velocities seem to be larger (relative to the corresponding $u_{\theta,max,average}$, shown in table 6.2) for the lower swirl ratio.
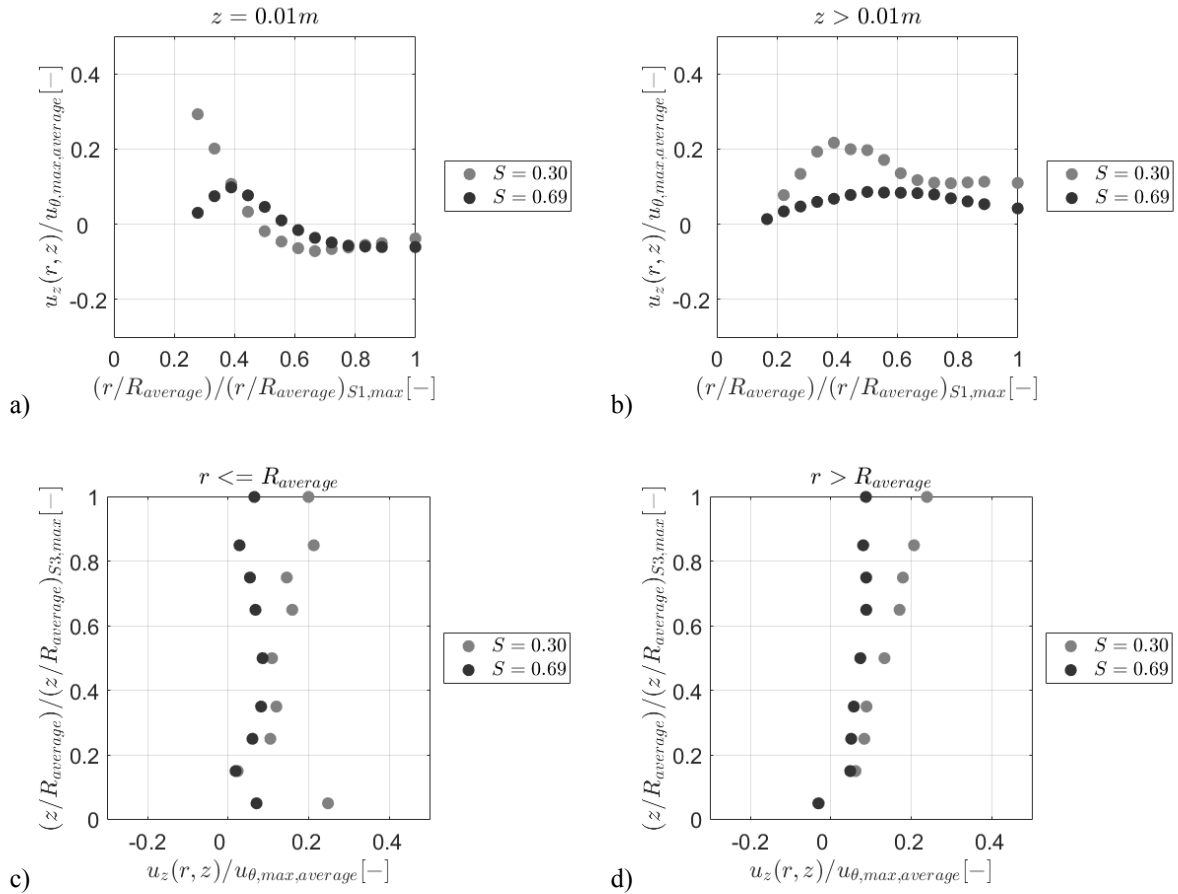
Figure 6.3: Vertical velocity component in *S1* for $S = 0.30$ and $S = 0.69$. The radial profile of the lowest height is shown in (a), whereas the radial profile of height-averaged results is shown in (b). The vertical profile of radially averaged results inside and outside the vortex are illustrated in (c) and (d), respectively.

6.2.2. *Surface pressure distribution*

Figure 6.4 illustrates the surface pressure distribution that arises as a result of the two flow fields investigated. The distribution of surface pressures obtained for $S = 0.30$ increases at a faster rate from the vortex centre towards larger radial distances compared to $S = 0.69$ (Figure 6.4). This behaviour can be explained by the different flow structures observed for $S = 0.30$ and $S = 0.69$, e.g., the relatively fast decay of the circumferential velocity component with increasing radial distance seems to cause a surface pressure distribution with a larger radial pressure gradient for $S = 0.30$.
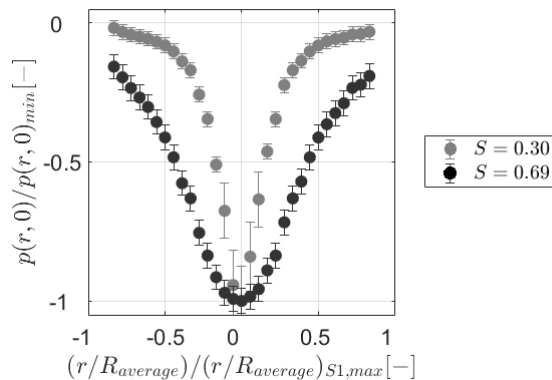
Figure 6.4: Surface pressure distributions in *S1* for $S = 0.30$ and $S = 0.69$. The uncertainty envelope represents the corresponding experimental measurement uncertainty of surface pressure measurements outlined in section 4.4.

6.3. *Comparison*

To assess the influence of the simulator's scale and corresponding geometric changes, flow field and surface pressure data obtained in *M1*, *S2*, *S3* and *S4* are compared to the reference flow and pressure fields of simulator *S1*. Differences between the velocity and surface pressure

fields are presented in terms of relative differences, normalised by the corresponding height-averaged circumferential velocity maximum. As will be demonstrated, in all cases, there are a number of similarities, e.g., for all swirl ratios in all simulators, the circumferential velocity component increases towards the core radius, reaches the overall maximum close to the surface, and decreases with increasing height in the lower heights. The general flow structure of the 2-D vector fields (based on the radial and vertical velocity components) show a similar flow behaviour outside the vortex core, with a strong radial inflow close to the surface up to the position where the overall (global) maximum of the circumferential velocity component occurs. At this position, the radial velocity weakens drastically and the vertical velocity increases significantly.

6.3.1. *The effect of the simulator's scale (T1)*

6.3.1.1. *Differences in the velocity field*
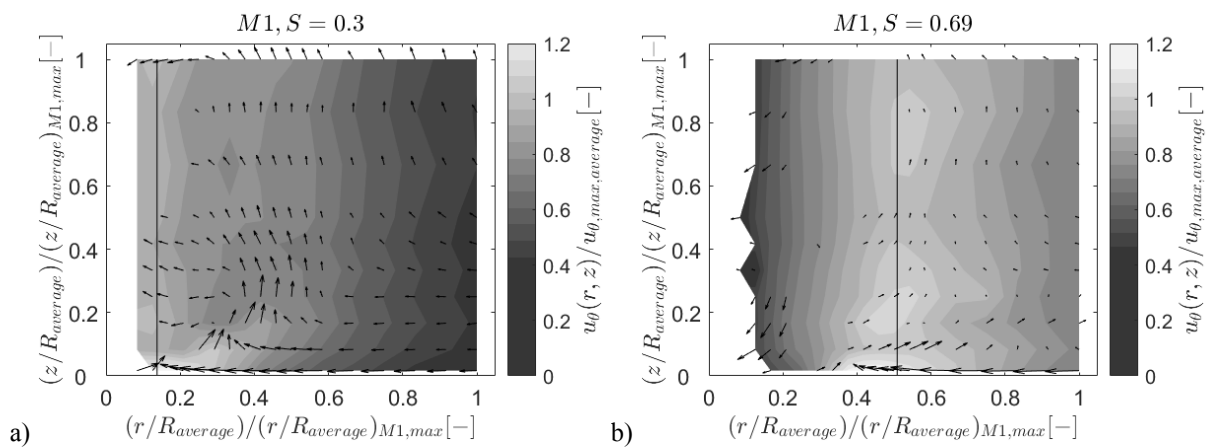
Figure 6.5: 3-D velocity fields in *M1* for *S = 0.30* (a) and *S = 0.69* (b). The normalised circumferential velocity component is shown as contour and the 2-D vector field indicates the vector based on the radial and vertical velocity component. The vertical solid black line indicates the corresponding location of the height-averaged core radius.

The 3-D velocity field obtained in the medium-scale simulator ($M1$) with $S = 0.30$ (Figure 6.5a), shows tentative evidence to suggest the presence of a counter-clockwise rotating cell near the surface close to the vortex centre covering a normalised area of approximately 0.25×0.25. At greater heights, the vortex core is dominated by radial inflow and an updraft, which turns into a downdraft at a normalised height of ~1. This in combination with the radial outflow from the vortex centre at $z = 0.01$m could suggest a narrow central downdraft, which penetrates all heights. For the same swirl ratio in $S1$ (Figure 6.1a), a very different flow field is observed - radial inflow velocities at lower heights inside the vortex centre, and the central radial outflow at larger heights have been interpreted as a flow structure similar to what might be expected for a 'vortex breakdown' with a central downdraft at greater heights.

With increasing swirl ratio in $M1$ ($S = 0.69$), a downdraft is detected in the vortex centre, which is likely to feed into the radial outflow at the lowest height at a normalised radial distance of ~0.3 (Figure 6.5b). This describes a flow structure, which might be expected for a two-celled vortex. For the same swirl ratio in $S1$, only positive vertical velocities were observed in the vortex core (Figure 6.1b). However, the weak radial outflow from the vortex centre led to the suggestion of a central downdraft.

Table 6.2: Averaged core radii, circumferential velocity maxima, surface pressure minima, relative and scaled radial / vertical distances and normalised core radii for *S1* and *M1*.

	S = 0.30		S = 0.69	
	S1	*M1*	*S1*	*M1*
$R_{average}$ *[m]*	0.077	0.083	0.100	0.305
$u_{\theta,max,average}$ *[m/s]*	5.38	7.45	6.92	8.75
p_{min} *[Nm^{-2}]*	-192.3	-225.2	-152.5	-174.4
$(r/R_{average})_{max}$	2.34	6.63	1.80	1.80
$(z/R_{average})_{max}$	2.60	7.23	2.00	1.97
$(r/R_{average})$ / $(r/R_{average})_{M1,max}$	0.35	1.00	1.00	1.00
$(z/R_{average})$ / $(z/R_{average})_{M1,max}$	0.36	1.00	1.02	1.00
$1 / (r/R_{average})_{M1,max}$	0.15		0.55	

The data presented in table 6.2 illustrate a decrease in magnitude of the surface pressure minimum *(p_{min})* with increasing swirl ratio in both simulators. This can potentially be an indication of a vortex transformation from a single-celled to a multiple-celled vortex. The flow fields in both simulators show tentative evidence of this transformation; however, both flow fields appear to be far more complex than a 'typical' single-celled or two-celled vortex structure might suggest. Furthermore, table 6.2 shows that despite the different scale of the simulators, maximum circumferential velocities *($u_{\theta,max,average}$)* in both simulators are of similar magnitude.

Maxima of normalised radial and vertical distances *($(r/R_{average})_{max}$* and *$(z/R_{average})_{max}$)* in *S1* and *M1* illustrate that flow fields measured for the same swirl ratio in the medium-scale and the small-scale simulator correspond to a different normalised radial / vertical area (Table 6.2). For *S* = 0.30 in *S1* for example, the flow field was captured within a normalised radial / vertical distance of 2.34 / 2.60, whereas in *M1* the flow field of a much larger normalised radial / vertical area of 6.63 / 7.23 could be determined (Table 6.2). Maximum circumferential velocities that occur at relatively small radial distances from the vortex centre in *M1* cause this difference.

Consequently, this results in a relatively small normalised $R_{average}$ of 0.15 in $M1$, compared to the simulator's size (Table 6.2). For the same swirl ratio in the small-scale simulator, the distribution of circumferential velocities causes a relatively large normalised $R_{average}$ of 0.43, compared to the simulator's size. Those differences are reflected in the normalisation of radial and vertical distances.

In order to ensure that only the relevant parts of the normalised flow fields are compared (and that the maximum amount of information is retained), the flow fields are scaled differently for each of the following comparisons, i.e., the normalised radial / vertical distance of vortices generated in simulator $S1$ are scaled by the normalised radial / vertical maximum, corresponding to the relevant comparison, i.e., $M1,max$ for the comparison study $T1$, $S3,max$ for the comparison study $T2$ and $S4,max$ for the comparison study $T3$ (see table 6.2, 6.3 and 6.4 for relevant scaling factors).

Table 6.2 illustrates that the flow field obtained in $S1$ for $S = 0.30$ is scaled to a normalised radial / vertical area of 0.35 / 0.36 (Table 6.2). Therefore, differences in the flow and surface pressure field illustrated in figure 6.6 and 6.7 can only be analysed up to this normalised radial / vertical distance. Figure 6.6 shows differences larger than the corresponding experimental measurement uncertainty between the flow fields obtained in $S1$ and $M1$ for both swirl ratios. Differences in the lowest measurement height ($z = 0.01$m) are shown as solid lines, whereas height-averaged differences at larger heights ($z > 0.01$m) are shown as dashed lines. The corresponding largest experimental measurement uncertainty is illustrated by the shaded area.
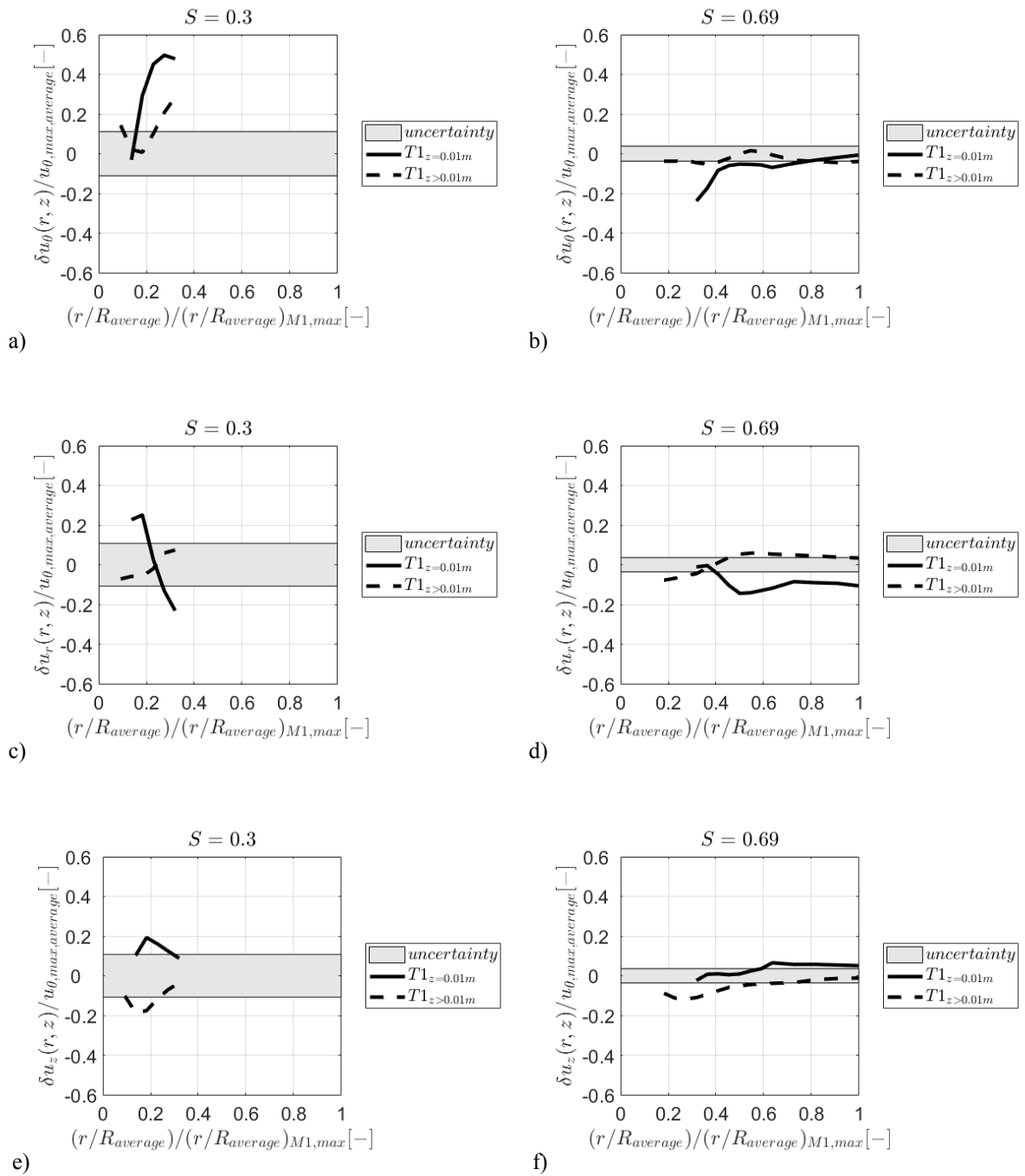
Figure 6.6: Differences between the radial profiles of circumferential (a and b), radial (c and d) and vertical (e and f) velocity components in *S1* and *M1*. The solid line indicates differences at the lowest measurement height ($z = 0.01$m) and the dashed line corresponds to (height-averaged) differences > 0.01m. The grey shaded area represents the corresponding larger experimental measurement uncertainty.

Outside the vortex core $((r/R_{average}) / (r/R_{average})_{M1,max} > 0.15)$, the radial profiles of circumferential velocity components obtained with the smaller swirl ratio differ significantly, especially at the lowest height, circumferential velocities are larger by about $0.5\delta\overline{u}_\theta$ in *M1* compared to *S1* (Figure 6.6a). Those differences are caused by the spatial compression of the flow field in the small simulator to a normalised area of 0.35×0.36 (Table 6.2).

For $S = 0.69$, the largest differences between the radial profiles of circumferential velocities occur inside the vortex core $((r/R_{average}) / (r/R_{average})_{M1,max} < 0.55)$ at the lowest measurement height (Figure 6.6b). Here, circumferential velocities obtained in the medium-scale simulator (*M1*) are lower by $\sim 0.2\delta\overline{u}_\theta$ compared to the small-scale simulator (*S1*). This means that circumferential velocities in *M1* decrease at a faster rate than in *S1*, from the vortex core towards the vortex centre. This is in good agreement with what is potentially expected for a two-celled vortex structure. The downdraft, which reaches the simulator's surface for $S = 0.69$ in *M1* (Figure 6.5b) seems to decreases the circumferential velocity close to the vortex centre. At larger heights ($z > 0.01$m), differences mostly lie within the experimental measurement uncertainty (Figure 6.6b).

Figure 6.6c shows differences between the radial profile of radial velocities for $S = 0.30$ in *M1* and *S1*. Those differences are about $\pm 0.2\delta\overline{u}_r$ in the lowest height ($z = 0.01$m), and are caused by the radial outflow at relatively small radial distances in *M1* (Figure 6.5a), which is not observed in *S1* (Figure 6.1a). With increasing radial distance, the radial inflow in *M1* dominates, whereas the inflow in *S1* already decreases, due to the spatial compression of the flow field.

For the larger swirl ratio, radial inflow velocities outside the vortex core are larger / lower by

about $\pm 0.1\delta\overline{u}_r$ in *M1* than *S1* for $z > 0.01$m and $z = 0.01$m, respectively (Figure 6.6d).

Figure 6.6e illustrates differences between the radial profiles of vertical velocity components in *M1* and *S1* of about $\pm 0.2\delta\overline{u}_z$ around the core radius. Those differences are caused by the downward directed radial inflow at the lowest measurement height in *S1* (Figure 6.1a), which was not observed in *M1* (Figure 6.5a). At larger heights, the flow field around the core radius in *S1* is dominated by vertical updraft, whereas in *M1*, radial inflow dominates, which results in lower vertical velocities in *M1* than *S1*.

For $S = 0.69$, differences of ~$0.1\delta\overline{u}_z$ between *M1* and *S1* are shown for the radial profile of vertical velocity components at heights > 0.01m inside the vortex core (Figure 6.6f). This can be explained by the downdraft captured in *M1* at relatively small normalised radial distances (*(r/R$_{average}$) / (r/R$_{average}$)$_{M1,max}$* < 0.4), whereas in *S1* this area is dominated by an updraft (Figure 6.1b and 6.5b).

Similar to figure 6.6, an analysis was undertaken to examine differences between the vertical profiles of circumferential, radial and vertical velocity components. In most cases, this supports the findings above, but does not contribute significantly to the discussion and as such, is not presented here. This transpires to be the case for all following simulator comparisons as well and for the sake of clarity and brevity, in what follows, discussions relating to the vertical profiles have been omitted in all cases.

6.3.1.2. *Differences in surface pressure distributions*

Figure 6.7 illustrates the differences in surface pressure fields between the small-scale and the medium-scale simulator. In general, the largest surface pressure differences are to be expected where the largest flow field differences were found. Therefore, it is not too surprising that the largest surface pressure differences are observed for $S = 0.30$. To capture those differences, the range for ordinates in figure 6.7 is adjusted to reach from $0.1\delta\bar{p}$ to $-0.6\delta\bar{p}$ instead of from $0.1\delta\bar{p}$ to $-0.3\delta\bar{p}$ as for the other comparison studies. Despite the differing magnitudes of surface pressure differences for $S = 0.30$ and $S = 0.69$, figure 6.7 shows that for both swirl ratios normalised surface pressures are generally lower in *M1* compared to *S1*. This consequently means that vortices generated in *M1* affect a larger normalised radial distance compared to *S1*. Those differences are found to be largest around the region of $R_{average}$.

The reason for surface pressure differences observed for the lower swirl ratio can largely be explained by the scaling issue addressed before. Similar to the flow field of *S1*, the surface pressure distribution is compressed into a normalised radial distance of ∓0.35. Consequently, this forces the surface pressure to increase at a much faster rate with increasing radial distance in *S1* than *M1*, thereby, causing the large surface pressure differences illustrated in figure 6.7a.

Differences observed for $S = 0.69$ could be caused by flow field differences inside the vortex core, where the central downdraft detected in *M1* potentially causes a more uniform surface pressure distribution around the vortex centre, thereby, causing a slower surface pressure increase with increasing radial distance from the vortex centre in *M1* than in *S1* (Figure 6.7b).

Figure 6.7: Surface pressure differences in *S1* and *M1* for *S* = 0.30 (a) and *S* = 0.69 (b). The grey shaded area represents the corresponding larger experimental measurement uncertainty.

6.3.2. The effect of the convection chamber height (T2)

In this section, the effect of changing the convection chamber height (H_2) in the small-scale generator (whilst keeping other geometric parameters and the swirl ratio constant) is investigated.

6.3.2.1. Differences in the flow field

The 3-D velocity fields obtained in *S2* (where the convection chamber height is reduced by ~38%) and *S3* (where the convection chamber height is reduced by ~75%) for both swirl ratios are shown in figure 6.8. In both cases, the vortex core ($r < R_{average}$) is dominated by radial outflow, which feeds into the updraft at a radial distance approximately equal to the corresponding core radius. This flow behaviour appears to become more distinct with decreasing H_2, irrespective of the swirl ratio. Furthermore, the relatively strong radial inflow close to the surface up to the position where the overall maximum circumferential velocity

occurs (shown in figure 6.1) appears to weaken with decreasing H_2 (Figure 6.8). For $S = 0.30$, the strong radial outflow and updraft observed in the vortex core of *S2* and *S3* suggests that the downdraft in *S1*, which seems to terminate aloft a stagnation point at a normalised height of approximately 0.3 (Figure 6.1a), lowers and reaches the surface of simulator *S2* and *S3* (Figure 6.8a and 6.8c).

The overall flow structures of all simulations for the larger swirl ratio suggest vortex structures similar to what might be expected in a two-celled vortex (Figure 6.1b, 6.8b and 6.8d). The radial outflow inside the vortex core obtained in *S1*, *S2* and *S3* suggests a central downdraft.
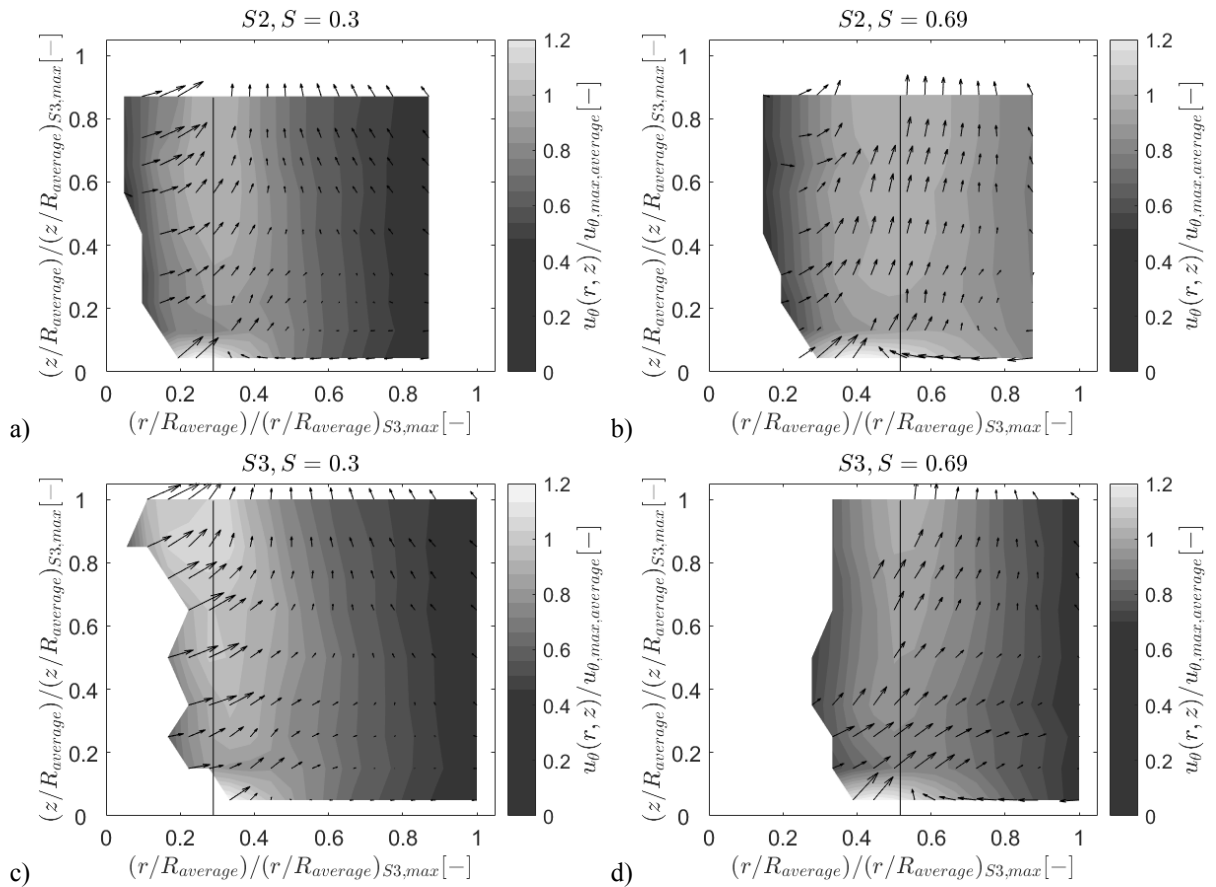
Figure 6.8: 3-D velocity fields in *S2* (a,b) and *S3* (c,d) for *S = 0.30* (a,c) and *S = 0.69* (b,d). The normalised circumferential velocity component is shown as contour and the 2-D vector field indicates the vector based on the radial and vertical velocity component. The vertical solid black line indicates the corresponding location of the height-averaged core radius.

The data embedded in table 6.3 illustrate that the maximum circumferential velocity ($u_{\theta,max,average}$) increases as H_2 decreases, i.e., this parameter varies in a range of 5.38m/s – 6.54m/s for $S = 0.30$. The same changes can also be observed for $S = 0.69$ with the maximum circumferential velocity varying from 6.92m/s – 8.16m/s. It is noted that differences in the circumferential velocity maximum between $S1$ and $S2$, and $S2$ and $S3$ are smaller than the corresponding uncertainty; however, differences between $S1$ and $S3$ are larger and therefore, can be assumed to be caused by the reduction of H_2 (Table 4.3 and 6.3). Also illustrated in the embedded data is the opposite trend for the core radius ($R_{average}$), i.e., the core radius decreases and varies in the range of 0.077m - 0.052m for $S = 0.30$. Similar to the circumferential velocity maxima, only when reducing H_2 by 75% ($S3$), differences larger than the experimental measurement uncertainty are obtained. As the swirl ratio increases, differences in $R_{average}$, which are larger than the uncertainty are only found for the vortex simulated in $S3$ compared to $S2$ (Table 4.3 and 6.3).

Differences of minimum surface pressures are masked by the experimental measurement uncertainty (Table 4.3 and 6.3).

Table 6.3: Averaged core radii, circumferential velocity maxima, surface pressure minima, relative and scaled radial / vertical distances and normalised core radii for $S1$, $S2$ and $S3$.

	$S = 0.30$			$S = 0.69$		
	$S1$	$S2$	$S3$	$S1$	$S2$	$S3$
$R_{average}$ [m]	0.077	0.060	0.052	0.100	0.107	0.093
$u_{\theta,max,average}$ [m/s]	5.38	5.96	6.54	6.92	7.22	8.16
p_{min} [Nm^{-2}]	-192.3	-190.9	-189.1	-152.5	-149.8	149.1
$(r/R_{average})_{max}$	2.34	3.00	3.46	1.80	1.68	1.94
$(z/R_{average})_{max}$	2.60	3.33	3.83	2.00	1.87	2.14
$(r/R_{average}) / (r/R_{average})_{S3,max}$	0.68	0.87	1.00	0.93	0.87	1.00
$(z/R_{average}) / (z/R_{average})_{S3,max}$	0.68	0.87	1.00	0.93	0.87	1.00
$1 / (r/R_{average})_{S3,max}$	0.29			0.52		

For more details, differences between the circumferential, radial and vertical velocity components for simulations conducted in $S1$, $S2$ and $S3$ are shown in figure 6.9 with respect to the radial distance. Figure 6.9 illustrates differences larger than the uncertainty for radial and vertical velocity components for both swirl ratios; although, differences between the flow fields of the lower swirl ratio seem to be more distinct. Differences between the radial profile of circumferential velocity components of both swirl ratios appear to be largely unaffected by the change in H_2 (Figure 6.9a and 6.9b). The largest differences are observed for the comparison of radial velocity components in $S1$, $S2$ and $S3$ for $S = 0.30$ (Figure 6.9c). Figure 6.9c illustrates that the radial velocity inside the vortex core at larger heights ($z > 0.01$m) increases significantly with decreasing H_2 by up to $0.2\delta\overline{u}_r$ in $S2$ and up to $0.4\delta\overline{u}_r$ in $S3$. As a result, the radial distance at which the central outflow turns into an inflow increases with decreasing H_2. For larger radial distances, differences remain present, but tend to decrease. Differences at the lowest measurement height (Figure 6.9c) illustrate the decreasing magnitude of radial inflow velocities with decreasing H_2 (Figure 6.1a, 6.8a, and 6.8c). This in combination with the radial outflow from the vortex centre, which was captured in $S2$ and $S3$ for $S = 0.30$, but not in $S1$, causes differences of up to $0.3\delta\overline{u}_r$ and $0.6\delta\overline{u}_r$ around the core radius of $S2$ and $S3$, respectively (Figure 6.9c). A similar trend can perhaps be inferred for radial velocity components of the larger swirl ratio; however, differences are not as significant as for $S = 0.30$ (Figure 6.9d).

Figure 6.9e and 6.9f show an updraft intensification with decreasing H_2 for both swirl ratios. Differences seem to be most distinct at the corresponding core radius, causing differences of up to $0.2\delta\overline{u}_r$ in $S2$ and up to $0.3\delta\overline{u}_r$ in $S3$ for $S = 0.30$ and differences of up to $0.1\delta\overline{u}_r$ in $S2$ and up to $0.2\delta\overline{u}_r$ in $S3$ for $S = 0.69$.
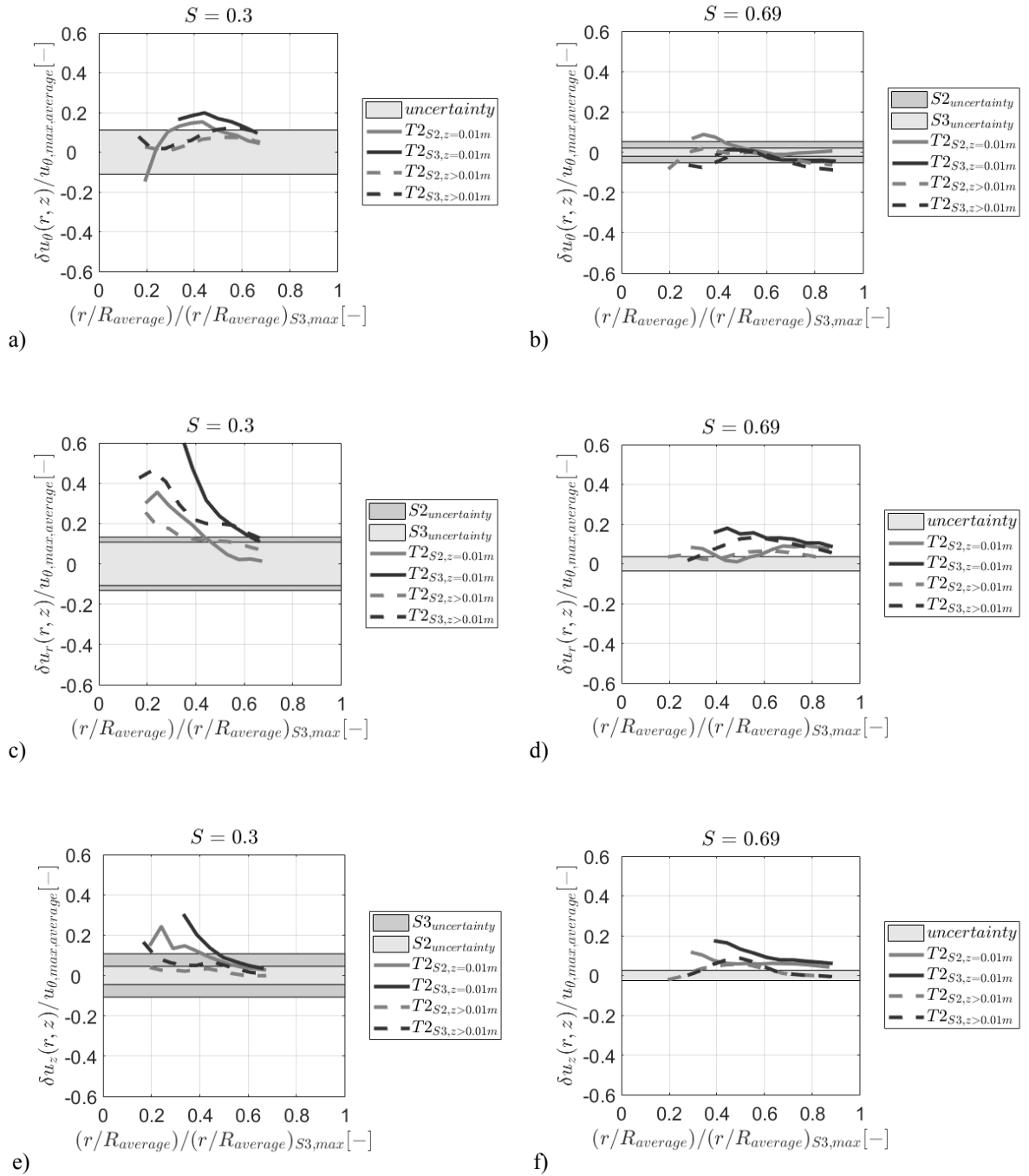
Figure 6.9: Differences between the radial profiles of circumferential (a and b), radial (c and d) and vertical (e and f) velocity components in *S1*, *S2* and *S3*. Differences at the lowest measurement height ($z = 0.01$m) are shown as solid line, whereas height-averaged differences for measurement locations > 0.01m are shown as dashed line. The grey shaded area corresponds to the corresponding larger experimental measurement uncertainty.

6.3.2.2.   *Surface pressure differences between S1, S2 and S3*

Differences of surface pressures measured in *S1*, *S2* and *S3* for $S = 0.30$ (a) and $S = 0.69$ (b) are presented in figure 6.10. For the lower swirl ratio, it appears that reducing H_2 causes the formation of vortices with a smaller radial surface pressure gradient (Figure 6.10a). As a result, the normalised radial distance affected by the vortex extends from *S1* to *S3*. This can partly be explained by the decreasing core radius with decreasing H_2 and the applied normalisation method for radial distances (Table 6.3).

For $S = 0.69$, an opposite trend is visible for the surface pressure distribution (Figure 6.10b). The surface pressure distribution in *S2* reveals larger surface pressures than in *S1*. A potential reason for this behaviour can be found in table 6.3. For $S = 0.69$, the core radius does not follow a clear trend with decreasing H_2 and the largest core radius is found for the vortex simulated in *S2*. This difference is reflected in the surface pressure distribution and results in a larger radial surface pressure gradient in *S2* than *S1*. The surface pressure distribution obtained in *S3* for the largest swirl ratio, shows differences, which lie within the corresponding uncertainty.

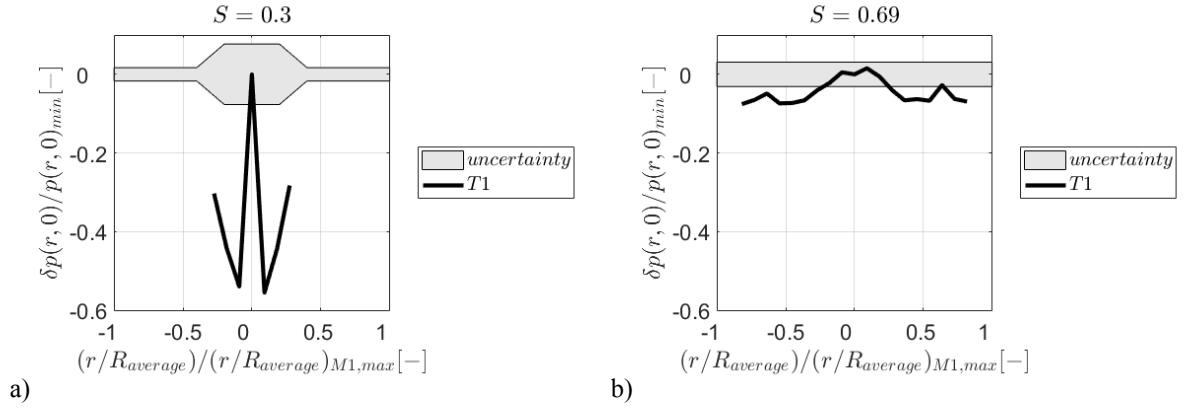a)   b)

Figure 6.10: Surface pressure differences in *S1*, *S2* and *S3* for $S = 0.30$ (a) and $S = 0.69$ (b). The grey shaded area represents the corresponding larger experimental measurement uncertainty.

6.3.3.   *The effect of the convergence chamber height (T3)*

In this section, the effect of changing the convergence chamber height (H_1) in the small-scale generator (whilst keeping other geometric parameters and the swirl ratio constant) is investigated.

6.3.3.1.   Flow field differences

The 3-D velocity fields obtained in *S4* for $S = 0.30$ (a) and $S = 0.69$ (b) are shown in figure 6.11. For the lower swirl ratio, flow fields in *S1* and *S4* show a similar behaviour - the central downdraft, which stagnates at a normalised height of ~0.3 in *S1* (Figure 6.1a) seems to lower to approximately ~0.15 in *S4* (Figure 6.11a). At this height, the downdraft is assumed to feed into the radial outflow from the vortex centre.

Flow fields obtained for $S = 0.69$ in *S1* and *S4* also reveal a similar flow pattern. The upwards directed radial outflow at all heights in the vortex centre of *S1* (Figure 6.1b) and *S4* (Figure 6.11b) suggests the presence of a central downdraft that reaches the surface of both simulators. This suggests the presence of a large counter-clockwise rotating cell as potentially expected in a two-celled vortex structure.

In addition, table 6.4 shows the height-averaged core radius, the maximum circumferential velocity and the minimum surface pressure. It is noted, that differences between parameters presented in table 6.4 are smaller than the experimental measurement uncertainty and therefore, differences are expected to be independent of the H_1 reduction. This is perhaps not surprising, considering the relatively small reduction of H_1 of only 25% from *S1* to *S4*.
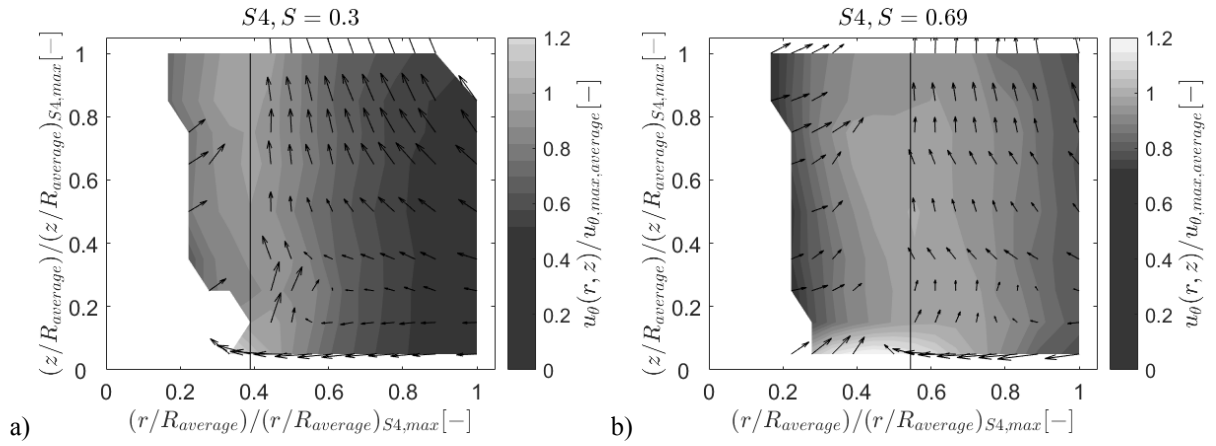
Figure 6.11: 3-D velocity fields in *S4* for *S = 0.30* (a) and *S = 0.69* (b). The normalised circumferential velocity component is shown as contour and the 2-D vector field indicates the vector based on the radial and vertical velocity component. The vertical solid black line indicates the corresponding location of the height-averaged core radius.

Table 6.4: Averaged core radii, circumferential velocity maxima, surface pressure minima, relative and scaled radial / vertical distances and normalised core radii for *S1* and *S4*.

	S = 0.30		S = 0.69	
	S1	*S4*	*S1*	*S4*
$R_{average}$ [m]	0.077	0.070	0.100	0.098
$u_{\theta,max,average}$ [m/s]	5.38	5.57	6.92	6.79
p_{min} [Nm⁻²]	-192.3	-192.3	-152.5	-151.0
$(r/R_{average})_{max}$	2.34	2.57	1.80	1.84
$(z/R_{average})_{max}$	2.60	2.86	2.00	2.04
$(r/R_{average})$ / $(r/R_{average})_{S4,max}$	0.91	1.00	0.98	1.00
$(z/R_{average})$ / $(z/R_{average})_{S4,max}$	0.91	1.00	0.98	1.00
$1 / (r/R_{average})_{S4,max}$	0.39		0.54	

Figure 6.12 shows that altering the height of the convergence chamber by ~25% appears to have the least effect – all of the differences illustrated are within the experimental measurement uncertainty, with the exception of a few points inside the vortex core. There is tentative evidence to suggest that the radial outflow feeding into the updraft inside the vortex core (Figure 6.12c and 6.12d), and vertical velocities in general (Figure 6.12e and 6.12f), become more distinct

when decreasing H_I. Although, it is acknowledged that this is within the experimental measurement uncertainty and as such is speculation.
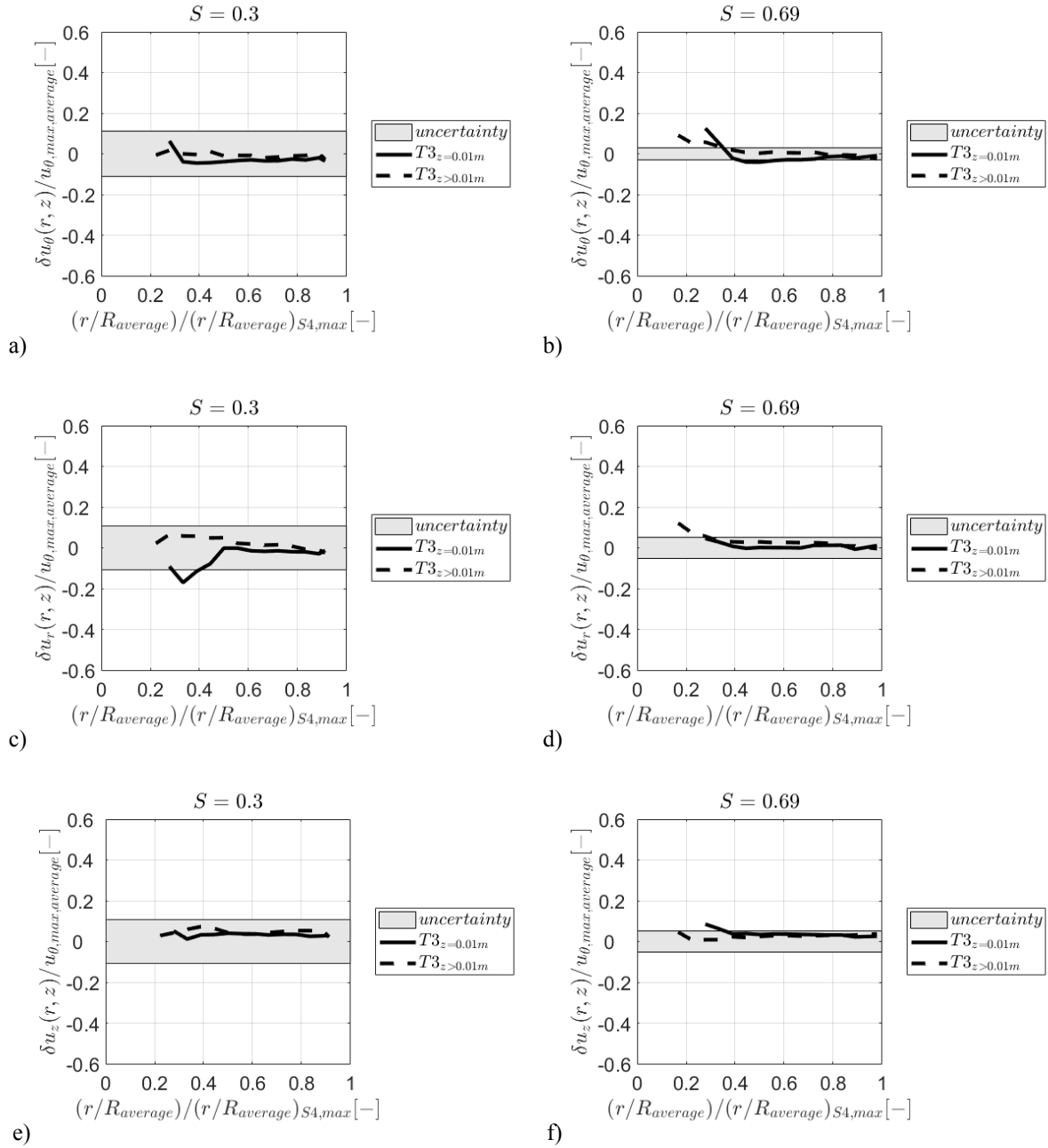
Figure 6.12: Differences between the radial profiles of circumferential (a and b), radial (c and d) and vertical (e and f) velocity components in *S1* and *S4*. Differences at the lowest measurement height ($z = 0.01$m) are shown as solid line, whereas height-averaged differences for measurement locations > 0.01m are shown as dashed line. The grey shaded area corresponds to the corresponding larger experimental measurement uncertainty.

6.3.3.2.   *Surface pressure differences*

Figure 6.13 shows differences between the surface pressures measured in *S1* and *S4* for *S* = 0.30 (a) and *S* = 0.69 (b). It seems that also the surface pressure distributions are largely unaffected by the change of the convergence chamber height, as most surface pressure differences lie within the corresponding experimental measurement uncertainty. Only around the core radius of *S* = 0.30, a weak dependence can be inferred with slightly smaller normalised surface pressures in *S4* (Figure 6.13a). This difference can potentially be explained by a combination of the lowering of the downdraft's stagnation point and the decreasing core radius with decreasing H_1, thereby, causing a surface pressure distribution with a smaller radial surface pressure gradient in *S4* than *S1*.

For the larger swirl ratio, a weak dependence on H_1 can be inferred as well, causing slightly larger normalised surface pressures in *S4* compared to *S1* (Figure 6.13b). The increasing vertical velocity at the lowest height could be a potential reason for this behaviour, causing a vortex with a larger radial surface pressure gradient with decreasing H_1. Although, it is acknowledged that differences lie within the experimental measurement uncertainty and as such is speculation.

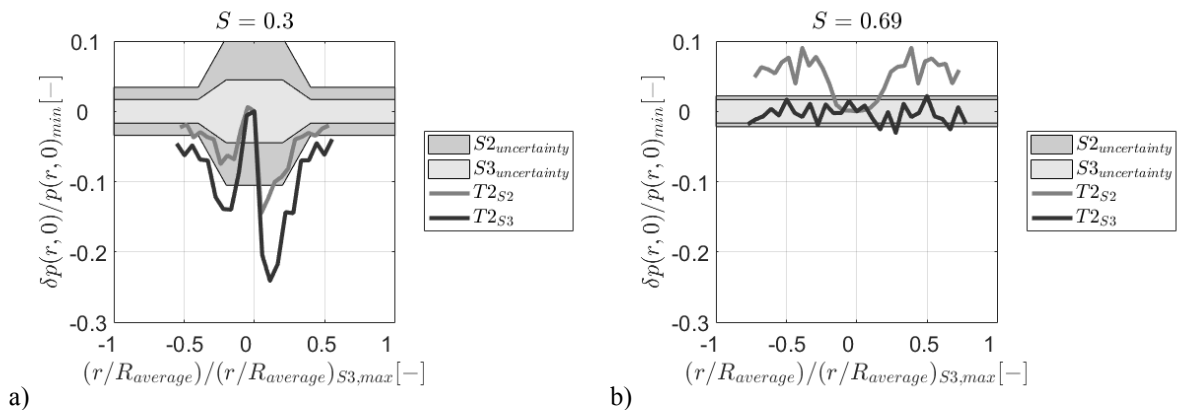a)   b)
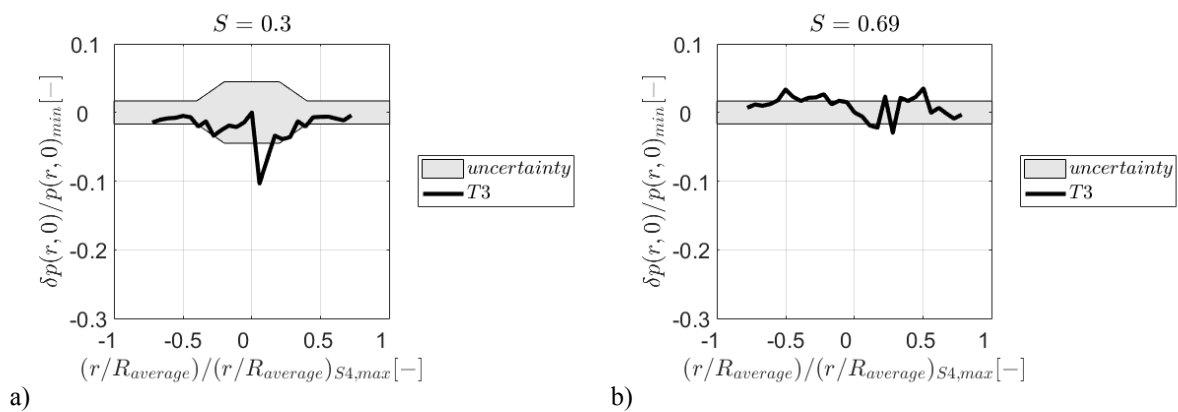
Figure 6.13: Surface pressure differences in *S1* and *S4* for *S* = 0.30 (a) and *S* = 0.69 (b). The grey shaded area corresponds to the corresponding larger experimental measurement uncertainty.

6.4. Concluding remarks

Based on this analysis, the following main conclusions can be drawn:

- Time-averaged velocity and surface pressure data have been presented and illustrate (in keeping with previous work) that the swirl ratio has an effect on the size of the core radius, pressure distribution and velocity characteristics.

- Velocity and surface pressure characteristics of vortices generated in simulators of different scale but swirl ratio and aspect ratio parity can differ significantly.

- Flow field and surface pressure characteristics of tornado-like vortices appear not only to be a function of the swirl ratio and the aspect ratio, but also a function of the convection chamber height.

- Reducing the convergence chamber height by 25% and thereby changing the aspect ratio from 2 to 1.5 showed little effect on velocity and surface pressure fields.

- It was found that the effect of different simulator scales and geometric modifications on the flow and surface pressure field can be swirl ratio dependent.
  - For $S = 0.30$, differences of up to 50% were found between surface pressures and circumferential velocity components of vortices generated in simulators of different scale, whereas the majority of differences observed for $S = 0.69$ remained below 20%.
  - For $S = 0.30$, differences of up to 30% and 60% were found between radial velocity components when reducing the convection chamber height by 38% and 75%,

respectively, whereas differences for $S = 0.69$ remained below 20%.

- It is noted that there are a variety of ways in which the pressure and velocity data could be normalised and it seems possible that different normalisations could mask or exaggerate the impact of geometric changes on the generated flow field.

Based on the above, it is suggested that ensuring aspect ratio and swirl ratio parity between different simulators is not sufficient to generate similar vortices with similar velocity and surface pressure characteristics, i.e., the boundary conditions govern the flow.

7. AN ANALYSIS OF TRANSIENT PROCESSES IN TORNADO-LIKE FLOWS

The relatively large fluctuations of local static surface pressures at the centre of the simulators with respect to time (section 4.4) suggested that a detailed investigation of the transient behaviour was warranted. The analysis relating to this investigation is reported in this section. It is acknowledged that parts of this research have previously been published in *Gillmeier et al. (2017)* and are reproduced with the permission of the co-authors.

7.1. Temporal and spatial distributions of surface pressures

The focus of most physical simulations to date concerns the generation of realistically looking tornado-like flow fields, generally expressed in terms of mean flow velocities and mean surface pressure distributions. Surprisingly, there is as of yet, little understanding about the effect and relative importance of transient (non-stationary) processes (e.g., the spatial movement of the vortex centre with time) on the tornado flow and surface pressure field (e.g., *Karami et al., 2017*).

In order to investigate the transient behaviour of vortices generated in the medium-scale (*M1*) and the small-scale (*S1*) tornado-like vortex simulator at the *UoB*, surface pressures obtained for three swirl ratios ($S = 0.14$, $S = 0.30$ and $S = 0.69$) will be analysed in this section. The focus of this analysis lies on surface pressure measurements because findings presented in section 4.4 give reason to suggest that transient phenomena occur either at the centre of the simulator or at relatively small radial distances from the vortex centre for which velocities could not be captured with the desired data quality.

Figure 7.1 shows surface pressure measurements in *S1* (a) and *M1* (b), which were obtained at the corresponding simulator's centre (a_1, b_1) and at corresponding core radii (a_2, b_2) in form of a box plot. Each box plot provides information of the median (horizontal line in the box), the first and third quartile (top and bottom of the box), and the remaining sample points (dots) of the corresponding surface pressure distribution. Surface pressures illustrated in figure 7.1 have been normalised by the corresponding time-averaged surface pressure minimum (p_{min}), which is given in the figure's caption.

In order to investigate and highlight differences between the analysed distributions, the skewness (ς) and the kurtosis (κ) have been calculated to describe the shape of frequency distributions. The skewness is the third statistical moment of a distribution and a measure of the symmetry of the distribution in relation to the normal distribution. A skewness of zero corresponds to the normal distribution, whereas a negative skewness means that the distribution has a tail, which extends further towards the left-hand side than the right-hand side and vice versa for a positively skewed distribution. The kurtosis is the fourth statistical moment of a frequency distribution and is a measure of the likelihood of a distribution to produce outliers in

relation to the normal distribution (*Rohatgi, 1976*). For this work, κ was calculated based on the definition given in *Pearson (1905)*, for which outliers are defined by values larger / smaller than three times the standard deviation, σ, of the corresponding distribution. A kurtosis of zero corresponds to the normal distribution, whereas if $\kappa > 0$, the tails of the distribution extend further than the tails of a normal distribution. Consequently, a frequency distribution of positive kurtosis has a larger likelihood for outliers than a normal distribution.

Table 7.1 provides information of skewness and kurtosis of the distributions illustrated in figure 7.1. In addition, the corresponding standard deviation is shown in percentage of p_{min}.
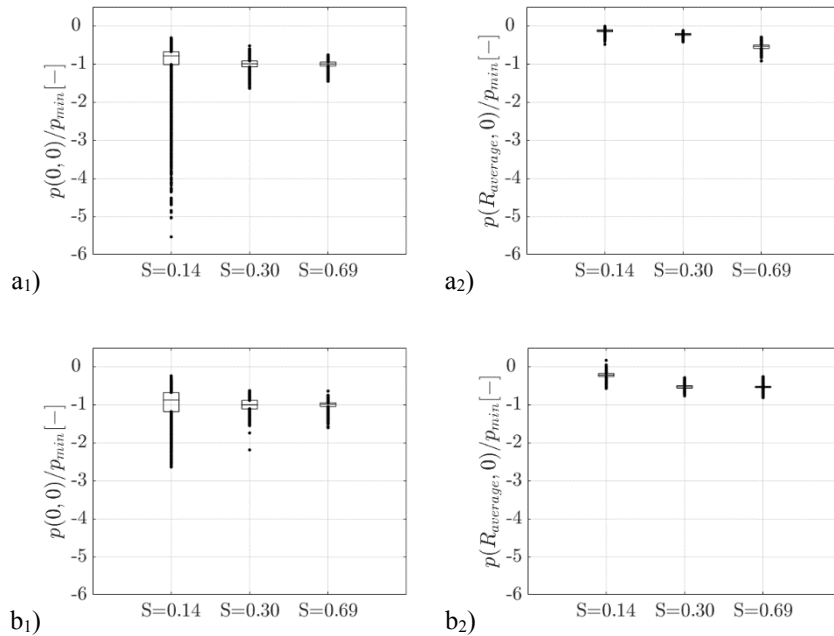
Figure 7.1: Box plot of surface pressure measurements obtained in *S1* (a) and *M1* (b) for different radial distances, $r = 0$ ($_1$) and $r = R_{average}$ ($_2$). For $S = 0.14$, $S = 0.30$ and $S = 0.69$ in *S1* p_{min} =-123.5Nm^{-2}, -192.3Nm^{-2} and -152.5Nm^{-2}, respectively. In *M1*, corresponding p_{min} values are -168.1Nm^{-2}, -225.2Nm^{-2} and -174.4Nm^{-2}.

Table 7.1: Standard deviation, skewness and kurtosis of surface pressure time series illustrated in figure 7.1 for *S1* (a) and *M1* (b) and different radial positions, $r = 0$ (1) and $r = R_{average}$ (2).

a1)

	S = 0.14	S = 0.30	S = 0.69
σ [%]	61.9	12.5	8.4
ς [-]	-2.7	-0.4	-0.6
κ [-]	8.4	0.9	0.9

a2)

S = 0.14	S = 0.30	S = 0.69
3.9	3.6	6.9
-1.0	-0.4	-0.3
3.7	0.7	0.3

b1)

	S = 0.14	S = 0.30	S = 0.69
σ [%]	46.1	15.0	8.6
ς [-]	-1.2	-0.4	-1.0
κ [-]	6.8	0.3	2.3

b2)

S = 0.14	S = 0.30	S = 0.69
6.5	5.1	3.5
-0.7	-0.1	-0.1
1.7	0.3	0.9

Figure 7.1a1 and figure 7.1b1 illustrate that the instantaneous surface pressure deficit at the centre of the vortex for the lowest swirl ratio ($S = 0.14$) can be larger than the average surface pressure deficit (p_{min}) by almost 6 times in *S1* and almost 3 times in *M1*. This behaviour is reflected in the corresponding statistical quantities presented in table 7.1a1 an table 7.1b1. For $S = 0.14$, standard deviations of approximately 62% and 46% of the corresponding p_{min} value highlight the large instantaneous variability in time at the vortex centre of *S1* and *M1*, respectively (Table 7.1a1 and 7.1b1). Furthermore, the relatively large kurtosis of those distributions ($\kappa = 8.4$ in *S1* and $\kappa = 6.8$ in *M1*) suggests heavily tailed frequency distributions with outliers much larger than three times the corresponding standard deviation. In addition, the negative skewness of $\varsigma = -2.7$ in *S1* and $\varsigma = -1.2$ in *M1* (Table 7.1a1 and 7.1b1) allows the conclusion to be drawn that frequency distributions at the vortex centre of both simulators are heavily tailed towards the negative side of the frequency distribution. This results in an increasing likelihood of an instantaneous decrease of the central surface pressure deficit for $S = 0.14$.

The surface pressure distributions obtained at the corresponding core radii in *S1* (Figure 7.1a$_2$) and *M1* (Figure 7.1b$_2$) for the lowest swirl ratio ($S = 0.14$) remain slightly left tailed (positive kurtosis and negative skewness); however, the shape of those distributions shows a behaviour more similar to what is expected for a normal distribution (Table 7.1a$_2$ and 7.1b$_2$). Hence, it is suggested that relatively large surface pressure fluctuations with respect to time seem to occur solely at, or in close proximity to the centre of both simulators for vortices simulated with the lowest swirl ratio ($S = 0.14$).

With increasing swirl ratio, results presented in table 7.1a and 7.1b illustrate that surface pressure distributions obtained at the centre of the simulators and at corresponding core radii also retain a slightly left tailed shape but become more similar to a shape that would be expected for a normal distribution.

In keeping with findings presented in section 4.4, differences between the shapes of surface pressure distributions obtained at the centre of both simulators and at corresponding core radii, seem to decrease with increasing swirl ratio, e.g., no radial dependence on the shape of surface pressure distributions was observed for the largest swirl ratio ($S = 0.69$) in both simulators over the range of radial distances analysed (Figure 7.1 and table 7.1). In conclusion, it seems that the magnitude of local surface pressure fluctuations at the centre of the simulators decreases with increasing swirl ratio.

In addition to the temporal distribution of surface pressure measurements, figure 7.2 illustrates the non-stationary movement of the vortex centre (which is defined as the local surface pressure minimum of the vortex at any time) for $S = 0.14$, $S = 0.30$ and $S = 0.69$ in *S1* (a) and *M1* (b).

The corresponding percentages show relative durations (relative to the entire measurement period) for which the vortex centre is located in any of the four quadrants. As the duration for which the vortex centre coincides with the simulator's centre is not accounted for in this analysis, percentages shown in figure 7.2 do not integrate to 100 as illustrated in table 7.2, which provides an overview of the entire duration for which the corresponding vortex is not located at the centre of the corresponding simulator. For this investigation, pressure taps surrounding the corresponding simulator's centre in a circular pattern (as illustrated in figure 4.2a and figure 4.2b for *S1* and *M1*, respectively) were analysed.

		y				*y*			
18[%]		29[%]		23[%]		29[%]		$S = 0.69$	
23[%]		6[%]		19[%]		10[%]		**S = 0.30**	
14[%]		1[%]		4[%]		10[%]		$S = 0.14$	
			x				*x*		
29[%]		19[%]		20[%]		26[%]			
29[%]		10[%]		17[%]		4[%]			
17[%]		5[%]		8[%]		12[%]			

a)   b)
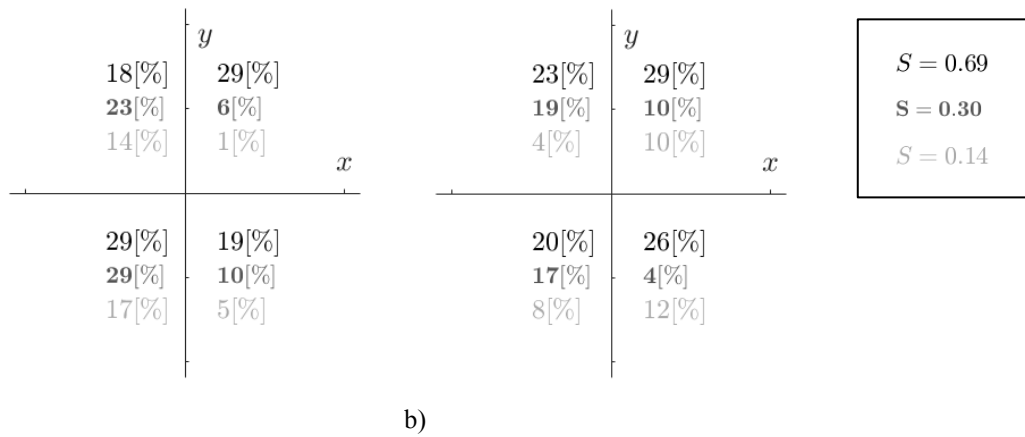
Figure 7.2: Percentage of the measurement time for which the local surface pressure minimum occurs in any of the four quadrants surrounding the simulator's centre $(x,y) = (0,0)$ for $S = 0.14$, $S = 0.30$ and $S = 0.69$ in *S1* (a) and *M1* (b).

Table 7.2: Relative duration of vortex movement in percentage of the measurement duration in *S1* and *M1* for $S = 0.14$, $S = 0.30$ and $S = 0.69$.

	S = 0.14	*S = 0.30*	*S = 0.69*
Duration of vortex movement in S1	*37 %*	*68 %*	*95 %*
Duration of vortex movement in M1	*34 %*	*50 %*	*98 %*

Table 7.2 shows that with increasing swirl ratio, the duration for which the corresponding vortex centre is not located at the centre of the simulator increases from ~37% to ~68% to ~95% for *S*

= 0.14, $S = 0.30$ and $S = 0.69$ in *S1* and from ~34% to ~50% to ~98% for $S = 0.14$, $S = 0.30$ and

$S = 0.69$ in *M1*. Detailed information regarding the location of the corresponding vortex centre

throughout the entire measurement duration is provided in figure 7.2. If observed movement

patterns had shown a more symmetric behaviour with respect to the simulators' centre, a regular

vortex movement could have been inferred. However, results presented in figure 7.2 are not

distinct enough to draw this conclusion, as a certain degree of randomness seems to be present

for the vortex movement of all analysed vortices in both simulators (Figure 7.2).

Defining the vortex centre as the position at which the lowest surface pressure is located, i.e.,

$r(x,y)_{p_{min}}$, it is possible to calculate a potential normalised vortex wandering velocity from:

$$u_{vortex\ wandering}(x, y, \Delta t) = \frac{\Delta r(x,y,\Delta t)_{p_{min}} f}{u_{\theta,max,average}} \tag{7.1}$$

where, $\Delta r(x,y,\Delta t)_{p_{min}} = \Delta r(x,y,t+1)_{p_{min}} - \Delta r(x,y,t)_{p_{min}}$, f is the sampling frequency of surface

pressure measurements (for this work $f = 100$Hz) and $u_{\theta,max,average}$ is the height-averaged

maximum circumferential velocity throughout the entire sampling period. Values of which are

given in the caption of figure 7.3. It is noted that an uncertainty is introduced to the vortex

wandering velocity due to the surface pressure tap spacing. Because of this, differences of

vortex wandering velocities, which are lower than 10%, 9% and 7% of the corresponding

$u_{\theta,max,average}$ for $S = 0.14$, $S = 0.30$ and $S = 0.69$ in *S1* cannot be detected. Due to the larger

spacing between pressure taps in *M1*, corresponding percentages are 70%, 35% and 30%.

Figure 7.3 illustrates the results of this analysis expressed in terms of a frequency distribution of vortex wandering velocities for $S = 0.14$, $S = 0.30$ and $S = 0.69$ in $S1$ (a) and $M1$ (b). The vortex simulated in $S1$ for $S = 0.14$ mainly moves with a velocity of ~30% of the corresponding $u_{\theta,max,average}$ (Figure 7.3a). For the second largest swirl ratio, the vortex centre typically moves at velocities of around 20% of $u_{\theta,max,average,(S=0.30)}$, and the vortex generated with the largest swirl ratio ($S = 0.69$) appears to be continuingly moving with velocities between 10% - 80% of its $u_{\theta,max,average}$. In addition, figure 7.3a highlights that vortex wandering velocities of all vortices simulated in $S1$ are lower or equal to the corresponding circumferential velocity maximum ($u_{\theta,max,average}$). Therefore, from figure 7.3, it can be concluded that relative vortex wandering velocities in $M1$ seem to be larger than in $S1$ for all vortices. Vortex wandering velocities of all vortices simulated in $M1$ exceed the corresponding circumferential velocity maximum (figure 7.3b). The vortex simulated with the lowest swirl ratio in $M1$ seems to move with velocities of about 1.4 to 2.6 times the corresponding $u_{\theta,max,average}$ (Figure 7.3b). For the second largest swirl ratio, the vortex mainly moves with velocities between 40% and 120% of its $u_{\theta,max,average}$, even though, occasionally, vortex wandering velocities can be significantly larger (up to 2.8 times $u_{\theta,max,average,(S=0.30)}$). The vortex with the largest swirl ratio seems to be mainly moving with a speed approximately similar to its circumferential velocity maximum. For the remaining time, the vortex moves with velocities of approximately 1.2 to 3.2 times of its corresponding $u_{\theta,max,average}$.
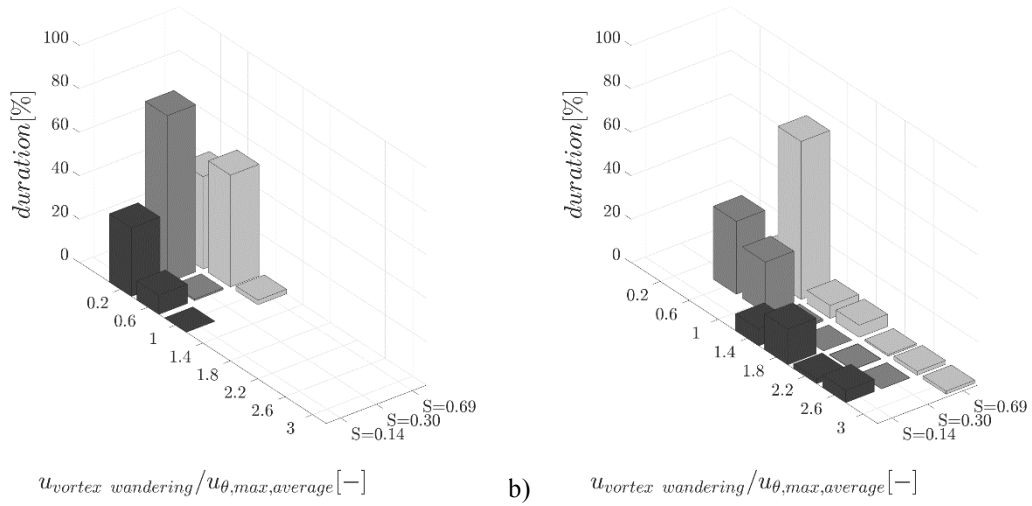
Figure 7.3: Transient vortex wandering velocities for all swirl ratios in *S1* (a) and *M1* (b). In *S1*, $u_{\theta,max,average}$ = 3.69m/s, 5.38m/s and 6.92m/s for *S* = 0.14, *S* = 0.30 and *S* = 0.69, respectively. In *M1*, corresponding values are 3.65m/s, 7.45m/s and 8.75m/s for *S* = 0.14, *S* = 0.30 and *S* = 0.69, respectively.

It is postulated that the transient behaviour in time and space outlined above could possibly be associated with a combination of a transient vortex intensifying / weakening in time and a non-stationary movement of the vortex centre in time (e.g., vortex wandering). In order to investigate the non-stationary temporal and spatial behaviour further, the technique of proper orthogonal decomposition (*POD*) is used in an attempt to decouple the influence of a possible vortex wandering and a potential vortex intensifying / weakening in time, from the mean flow field.

7.2. *Proper Orthogonal Decomposition (POD) of surface pressure fluctuations*

The *POD* method assumes that surface pressure fluctuations can be represented by a series of spatial and temporal functions, which are the eigenvectors (modes) and the mean square values of the eigenvalues of the pressure fluctuation covariance matrix (*Baker, 2000*). The significance of certain modes is determined by their corresponding eigenvalue because the eigenvalue represents the amount of 'energy' that is carried by the associated mode, hence, the eigenvalue also indicates the degree to which this mode might represents the actual surface pressure fluctuations. In practice it is found that only the first few modes contain significant energy (*Baker, 2000*). Consequently, in theory, the most relevant features of the surface pressure fluctuations can be represented by those first few ('most energetic') modes.

For this work, the *POD* analysis yields 41 modes (due to the 41 experimental measurement positions illustrated in figure 4.2). Figure 7.4 shows the cumulative 'energy' within the first ten modes for *S1* (a) and *M1* (b) for all swirl ratios (as given by the sum of the eigenvalues up to that mode). It can be observed that the eigenvalues of the lower modes contribute significantly more to the total 'energy' in the flow than the higher modes. In particular, the first three modes are responsible for approximately 50% or more of the total 'energy'. This was found to be the case for both simulators and all swirl ratios investigated. For $S = 0.14$, about 90% of the total 'energy' is given within the first three modes. In what follows, the first three modes are analysed in more detail for all swirl ratios, as those are the modes, which individually contain a significant amount of 'energy' of at least around 20% of the total 'energy', and therefore, might

be expected to correspond to physical flow mechanisms. The individual contribution of higher modes (modes > 3) is relatively small and for that reason, it is unlikely that those modes represent coherent physical phenomena.
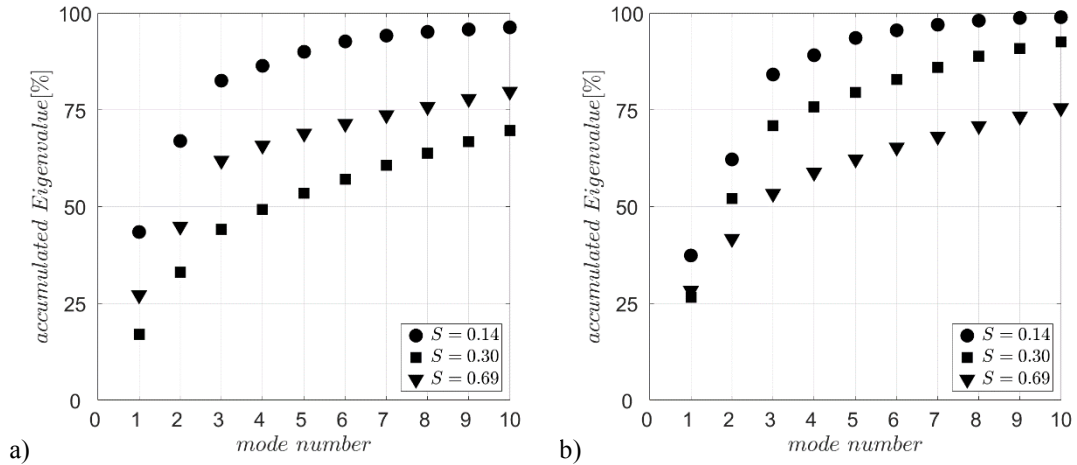
Figure 7.4: Normalised accumulated eigenvalues in *S1* (a) and *M1* (b) for the first ten modes and three swirl ratios ($S = 0.14$, $S = 0.30$ and $S = 0.69$).

Figures 7.5 and 7.6 show the eigenvectors of the first ($_1$), second ($_2$) and third ($_3$) mode for $S = 0.14$ (a), $S = 0.30$ (b) and $S = 0.69$ (c) in *S1* and *M1,* respectively. The eigenvector of the first mode for the lowest swirl ratio ($S = 0.14$) shows a strong gradient in 'energy' towards the centre in *S1* and *M1* (Figure 7.5a_1 and 7.6a_1). A similar behaviour can be found for the eigenvector of the third mode for $S = 0.30$ (Figure 7.5b_3 and 7.6b_3) and the eigenvector of the first mode for $S = 0.69$ (Figure 7.5c_1 and 7.6c_1) in both simulators. However, the 'energy' gradient towards the centre decreases with increasing swirl ratio, which can be explained by the different amount of 'energy' carried by those modes (Figure 7.4). Figure 7.5 and 7.6 also show relatively strong regions of positive and negative eigenvalues, suggesting an oscillation in the energy for modes 2 and 3 ($S = 0.14$), modes 1 and 2 ($S = 0.30$), and modes 2 and 3 ($S = 0.69$). It is perhaps worth noting that figure 7.5 and 7.6 represent the 'energy' over the sampling period and instantaneous distributions support the notion of oscillation, since the areas of localised maximum / minimum

~ 143 ~

change sign throughout the sampling period (instantaneous distributions for *S1* can be viewed here: *https://instantaneousdistributions.neocities.org/*). It is hypothesised that this oscillation might be indicative of a circular vortex movement for all swirl ratios in both simulators, which could in turn be indicative of vortex wandering.

The relative radial distance of the localised maximum / minimum (or potentially the region of vortex wandering), with respect to the corresponding core radius, appears to remain constant for all swirl ratios at approximately 0.3 $R_{average}$ in *S1* (Figure 7.5). In *M1* (Figure 7.6), the relative distance (with respect to the corresponding core radius) increases compared to *S1* but remains also constant at approximately 0.5 $R_{average}$ for all swirl ratios.
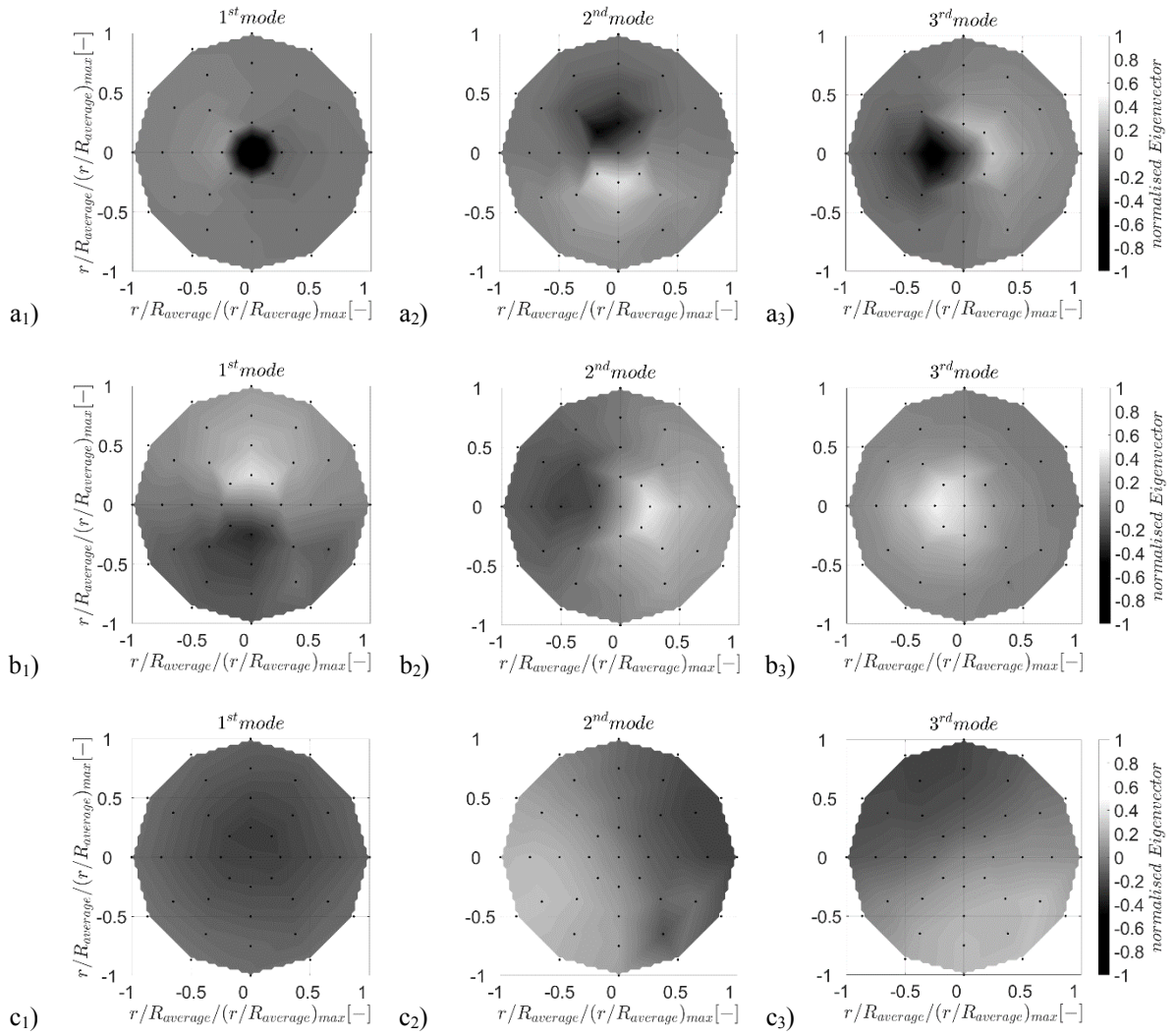
Figure 7.5: Normalised eigenvectors for the first ($_1$), second ($_2$) and third ($_3$) mode in *S1* for $S = 0.14$ (a), $S = 0.30$ (b) and $S = 0.69$ (c), respectively. To normalise the radial distance, maximum values of experimentally obtained *(r/R$_{average}$)$_{max}$* are used. For $S = 0.14$, $S = 0.30$ and $S = 0.69$ *(r/R$_{average}$)$_{max}$* = 0.83, 0.52 and 0.40, respectively.
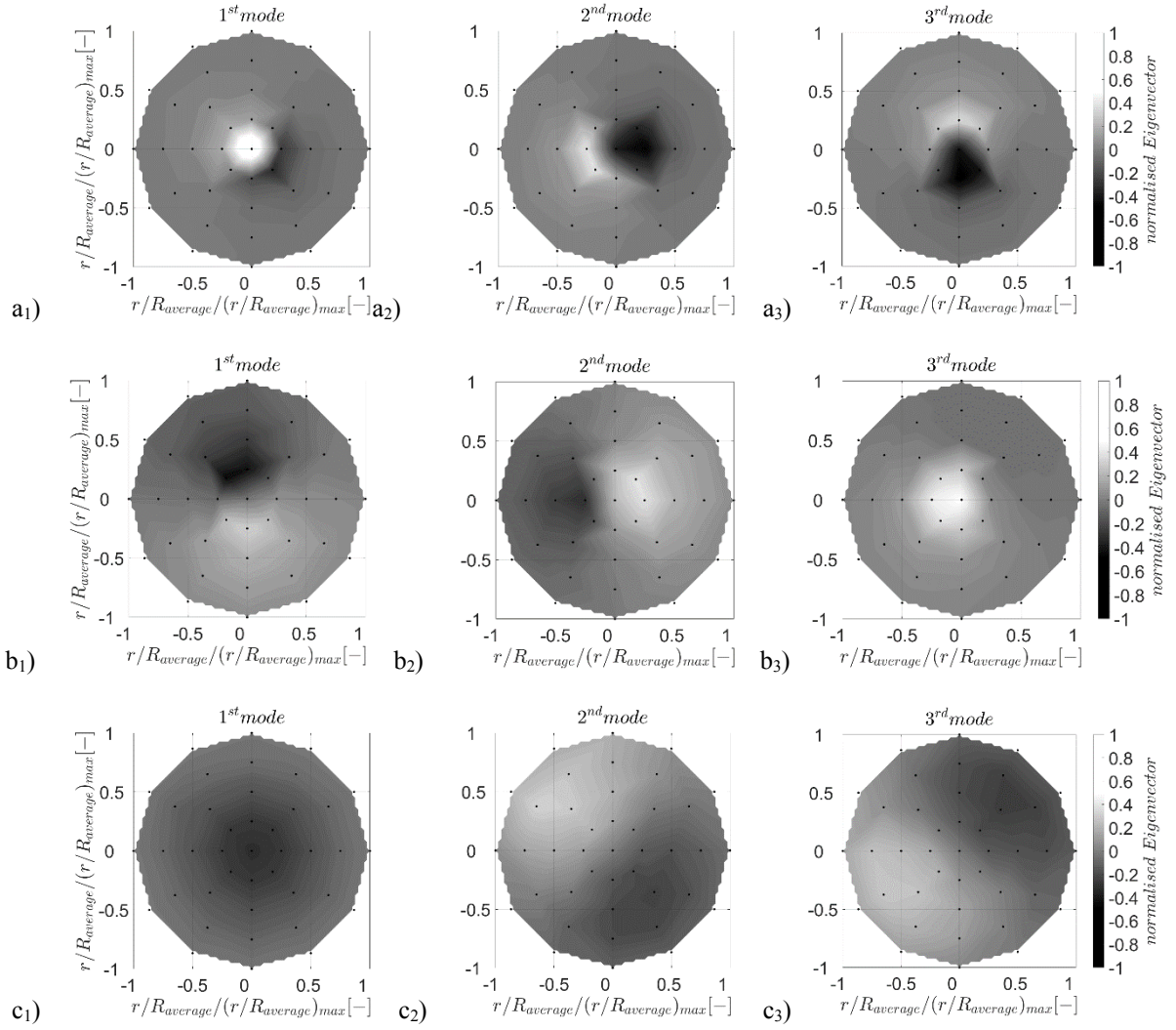
Figure 7.6: Normalised eigenvectors for the first ($_1$), second ($_2$) and third ($_3$) mode in *M1* for $S = 0.14$ (a), $S = 0.30$ (b) and $S = 0.69$ (c), respectively. To normalise the radial distance, maximum values of experimentally obtained $(r/R_{average})_{max}$ are used. For $S = 0.14$, $S = 0.30$ and $S = 0.69$ $(r/R_{average})_{max}$ = 1.82, 2.41 and 0.66, respectively.

In order to analyse, if any of the observed transient phenomena highlighted in figures 7.5 and 7.6 occur at a certain frequency in time, the power spectral density distribution of surface pressures measured at five radial distances $((r/R_{average}) / (r/R_{average})_{max} = 0, 0.25, 0.50, 0.75$ and 1$)$ for $S = 0.14$ (a_1), $S = 0.30$ (b_1) and $S = 0.69$ (c_1) in $S1$ (Figure 7.7) and $M1$ was analysed. In addition, the corresponding mode spectra of the lowest three modes are investigated for $S = 0.14$ (a_2), $S = 0.30$ (b_2) and $S = 0.69$ (c_2). To cut off frequencies, which show aliasing, a low-pass filter was applied to all calculated power spectral density functions at a frequency of 25Hz. For brevity, only results obtained in $S1$ are illustrated in what follows. Findings in $M1$ reveal a similar behaviour and therefore, would not contribute much to the general understanding.

The spectra of the first mode for $S = 0.14$ (Figure 7.7a_2) and $S = 0.69$ (Figure 7.7c_2) and the third mode for $S = 0.30$ (Figure 7.7b_2) show an energy distribution (over the frequencies analysed), which is similar to the surface pressure spectra obtained at the corresponding vortex centre $((r/R_{average}) / (r/R_{average})_{max} = 0$; Figure 7.7). This is not surprising, taking the findings of the POD analysis into account, as those are the modes affecting the surface pressure fluctuation at the vortex centre, which have been identified as a possible vortex intensifying / weakening (compare Figure 7.5).

The second and third mode of the lowest swirl ratio (Figure 7.7a_2) show relatively high energies at around 2-5Hz. A potentially similar pattern can be found in the surface pressure spectra for the corresponding vortex at radial distances between $(r/R_{average}) / (r/R_{average})_{max} = 0.25 - 0.75$ (Figure 7.7a_1). This might suggest that a combination of those modes can replicate (to some extent) the low frequency surface pressure fluctuations at those positions.

Figure 7.7b$_2$ shows that surface pressure fluctuations, which are causing a vortex intensifying / weakening around the vortex core (mode 3), occur at frequencies, which are relatively high (~20Hz) compared to those fluctuations, which are possibly causing a circular vortex movement around the vortex core (~3-4Hz, mode 1 and 2). The surface pressure spectra for $S = 0.30$ (Figure 7.7b$_1$) shows that the energy content of the dominant frequency of the third mode decreases with increasing radial distance and a possible connection between dominant frequencies of first and second mode (Figure 7.7b$_2$) and the corresponding surface pressure spectra for larger radial distances ($(r/R_{average}) / (r/R_{average})_{max} > 0.75$) can be inferred.

A relation between modes and the corresponding surface pressure spectra is not that obvious for the highest swirl ratio. It general, it is not surprising that mode spectra for the lowest swirl ratio show a better representation of the actual surface pressure spectra because for this swirl ratio the lowest three modes contain about 90% of the entire energy in the flow, whereas for $S = 0.30$ only about 50% of the entire energy is contained in mode 1 to 3, and only 60% for $S = 0.69$ (c.f. Figure 7.4a). Nevertheless, it seems likely that the circular vortex movement illustrated in Figure 7.5 causes those low frequency peaks in the surface pressure spectra. However, the surface pressure fluctuations of all vortices analysed seem to be far more complex and cannot be described fully by the lowest three modes.
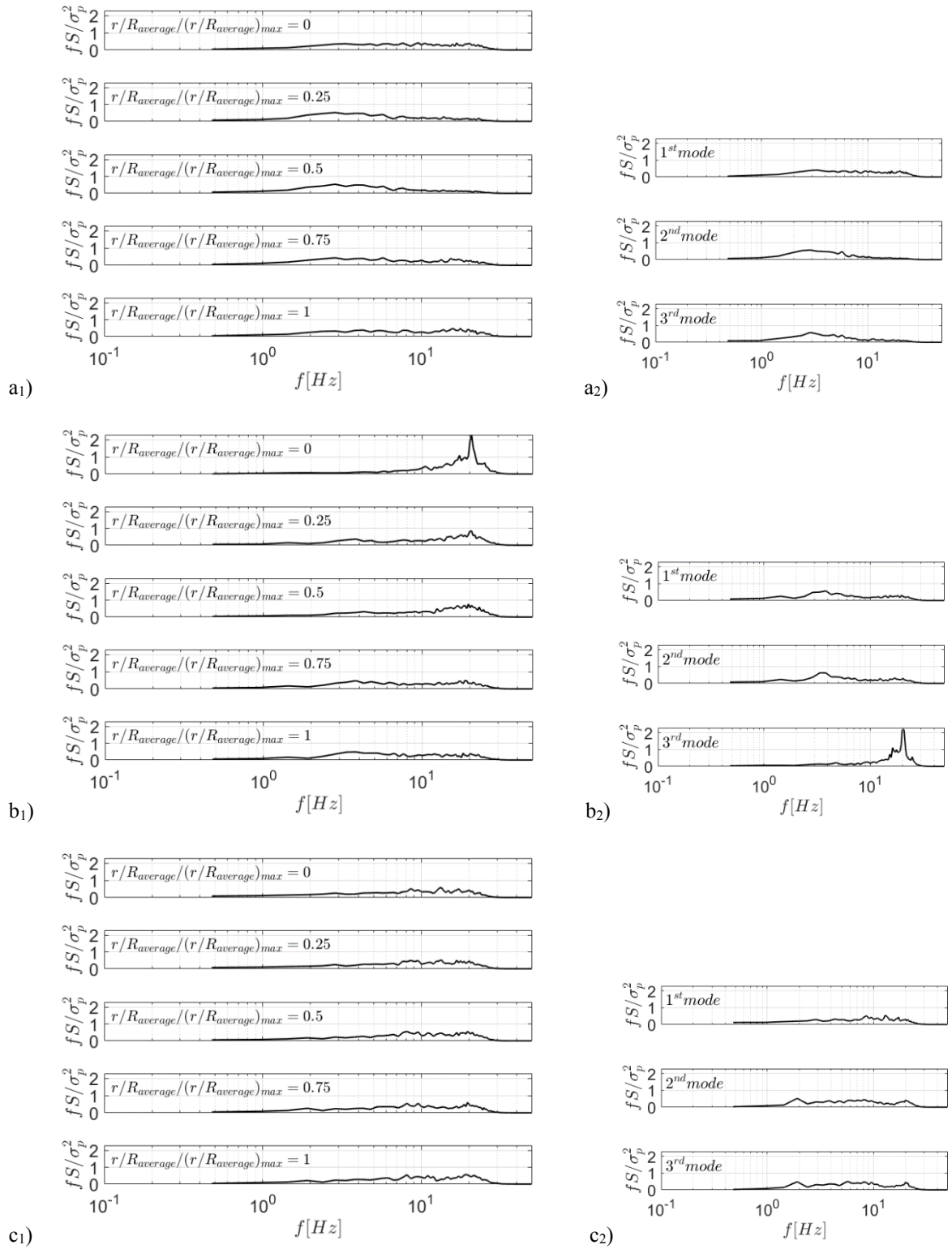
Figure 7.7: Power spectral density functions of surface pressure measurements at $(r/R_{average}) / (r/R_{average})_{max} = 0$, 0.25, 0.50, 0.75 and 1) for $S = 0.14$ (a$_1$), $S = 0.30$ (b$_1$) and $S = 0.69$ (c$_1$) in SI, respectively. Additionally, the power spectral density function of the POD coefficients of the first three modes is shown in (a$_2$), (b$_2$) and (c$_2$) for $S = 0.14$, $S = 0.30$ and $S = 0.69$, respectively.

7.3. Concluding remarks

Based on this analysis the following tentative conclusions can be drawn:

- The flow and surface pressure field of the generated vortices appears to be highly complex and unstable.

- The experiments have illustrated that significant vortex wandering can occur in physical tornado-like simulators despite of their boundary conditions remaining unchanged.

- The duration for which the vortex centre is moving throughout the measurement duration was found to increases with increasing swirl ratio.

- Vortex wandering velocities were found to differ in different simulators with respect to the corresponding circumferential velocity maximum. Furthermore, it was observed that vortex wandering velocities seem to be swirl ratio dependent and an increasing variability of vortex wandering velocities was observed with increasing swirl ratio.

- The first three modes of the surface pressure *POD* analysis seem to be related to a local intensifying / weakening of the vortex centre in time and a circular vortex movement around it. However, the surface pressure fluctuations for the three vortices analysed seem to be far more complex and cannot fully be described by the lowest three modes.

- Flow phenomena related to a local intensifying / weakening of the vortex were found to have a larger effect on vortices simulated with a low swirl ratio. This finding in combination with

the movement of a vortex with relatively large radial surface pressure gradients seems to be responsible for the relatively large uncertainties of surface pressures, which were observed at the centre of the simulator and have been reported and described in section 4.4.

8. *REFLECTIONS AND RECOMMENDATIONS FOR FURTHER WORK*

The focus of this work was set on analytical and experimental modelling of tornado-like vortices. A detailed evaluation of assumptions and limitations of experimental and analytical tornado-like vortex models (as outlined in the aim of this thesis) has shown that results obtained from both modelling techniques can only illustrate extremely simplified versions of atmospheric tornadoes (section 2).

The comparison of experimental and analytical model results (as outlined in objective 1) has highlighted that analytical models fail to replicate the complexity of the experimentally obtained time-averaged three-dimensional vortex structure due to the simplifying assumptions made in their derivations. A further benefit of experimental measurements compared to analytical results was found to be the ability to capture time-dependent flow characteristics of generated vortices, as those transient effects were found to cause instantaneous surface pressure changes of significant magnitude. It seems likely that those transient events have a large impact on the structural failure of buildings exposed to those types of flow fields. This underlines the importance of those processes to be taken into account when simulating tornado-like vortices, and since none of the analysed analytical vortex models takes turbulence or transient processes

into account, their application with respect to a realistic assessment of flow and pressure fields of naturally occurring tornadoes is questionable. Nevertheless, they remain the cheapest option to simulate the tornado flow field, which in the future might become profitable if they would allow a more realistic representation of atmospheric tornadoes. Relevant information can be found in section 2.4, section 5 and section 7.

With respect to the effect of the simulator's geometric design on experimentally obtained results (as outlined in objective 2), this work has proven that to date not all relevant geometric parameters of physical tornado simulators that affect the generated flow field are identified. As a result, the parity of currently used non-dimensional parameters (i.e., the aspect ratio and the swirl ratio) was found to be insufficient to guarantee the geometric and dynamic similarity of flow fields obtained in different tornado simulators. This means that results obtained in different simulators differ because they depend significantly on the geometric design and controlling boundary conditions of the corresponding simulator. This crucial limitation of experimental results is not surprising but has not been acknowledged before. This work suggests that there are geometric parameters that affect the flow field more significantly than others and that the effect of those parameters is not solely dependent on the rate of change, but also on the swirl ratio. This complex relationship between the swirl ratio and the effect of geometric parameters on the generated flow field, makes a generalised assessment of the effect of those parameters challenging, especially because it seems likely that their effect differs for different simulators due to their different geometric design and way of introducing vorticity to the flow field. Relevant information can be found in section 2.5, 3.2, 6 and appendix A.

Even though the swirl ratio is known to affect the generated vortex flow structure, this work demonstrates that swirl ratio definitions among different simulators differ, which complicates a reasonable comparison between flow fields generated in different simulators even further. Those findings are outlined in section 3.2.3 and appendix B. In addition, if the swirl ratio is determined based on velocity measurements, it seems sensible to introduce an uncertainty to its value in order to indicate the sensitivity of the swirl ratio to flow field changes. To date the swirl ratio is defined solely based on the circumferential velocity component. A potential reason for this could be that the circumferential velocity component has the largest velocity magnitude and therefore, might have received the most attention. Furthermore, due to its larger magnitude, measurement uncertainties do not account that significantly as for radial and vertical velocity components, whose magnitudes can be close to zero. Nevertheless, if the similarity of the three-dimensional flow structure is of interest it seems reasonable that non-dimensional parameters are introduced that describe the three-dimensional flow structure. Last but not least, since this work has proven that results obtained in physical tornado-like vortex simulators are affected by multiple geometric parameters, there is no solid reason why the swirl ratio should be dependent on the aspect ratio (as it is for most simulations conducted to date).

This work also addresses challenges associated with the geometric scaling factor. Determining the geometric scale of experimental simulations is a crucial part of a reasonable comparison between flow fields of different scale. However, this work has illustrated that the experimental measurement uncertainty can introduce an uncertainty to the geometric scaling factor, which consequently affects the accuracy of scaled results. Furthermore, it is noted that to date no uniform method exists to determine the geometric scale of physical tornado-like vortex simulations. This work shows that dependent on the chosen method, significant differences can

be found for the geometric scaling factor. Besides, it seems likely that the uncertainty of the scaling factor gets even larger when corresponding values have to be found in atmospheric tornadoes, because firstly, those values might change throughout the lifetime of a full-scale tornado, and secondly, the spatial resolution and associated uncertainty of full-scale measurements might make it difficult to determine required parameters with the desired representativeness. Furthermore, it is noted that for Wind Engineers, the lowest few metres of the simulated tornado-like flow field are of most interest as this is the part of the flow field, we and our built environment are exposed to. However, especially locations close to the surface are challenging to measure experimentally if the geometric scale of modelled tornado-like vortices is relatively small. This is also the most challenging region with respect to full-scale measurements because of the limitations associated with Doppler radar devices. For that reason, the question, how well the near-surface tornado flow field can be replicated remains unsolved to date. Those important limitation of scaled experimentally obtained results have not been acknowledged before and should be addressed in detail before results obtained from simplified models are applied with confidence in practice. Relevant information can be found in section 3.2.4 and appendix C.

One of the currently largest challenges for the Wind Engineering community with respect to the simulation of tornadoes, is to establish experimental tornado-like vortex modelling as a sensible methodology to assess the flow and pressure field of tornadoes. Currently, results obtained from experimental models seem to have the potential to capture some of the flow and pressure characteristics present in full-scale tornadoes; however, this work has shown that to date many uncertainties and unknowns still exist, which have to be addressed before trustworthy results can be obtained from those models.

Based on the findings presented in this thesis, the following further investigations are suggested:

A comparison study conducted in a number of the currently used tornado-like vortex simulators, for which the flow field of a specific full-scale tornado is generated in all simulators. Based on findings presented in section 3.2, section 6 and appendix A, it is assumed that apart from different geometric scales, different sets of geometric and dynamic parameters will be required for each simulator in order to obtain a flow field similar to the atmospheric one. At first, a comparison and detailed assessment of the differences of geometric and dynamic parameters would allow an improved understanding of the simulation of tornado-like vortices in different simulators. In addition, the experimentally obtained datasets could be used for a comparison study in which all experimentally simulated tornado-like vortices that are supposed to be similar to the same full-scale tornado flow field are compared. This would allow an understanding of how similar results obtained in different simulators can be expected to be if the simulation of the same full-scale tornado is of interest. As this work has proven that the effect of geometric parameters is swirl ratio dependent (section 6), it would be interesting to conduct this comparison for a number of different full-scale tornadoes of different intensity and core radius.

Further to this, an investigation concerning the sensitivity of wind loads on the uncertainty associated with the determination of the geometric scale is suggested. Also for this analysis, the flow field of an atmospheric tornado has to be simulated and the geometric scale of the simulation and its accompanied uncertainty has to be defined. The geometric scale including its uncertainty envelope can be used to scale two model structures, i.e., one model has to be scaled with the determined geometric scaling factor + ½ the uncertainty, and another model has to be scales with the geometric scaling factor − ½ the uncertainty. Differences of the wind load

analysis conducted with both model structures would give an improved understanding of how accurately wind loads can be assessed in a tornado-like vortex simulator. Also for this analysis it would be beneficial to analyse multiple full-scale tornadoes of different core radii to conduct this analysis for a variety of geometric scaling factors. In addition, if a similar comparison would be carried out in multiple simulators, this would allow conclusions to be drawn regarding the trustworthiness / representativeness of wind load results obtained in a specific simulator.

APPENDICES

A – The effect of the number of guide vanes on the generated vortex

In order to address if the number of guide vanes has an effect on the generated vortex, a brief experiment has been conducted in the small-scale tornado-like vortex simulator, *S1*. A detailed description of this simulator is provided in section 4.1. The original design of *S1* consists of 20 guide vanes, each of which has a height of 0.30m, a length of 0.13m and a width of 0.01m. All guide vanes are equally spaced around the circumference of the convergence chamber. For this test, the surface pressure profile across the simulator was measured for a guide vane angle of 70 degree ($S = 0.69$), see section 4.3.1 for detailed information regarding the surface pressure measurements.

Figure A.1 illustrates surface pressure distributions of vortices simulated with 10 and 20 guide vanes. This figure highlights that the radial distribution of surface pressures appears to be highly dependent on the number of guide vanes. In addition, the minimum pressure deficit (p_{min}) is also affected, i.e., a decrease of more than 50% (-149.8Nm^{-2} to -60.4Nm^{-2}) can be observed. Furthermore, figure A.1 suggests that not only the intensity of the vortex decreases with decreasing guide vanes, in addition, the radial extent of the vortex decreases. These

observations are in contrast to the work of *Davies-Jones (1973)*, which implicitly suggested that the number of vanes were not important in order to ensure geometric (Eq. 2.20) and dynamic similarity (Eq. 2.21 and 2.22).
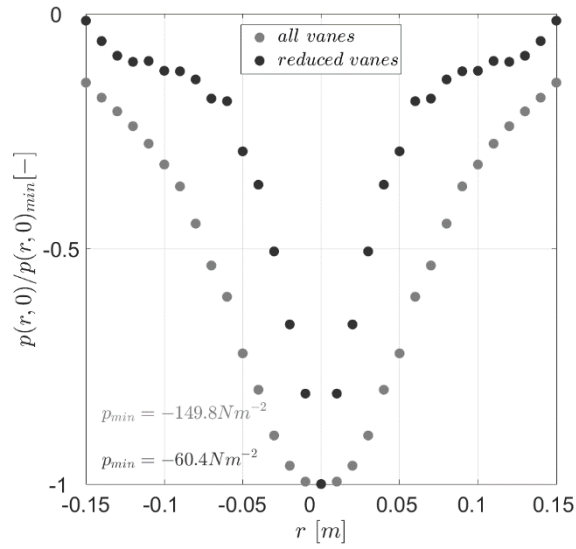
Figure A.1: Surface pressure distributions obtained in *S1* with *S* = 0.69 for all vanes (20 vanes) and a reduced number of vanes (10 vanes).

B - The swirl ratio and its multiple definitions

In this thesis, the swirl ratio has been defined in equation (4.2) and for the purpose of this appendix is denoted as S_1. As highlighted in section 3.2.3, a variety of other swirl ratio definitions exists (Table 3.3). In this section, swirl ratios are calculated for the flow fields obtained in the medium-scale (*M1*) and small-scale simulator (*S1*) of the University of Birmingham (*UoB*) for $S_1 = 0.30$ and $S_1 = 0.69$ at all measurement locations in the flow fields, using the following equation (B.1). Detailed information regarding the simulations conducted in *M1* and *S1* can be found in section 4.

$$S(r,z) = \frac{\Gamma(r,z)\, r}{2\, Q} \tag{B.1}$$

Figure B.1 illustrates the values of S (Eq. B.1) in *M1* (a) and *S1* (b) for the flow fields obtained with $S_1 = 0.30$ (a$_1$/b$_1$) and $S_1 = 0.69$ (a$_2$/b$_2$). The cross in the figures indicates the location where the overall largest circumferential velocity occurs, hence, the core radius, *R,* of the corresponding vortex. The solid vertical line, shows the location of the updraft radius ($\frac{1}{2}D_3 = R_3$). Radial and vertical distances are normalised in a similar way than figure 6.1 for *S1* and figure 6.5 for *M1*.

In addition, swirl ratios have been calculated using the following equations:

$$S_2 = \frac{\Gamma_{(R)}\, R}{2Q} \tag{B.2}$$

$$S_3 = \frac{\Gamma_{average\ @\ R_3} R_3}{2Q} \qquad \text{(B.3)}$$

$$\text{with} \quad \Gamma_{\text{average}\ @\ R_3} = \frac{1}{N}\sum_{i=1}^{N} \Gamma(R_{3_i})$$

where, N is the number of measurement heights in the corresponding simulator.

The definition adopted for S_1 (Eq. 4.2) is identical to the definition used at the Purdue University (*Church et al., 1977*) and the definition adopted for S_2 (Eq. B.2) is similar to the definition adopted in WIST (*Haan et al., 2017*). Equation (B.3) is based on a height average of swirl ratios at $r = R_3$. This definition is identical to the swirl ratio defined in VorTECH (*Tang et al., 2018*). Furthermore, the following definition is introduced (Eq. B.4) as this is the definition used in WindEEE (*Refan and Hangan, 2018*).

$$S_4 = \frac{\Gamma_{(R)} R_3}{2Q} \qquad \text{(B.4)}$$

The difference between the definition of S_4 (Eq. B.4) and S_2 and S_3 (Eq. B.2 and B.3) is that the length scale in the numerator of S_4 is not identical to the radial distance at which the circulation is estimated, instead the radius of the updraft hole, R_3, is used in equation (B.4).

Corresponding swirl ratio values ($S_1 - S_4$) are presented in table B.1 for the flow fields obtained in *M1* and *S1* for $S_1 = 0.30$ and $S_1 = 0.69$. In addition, the flow rate and corresponding radial distances of R and R_3 are given.
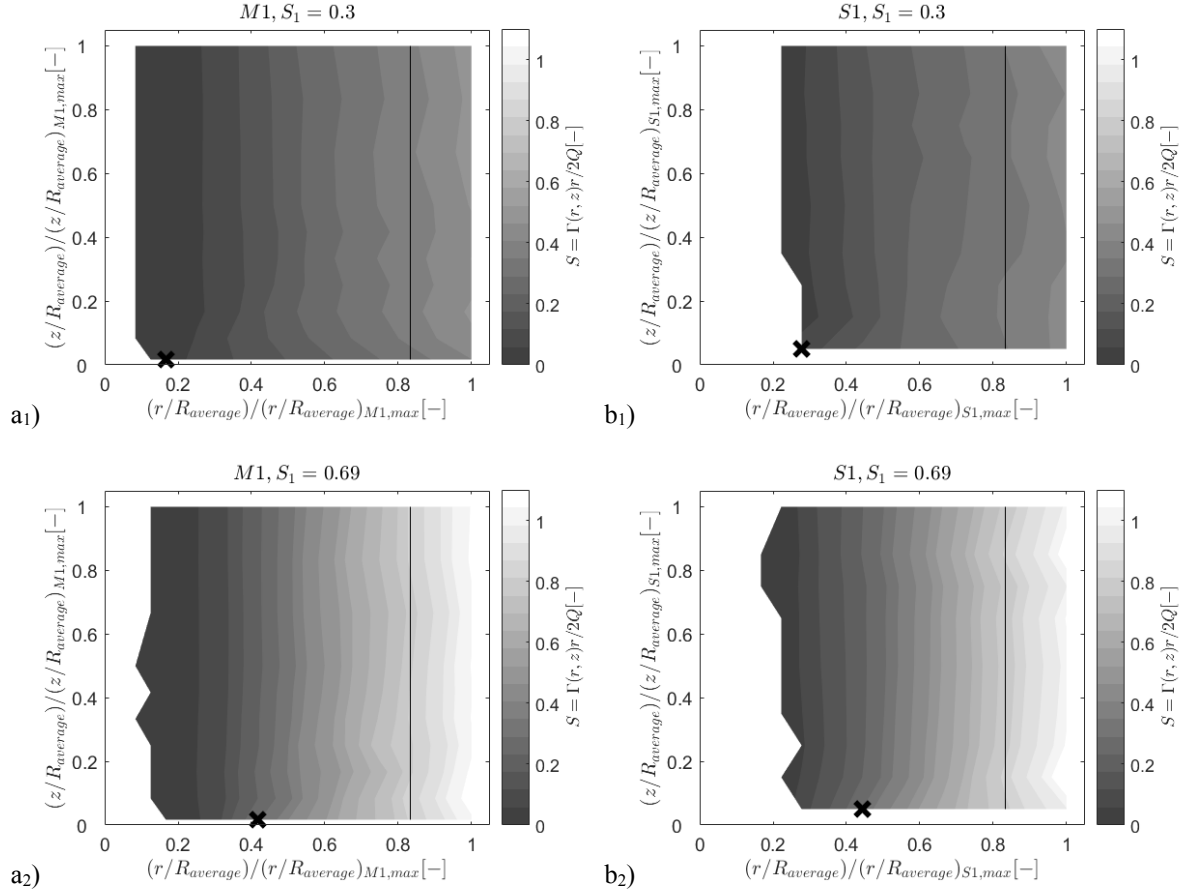
Figure B.1: Swirl ratios, S (Eq. B.1), in the medium-scale (a) and small-scale (b) simulator for $S_1 = 0.30$ (1) and $S_1 = 0.69$ (2). The cross indicates the location of the core radius, R, where the overall largest circumferential velocity occurs, whereas the solid vertical line is placed at the updraft radius ($\frac{1}{2}D_3 = R_3$). Radial and vertical distances are normalised in a similar way to figure 6.1 for $S1$ and figure 6.5 for $M1$.

Table B.1: Swirl ratios ($S_1 - S_4$) defined at different locations in $M1$ and $S1$. Additionally, corresponding flow rates and radial distances of R and R_3 are presented.

a)

	Figure B.1	S_1	S_2	S_3	S_4	$Q\ [m^3s^{-1}]$	$R\ [m]$	$R_3\ [m]$
M1	a1)	*0.30*	*0.04*	*0.38*	*0.20*	*7.58*	*0.100*	*0.500*
S1	b1)	*0.30*	*0.09*	*0.35*	*0.26*	*0.65*	*0.050*	*0.150*

b)

	Figure B.1	S_1	S_2	S_3	S_4	$Q\ [m^3s^{-1}]$	$R\ [m]$	$R_3\ [m]$
M1	a2)	*0.69*	*0.29*	*0.82*	*0.59*	*6.86*	*0.250*	*0.500*
S1	b2)	*0.69*	*0.31*	*0.81*	*0.59*	*0.55*	*0.080*	*0.150*

Because of the forced aspect ratio and guide vane angle parity between both simulators, S_1 is identical for flow fields illustrated in figure B.1a$_1$ and figure B.1b$_1$ (Table B.1a) and figure B.1a$_2$ and figure B.1b$_2$ (Table B.1b), respectively. It is noted that the definition of S_1 is the only swirl ratio definition of those presented in this section, which is independent of the radial distance and any direct velocity measurement.

Figure B.1 illustrates an increase in S with increasing radial distance for both flow fields in both simulators. The reason for this can be found in the numerator of equation (B.1). Since the circulation is proportional to the radial distance, S (Eq. B.1) is proportional to the square of the radial distance. This relation between S and r is also reflected in the definitions of S_2 and S_3, which correspond to the lowest (S_2) and highest swirl ratio (S_3) of all analysed flow fields because S_2 is calculated at relatively small radial distances ($r = R$) and S_3 is calculated at relatively large radial distances ($r = R_3$) (Table B.1). Because of the dependence on the radial distance, swirl ratios obtained at different radial distances in the flow fields of $M1$ and $S1$ for $S_1 = 0.30$ differ by a factor of ~ 9.5 and ~ 3.9, respectively (Table B.1a). For vortices simulated with $S_1 = 0.69$ in $M1$ and $S1$, swirl ratios obtained at different radial distances differ by a factor of ~ 2.7 in both simulators (Table B.1b).

The swirl ratio S_4 is defined based on a combination of R and R_3 (Eq. B.4) and therefore, its value lies between the values obtained for S_2 and S_3 (Table B.1).

Differences of up to 50% are revealed between values of S_2 in $M1$ and $S1$ for the flow fields simulated with $S_1 = 0.30$ (Table B.1a). This relatively large difference seems to be caused by the relatively small core radius, R, of the vortex in $M1$ compared to the size of the simulator

(Figure B.1a$_1$). As a result, the value obtained for S_2 in $M1$ is relatively small compared to the value obtained for S_2 in $S1$. Differences between swirl ratios defined in a similar way in $M1$ and $S1$ for $S_1 = 0.69$ were found to be less than 7%, regardless of the definition used (Table B.1b).

To conclude, this section has demonstrated that the swirl ratio value can depend significantly on where in the flow field it is defined. Furthermore, results presented in table B.1a seem to suggest that swirl ratio parity between flow fields may exist at certain locations; however, those locations may not be representative for the entire flow field of those vortices. Additionally, it is noted that swirl ratios presented here are calculated based on time-averaged quantities of the circulation and the flow rate and therefore, conclusions can only be drawn with respect to the time-averaged flow behaviour. The instantaneous flow field of two vortices of similar swirl ratio may differ significantly. Furthermore, all swirl ratio definitions presented in this section focus on the similarity between circumferential velocity components. Therefore, no conclusion can be drawn regarding the similarity of radial and vertical velocity components.

C – Geometric scaling of simulated vortices

In order to determine the geometric scale of simulations conducted in *M1* and *S1* for three different swirl ratios ($S = 0.14$, $S = 0.30$ and $S = 0.69$), the flow field around the corresponding core radius close to the simulators' surfaces was mapped in detail and the radial distance, *R*, and height, *Z*, at which the overall maximum circumferential velocity component occurs was determined. Detailed information regarding the simulations conducted in the medium-scale simulator, *M1* and the small-scale simulator, *S1*, can be found in section 4. For the purpose of this appendix, the spatial distribution of velocity measurements close to the simulators' surfaces around the corresponding core radius of simulated vortices was refined, and measurements have been taken every 0.005m in *M1* and *S1* in the radial direction and at seven heights (0.001m, 0.003m, 0.006m, 0.008m, 0.012m, 0.016m and 0.020m) in *M1* and at five heights (0.001m, 0.003m, 0.006m, 0.008m, 0.012m) in *S1*. Figure C.1 illustrates maximum circumferential velocities at those measurements heights in *M1* (a_1) and *S1* (b_1). Corresponding core radii in *M1* and *S1* are shown in Figure C.1a_2 and Figure C.1b_2. Table C.1 provides values of *R* and *Z* based on the geometric scaling method introduced by *Hangan and Kim (2008)* for $S = 0.14$, $S = 0.30$ and $S = 0.69$ in both simulators.
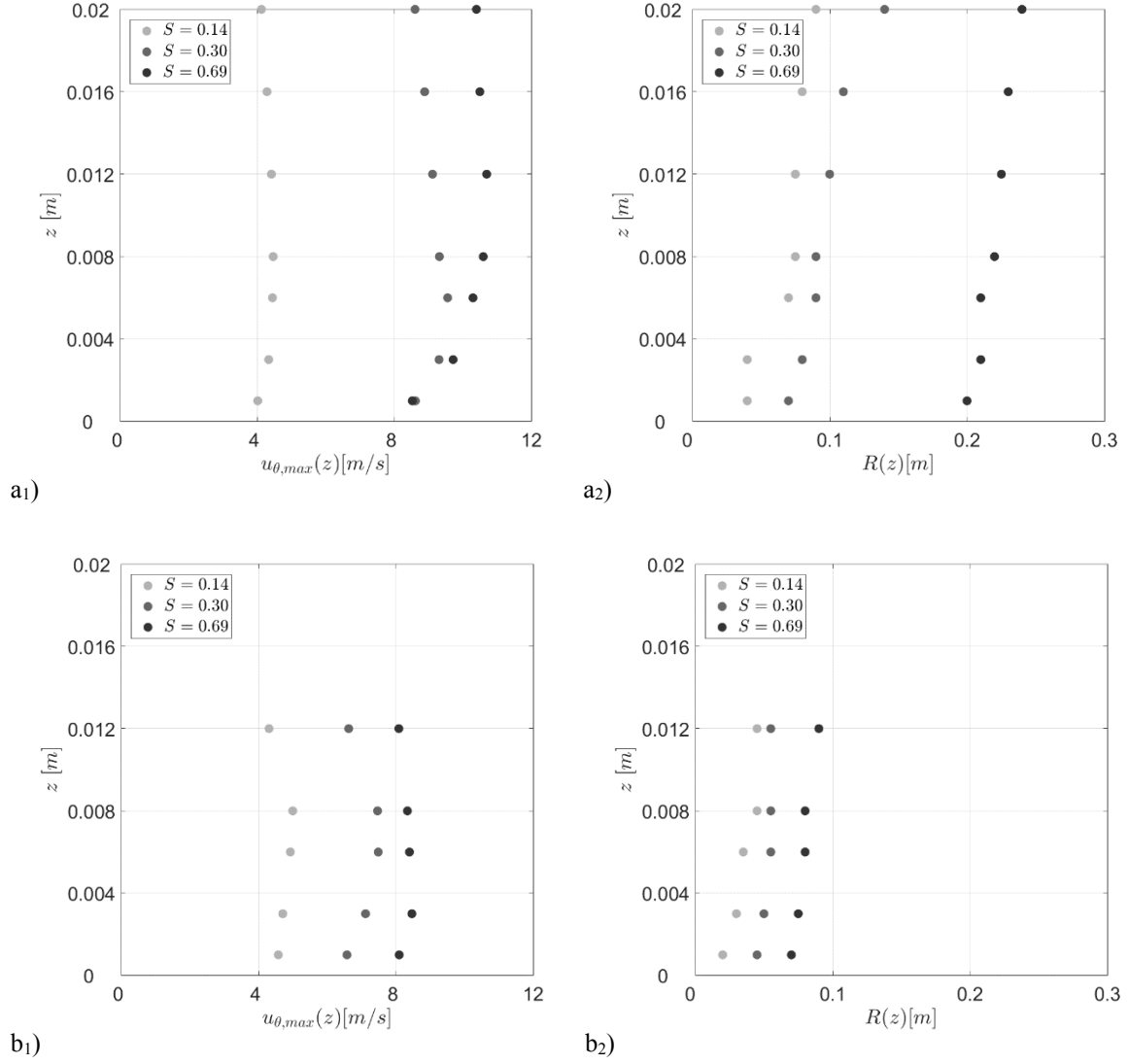
Figure C.1: Maximum circumferential velocities at different heights in *M1* (a_1) and *S1* (b_1) for $S = 0.14$, $S = 0.30$ and $S = 0.69$ and corresponding core radii in *M1* (a_2) and *S1* (b_2).

Table C.1: Values of R (a) and Z (b), defined at the radial distance and height at which the overall circumferential velocity maximum occurs for vortices simulated in *M1* and *S1* for $S = 0$ 14, $S = 0.30$ and $S = 0.69$.

a)

	$S = 0.14$	$S = 0.30$	$S = 0.69$
$R(M1)$	0.075m	0.090m	0.225m
$R(S1)$	0.045m	0.055m	0.075m

b)

	$S = 0.14$	$S = 0.30$	$S = 0.69$
$Z(M1)$	0.008m	0.006m	0.012m
$Z(S1)$	0.008m	0.006m	0.003m

In keeping with previous work, R increases with increasing swirl ratio from 0.075m to 0.225m in $M1$ and from 0.045m to 0.075m in $S1$ (Table C.1a). The height at which the overall maximum circumferential velocity occurs seems to lower from 0.008m to 0.003m with increasing swirl ratio in $S1$ (Table C.1b). A similar trend is observed in $M1$ for $S = 0.14$ and $S = 0.30$; however, for the largest swirl ratio in $M1$, the height at which $u_{\theta,max}$ occurs increases to 0.012m. Figure C.2a illustrates the scaling factors found between R and Z of $M1$, and R and Z of $S1$ for the three swirl ratios. Obviously, for one flow field only one scaling factor can exist. However, figure C.2a illustrates that scaling factors between R and Z of $M1$, and R and Z of $S1$ do not match for the same swirl ratio. It needs to be noted that an uncertainty is introduced to the values of R and Z due to the measurement uncertainty of velocity measurements, which is addressed in section 4.4. If this measurement uncertainty is taken into account, no definite value of R and Z can be defined because Z has an uncertainty of $\sim \mp 0.005$m and $\sim \mp 0.003$m in $M1$ and $S1$, respectively, and due to the uncertainty in determining Z, an uncertainty is introduced to R. The uncertainty for R is approximately ∓ 0.010m and about ∓ 0.005m in $M1$ and $S1$, respectively. Figure C.2b illustrates the same scaling factors as shown in Figure C.2a - in addition, the corresponding uncertainty of R and Z is shown. As a result, a scaling factor of approximately 1.5 ∓ 0.1 can be determined in order to scale R and Z of vortices simulated in $S1$ to values of R and Z of vortices simulated in $M1$ for $S = 0.14$ and $S = 0.30$. For the largest swirl ratio ($S = 0.69$), a scaling factor of $\sim 3 \mp 0.4$ is found to scale values of R and Z in $S1$ to values obtained for R and Z in $M1$. It is noted that the uncertainty in determining scaling factors is a limiting factor for the accuracy of, e.g., wind load analyses, because the size of modelled building structures is directly affect by the chosen scaling factor. It also needs to be noted that obtained scaling factors do not guarantee that the flow fields show similar flow characteristics (as will be demonstrated in section 6.3.1). This method simply scales results obtained in two different simulators of different scale based

on values obtained for *R* and *Z*. In addition, results shown in figure C.2b highlight that the geometric scaling factor of vortices generated in different simulators dependents on the swirl ratio. Therefore, no consistent scaling value can be defined that scales vortices simulated in one simulator to vortices simulated in another simulator, this was found to be the case even if swirl ratio and aspect ratio of the simulated vortices are similar. When a comparison to full-scale tornadoes is of interest, the uncertainty of scaling factors is likely to increase even further due to the relatively large measurement uncertainty of mobile Doppler radar measurements and the transient nature of atmospheric tornadoes. Therefore, it is extremely important to be aware of uncertainties associated with the geometric scaling factor because obtained results are directly affected.
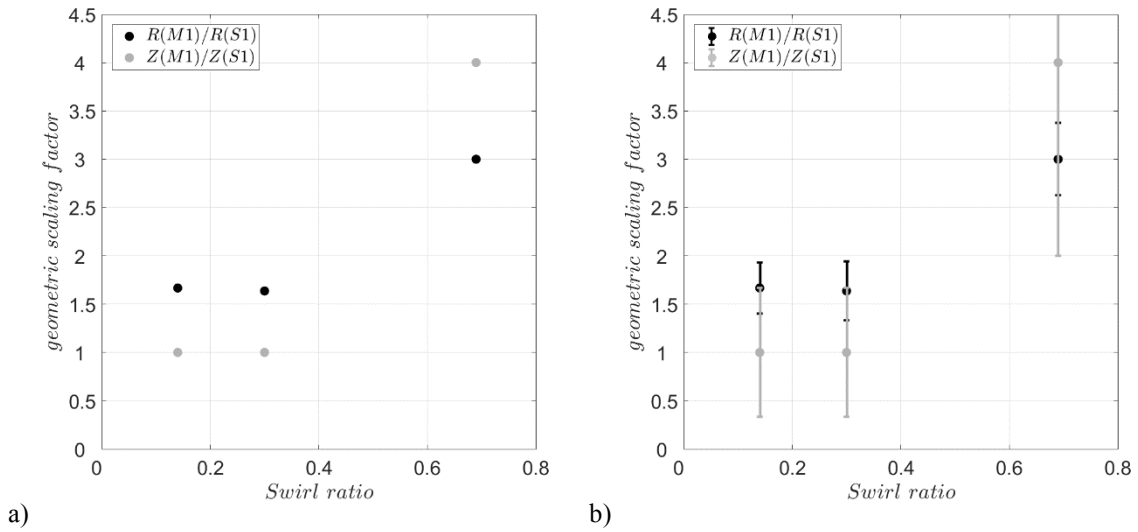
Figure C.2: Geometric scaling factors for *R* and *Z* of *M1* and *S1* for *S* = 0.14, *S* = 0.30 and *S* = 0.69 without taken the measurement uncertainty of velocity measurements into account (a) and with taken the measurement uncertainty of velocity measurements into account (b).

For cases where no flow field information is available but a geometric scaling factor needs to be found, the surface pressure distribution has been used to determine the vortex core radius by means of assuming the validity of the cyclostrophic equation (Eq. 2.5) (e.g., *Mishra et al., 2008a*). More details regarding the determination of $R_{cyclostrophic}$ are provided in section 4.2.

Table C.2 illustrates values of $R_{cyclostrophic}$ obtained for $S = 0.14$, $S = 0.30$ and $S = 0.69$ in *M1* and *S1*. It needs to be noted that an uncertainty is introduced due to the spatial distribution of surface pressure measurements. The information embedded in table C.2 reveals that scaling factors of vortices simulated in *S1* and *M1* are approximately around 15 , 5 and 3.2 for $S = 0.14$, $S = 0.30$ and $S = 0.69$, respectively. For the two lower swirl ratios, the scaling factors obtained by means of $R_{cyclostrophic}$ differ significantly compared to the scaling factors obtained by means of the approach presented in table C.1. The results obtained in this section highlight the dependence of the scaling factor on the chosen determination method, and the large uncertainty associated with it. Since this uncertainty has a direct effect on scaled results, it is crucial that the limitations associated with the geometric scaling are addressed thoroughly before results from scaled simulators are applied in practice.

Table C.2: Values of $R_{cyclostrophic}$, defined at the radial distance from the vortex centre at which the maximum pressure gradient in the radial direction occurs for vortices simulated in *M1* and *S1* for $S = 0.14$, $S = 0.30$ and $S = 0.69$.

	$S = 0.14$	$S = 0.30$	$S = 0.69$
$R_{cyclostrophic}(M1)$	$0.075m \mp 0.025m$	$0.075m \mp 0.025m$	$0.175m \mp 0.025m$
$R_{cyclostrophic}(S1)$	$0.005m \mp 0.004m$	$0.015m \mp 0.005m$	$0.055m \mp 0.005m$

D - The tubing transfer function

The length of the tube, which connects the pressure tap to the pressure transducer can have an effect on the measured fluctuating pressures due to distortion effects (*Irwin et al., 1979*). Those distortion effects are known to increase with increasing tubing length. The experimental arrangement that was used to quantify distortion effects of the tubing system used for this work is shown in figure D.1. A sound wave is propagated by a loudspeaker and the signal is recorded at the reference transducer and the measurement transducer with 100Hz, which equals the measurement frequency used for this work. The reference transducer measures an undistorted signal of the sound wave directly at the small cavity above the loudspeaker, whereas the measurement transducer measures the distorted signal of the sound wave after it has propagated through the tube of interest.
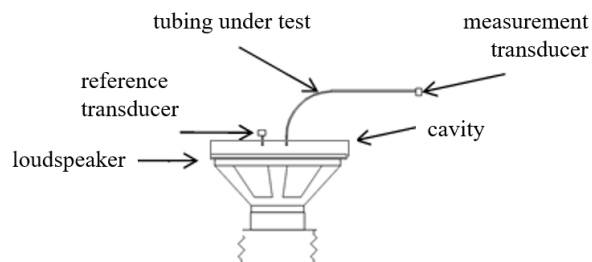
Figure D.1: Experimental arrangement to measure the tubing transfer function.

By means of the Tubing Transfer Function (*TTF*), the distorted pressure signal can be corrected. In order to obtain the *TTF*, the pressure signals measured at both transducers need to be transferred from the time domain into the frequency domain by means of a Fast Fourier Transformation. The *TTF* can then be calculated using the following formula (Eq. D.1) (*Irwin et al., 1979*):

$$TTF = \frac{B_i}{A_i} \qquad \text{(D.1)}$$

where, B_i and A_i are the complex Fourier coefficients of the pressure signal measured at the measurement transducer and the reference transducer, respectively.

The *TTF* for the 0.3m long *PVC* tube used for this work is shown in the figure D.2.
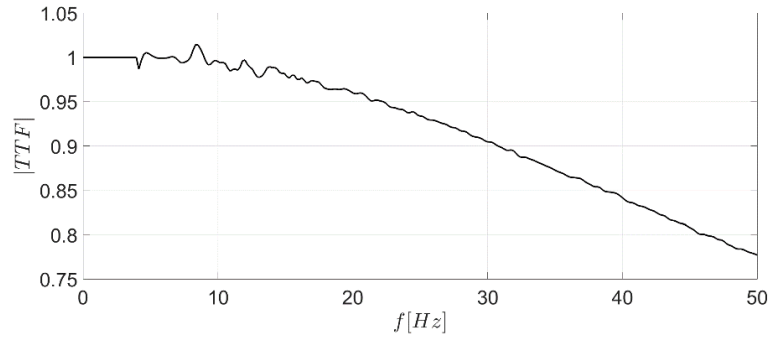
Figure D.2: Absolute values of the TTF.

By means of the *TTF*, every pressure signal measured for this work was corrected using equation (D.2):

$$p_{corrected} = IFFT\left(\frac{FFT(p)}{TTF}\right) \qquad \text{(D.2)}$$

where, *IFFT* is the Inverse Fast Fourier Transformation, $p_{corrected}$ and p are the corrected and distorted pressure signal, respectively.

Looking at figure D.2 in combination with equation (D.2), the decreasing *TTF* with increasing frequency means that the tube's effect on the pressure signal is larger for fluctuations with higher frequencies. This effect can also be seen when comparing distorted and corrected

pressure signals (Figure D.3). However, the change in mean values (Figure D.3) is not significant and much smaller compared to the experimental measurement uncertainty defined in section 4.4.

Since the majority of this work focuses on temporal averages of pressure measurements, those findings suggest that the measured (distorted) pressure signal will only be changed insignificantly when applying the distortion correction. A potential larger effect of the tubing length can be expected for the analysis regarding transient processes in tornado-like flows (section 7). Even though, it might seem unnecessary to apply the correction for temporally averaged quantities, the correction was undertaken for all measured pressure signals of this work.

Figure D.3: Difference between corrected and distorted pressure signal

REFERENCES

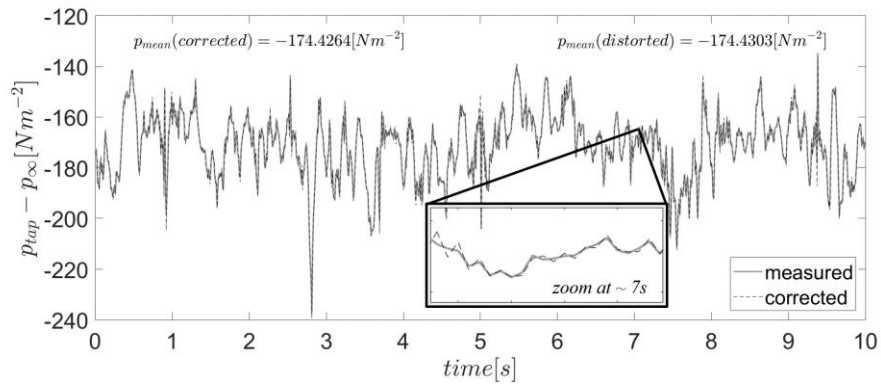Alekseenko, S.V., Kuibin, P.A., Okulov, V.L., 2007. *Theory of Concentrated Vortices. Springer Berlin Heidelberg New York. ISBN 978-3-540-73376-8*

Alexander, C.R. and Wurman, J., 2008. *Updated mobile radar climatology of supercell tornado structures and dynamics. The 24th Conference on Severe Local Storms. Savannah, GA. USA*

Antonescu, B., Schultz, D.M., Holzer, A., Groenemeijer, P., 2017. *Tornadoes in Europe: An underestimated threat. Bulletin of the American Meteorological Society 98, 713–729*

Baker, C.J., 2000. *Aspects of the use of proper orthogonal decomposition of surface pressure fields. Journal of Wind and Structures, 3, 97-115*

Baker, C.J. and Sterling, M., 2017. *Modelling wind fields and debris flight in tornadoes. Journal of Wind Engineering and Industrial Aerodynamics 168, 312-321*

Batterson, J.W., Maicke, B.A., Majdalani, J., 2007. *Advancements in Theoretical Models of Confined Vortex Flowfields. Defense Technical Information Center, University of Tennessee Space Institute, Tullahoma, TN 37388*

Bech, J., Gayà, M., Aran, M., Figuerola, F., Amaro, J., Arús, J., 2009. *Tornado damage analysis of a forest area using site survey observations, radar data and a simple analytical vortex model. Atmospheric Research 93, 118–130*

Bloor, M.I.G., Ingham, D.B., 1987. *The flow in industrial cyclones. Journal of Fluid Mechanics 178, 507-519*

Brown, R.A., Wood, V.T., 2004. *Comparisons of Doppler velocity tornadic vortex signatures with signatures from model vortices. The 22nd Conference on Severe Local Storms, Anonymous Hyannis, MA*

Burgers, J.M., 1948. *A Mathematical Model Illustrating the Theory of Turbulence. Advances in Applied Mechanics 1, 171-199*

Case, J., Sarkar, P., Sritharan, S., 2014. *Effect of low-rise building geometry on tornado-induced loads. Journal of Wind Engineering and Industrial Aerodynamics 133, 124-134*

Church, C.R., Snow, J.T., Agee, E.M., 1977. *Tornado Vortex Simulation at Purdue University. American Metrological Society* 58, 900–908

Church, C.R., Snow, J.T., Baker, G.L., Agee, E.M., 1979. *Characteristics of Tornado-Like Vortices as a Function of Swirl Ratio: A Laboratory Investigation. Journal of the Atmospheric Sciences* 36, 1755-1776

CSWR – Centre for Severe Weather Research. *Radar Observations of Tornadoes and Thunderstorms Experiments – ROTATE (last accessed 02/07/2018)*

Davies-Jones, R., 1973. *The Dependence of Core Radius on Swirl Ratio in a Tornado Simulator. Journal of Atmospheric Science* 30, 1427-1430

Davies-Jones, R. and Kessler, E., 1974. *Tornadoes. Weather and Climate Modification. Wiley,* 552-595

Davies-Jones, R., 1976. *Laboratory simulations of tornadoes. Proceedings of the Symposium on Tornadoes: Assessment of Knowledge and Implications of Man. Boston, MA, USA*

Davies-Jones, R., 1984. *Streamwise Vorticity: The Origin of Updraft Rotation in Supercell Storms. Journal of Atmospheric Science* 41, 2991-3006

Davies-Jones, R., Trapp, R.J., Bluestein, H.B., 2001. *Tornadoes and Tornadic Storms. Meteorological Monographs* 50, 167-221

Davies-Jones, R., 2006. *Tornadogenesis in Supercell Storms–What we know and what we don't know. Symposium on the Challenges of Severe Convective Storms. Atlanta, GA, USA*

Davies-Jones, R., 2015. *A review of supercell and tornado dynamics. Atmospheric Research* 158 – 159, 274–291

Dessens, J., 1971. *Influence of Ground Roughness on Tornadoes: A Laboratory Simulation. Journal of Applied Meteorology* 11, 72-75

Doering, C.R. and Gibbon, J.D., 1995. *Applied Analysis of the Navier-Stokes Equations, 1st edition. Cambridge University Press. ISBN: 978-0521445689*

Doswell, C.A., Burgess, D.W., 1993. *Tornadoes and Tornadic Storms: A Review of Conceptual Models. The Tornado: Its Structure, Dynamics Prediction, and Hazards. Geophysical Monograph Series* 79

Edwards, R. LaDue, J.G., Ferree, J.T., Scharfenberg, K., Maier, C., Coulbourne, W., 2013. *Tornado Intensity Estimation: Past, Present, and Future. American Meteorological Society* 641 – 653

Elsom, D.M., Meaden, G.T., Reynolds, D.H., Rowe, M.W., Webb, J.D.C., 2001. *Advances in tornado and storm research in the United Kingdom and Europe: the role of the Tornado and Storm Research Organisation. Atmospheric Research* 56, 19–29

Fujita, T.T., 1971. *Proposed characterization of tornadoes and hurricanes by area and intensity. University of Chicago. Research Paper 91*

Gibbings, J.C., 2011. *Dimensional Analysis. Springer Verlag. ISBN 978-1-84996-317-6*

Gillmeier, S., Sterling, M., Hemida, H., 2016. *An Analysis of the Influence of a Tornado Generator's Geometry on the Flow Field. The 8th International Colloquium on Bluff Body Aerodynamics and Applications. Boston, Massachusetts, USA*

Gillmeier S., Sterling, M., Baker,C., 2017. *An analysis of non-stationary processes in tornado-like vortices. International Workshop on Physical Modelling of Flow and Dispersion Phenomena. France*

Gillmeier, S., Sterling, M., Hemida, H., Baker, C.J., 2018. *A reflection on analytical tornado-like vortex flow field models. Journal of Wind Engineering and Industrial Aerodynamics 174, 10–27*

Haan, F.L., Sarkar, P.P., Gallus, W.A., 2008. *Design, construction and performance of a large tornado simulator for win engineering applications. Engineering Structures 30, 1146–1159*

Haan, F.L., Balaramudu, V.K., Sarkar, P.P., 2010. *Tornado-Induced Wind Loads on a Low-Rise Building. Journal of Structural Engineering 136, 106-116*

Haan, F.L., Sarkar, P.P., Kopp, G.A., Stedman, D.A., 2017. *Critical wind speeds for tornado-induced vehicle movements. Journal of Wind Engineering and Industrial Aerodynamics 168, 1–8*

Hangan, H. and Kim, J-D., 2008. *Swirl ratio effects on tornado vortices in relation to the Fujita scale. Wind and Structures, Vol. 11, No. 4, 291–302*

Hashemi Tari, P., Gurka, R., Hangan, H., 2010. *Experimental investigation of tornado-like vortex dynamics with swirl ratio: The mean and turbulent flow fields. Journal of Wind Engineering and Industrial Aerodynamics 98, 936-944*

Hoecker, W.H., 1960. *Wind speed and air flow patterns in the Dallas tornado of April 2, 1957. Monthly Weather Review 88, 167-180*

Hu, H., Yang, Z., Sarkar, P., 2011. *Characterization of the wind loads and flow fields around a gable-roof building model in tornado-like winds. Experiments in Fluids 51, 835-851*

Irwin, H.P.A.H., Cooper, K.R., Girard, R., 1979. *Correction of distortion effects caused by tubing systems in measurements of fluctuating pressures. Journal of Industrial Aerodynamics 5, 93-107*

Jeff Haby – *Thunderstorm Ingredients - theweatherprediction.com (last accessed 31/08/2018)*

Jischke, M.C. and Parang, M., 1974. *Properties of Simulated Tornado-Like Vortices. Journal of the Atmospheric Science 11, 506–512*

Karami, Romanic, D., Refan, M., Hangan, H., 2017. *Modeling of tornado-like vortices. Islands Fluid Mechanics Meeting*

Karstens, C.D., Samaras, T.M., Lee, B.D., Gallus Jr. W.A., Finley, C.A., 2010. *Near-Ground Pressure and Wind Measurements in Tornadoes. Monthly Weather Review 138, 2570–2588*

Kilty, K.T., 2005. *Steady-state tornado vortex models (last accessed 08/06/2017)*

Kim, Y.C., Matsui, M., 2017. *Analytical and empirical models of tornado vortices: A comparative study. Journal of Wind Engineering and Industrial Aerodynamics 171, 230-247*

Kosiba, K. A., Trapp, R.J., Wurman, J., 2008. *An analysis of the axisymmetric three dimensional low-level wind field in a tornado using mobile radar observations. Geophysical Research Letter, 35*

Kosiba, K., Wurman, J., 2010. *The Three-Dimensional Axisymmetric Wind Field Structure of the Spencer, South Dakota, 1998 Tornado. Journal of the Atmospheric Sciences 67, 3074-3083*

Kosiba, K. and Wurman, J., 2013. *The Three-Dimensional Structure and Evolution of a Tornado Boundary Layer. Weather and Forecasting 28, 1552–1561*

Kraus, H., 2004. *Die Atmosphäre der Erde: Eine Einführung in die Meteorologie. Springer Verlag, Auflage 3. ISBN-10:3540206566*

Kuo, H.L., 1971. *Axisymmetric Flows in the Boundary Layer of a Maintained Vortex. Journal of the Atmospheric Sciences 28, 20-41*

Lee, J.J., Samaras, T., Young, C.R., 2004. *Pressure measurements at the ground in an F-4 tornado. The 22nd Conference on Sever Local Storms. Anonymous Hyannis, MA, USA*

Lee, W.C and Wurman, J., 2005. *Diagnosed three-dimensional axisymmetric structure of the Mulhall tornado on 3 May 1999. Journal of Atmospheric Science 62, 2373–2393*

Leslie, F.W., 1977. *Surface Roughness Effects on Suction Vortex Formation: A Laboratory Simulation. Journal of Wind Engineering and Industrial Aerodynamics, 34, 1022-1027*

Letchford, C., Mans, C., Chay, M.T., 2002. *Thunderstorms - their importance in wind engineering (a case for the next generation wind tunnel). Journal of Wind Engineering and Industrial Aerodynamics 90, 1415–1433*

Lewellen, W.S. 1976. *Theoretical models of the tornado vortex. Symposium on Tornadoes: Assessment of Knowledge and Implications for Man, Texas Tech University, 107–143*

Lewellen, W.S., 1993. *Tornado Vortex Theory. The Tornado: Its Structure, Dynamics, Prediction, and Hazards. Geophysical Monograph Series 79*

Lewellen, D.C., Lewellen, W.S., Xia. J, 2000. *The influence of a local swirl ratio on tornado intensification near the surface. Journal of the Atmospheric Sciences 57,527-544*

Liu, Z. and Ishihara T., 2012. *Effects of the swirl ratio on the turbulent flow fields of tornado-like vortices by using LES turbulent model. The 7ᵗʰ International Colloquium on Bluff Body Aerodynamics and Applications. Shanghai, China*

Markowski, P.M., Richardson, Y.P., 2009. *Tornadogenesis: Our current understanding, forecasting considerations, and questions to guide future research. Atmospheric Research 93, 3–10*

Mayer, L.J., 2009. *Development of a Large-Scale Tornado Simulator. Master Thesis, Mechanical Engineering, Texas Tech University*

Meaden, G.T., 1976. *Tornadoes in Britain: their intensities and distribution in space and time. Journal of Meteorology 1, 242–251*

Mishra, A.R., James, D.L., Letchford, C.W., 2008a. *Physical simulation of a single-celled tornado-like vortex, Part A: Flow field characterization. Journal of Wind Engineering and Industrial Aerodynamics 96, 1243-1257*

Mishra, A.R., James, D.L., Letchford, C.W., 2008b. *Physical simulation of a single-celled tornado-like vortex, Part B: Wind loading on a cubical model. Journal of Wind Engineering and Industrial Aerodynamics 96, 1258-1273*

Monji, N., 1985. *A Laboratory Investigation of the Structure of Multiple Vortices. Journal of the Meteorological Society of Japan, Vol. 63, No. 5, 703–712*

Monji, N. and Yunkuan, W., 1989. *A Laboratory Investigation of Characteristics of Tornado-Like Vortices over various rough surfaces*

Munson, B.R., Okiishi, T.H., Huebsch, W.W., Rothmayer, A.P., 2012. *Fundamentals of Fluid Mechanics, 7ᵗʰ edition. John Wiley & Sons, Inc. ISBN: 9781118370438*

Natarajan, D., Hangan H., 2012. *Large eddy simulations of translation and surface roughness effects on tornado-like vortices. Journal of Wind Engineering and Industrial Aerodynamics 104-106, 577-584*

NOAA₁-*National Oceanic and Atmospheric Administration. Storm Prediction Center-Current Convective Watches (last accessed 06/07/2018)*

NOAA₂–*National Oceanic and Atmospheric Administration. U.S. Department of Commerce. Tornadoes 101–An essential guide to tornadoes: Stay alert to stay alive (last accessed 28/05/2018)*

NOAA₃-*National Oceanic and Atmospheric Administration. U.S. Department of Commerce. Tornadoes – Annual 2011 (last accessed 06/06/2018)*

NOAA₄–National Oceanic and Atmospheric Administration. U.S. Department of Commerce. On This Day: 2011 Tornado Super Outbreak (last accessed 28/05/2018)

NOAA₅–Explanation of severe weather parameters (last accessed 27/05/2018)

NSSL₁–The National Severe Storms Laboratory. Severe Weather 101-Tornadoes: Tornado Basics (last accessed 28/05/2018)

NSSL₂-The National Severe Storms Laboratory. Severe Weather 101-Tornadoes: Tornado Forecasting (last accessed 06/07/2018)

NSSL₃-The National Severe Storms Laboratory. Severe Weather-101-Tornadoes:FAQ about Tornadoes (last accessed 06/07/2018)

NSSL₄ –The National Severe Storms Laboratory. VORTEX @ NSSL (last accessed 02/07/2018)

Pearson, K., 1905. Das Fehlergesetz und seine Verallgemeinerungen durch Fechner und Pearson. A Rejoinder, Biometrika 4, 169-212

Promet–Meteorologische Fortbildung (DWD), 1971 (1/2). Mikro- und Makroturbulenz (last accessed 28/05/2018)

Rankine, W.J.M., 1882. A Manual of Applied Physics, 10ᵗʰ edition. Charles Griff and Co.

Refan, M., Hangan, H., Wurman, J., 2014. Reproducing tornadoes in laboratory using proper scaling. Journal of Wind Engineering and Industrial Aerodynamics 135, 136-148

Refan, M., Hangan, H., 2016. Characterization of tornado-like flow fields in a new model scale wind-testing chamber. Journal of Wind Engineering and Industrial Aerodynamics 151, 107-121

Refan, M. and Hangan, H., 2017a. Surface pressures dependency on Reynolds number and swirl ratio in tornado vortices. The 13ᵗʰ Americas Conference on Wind Engineering, Gainesville, FL, USA

Refan, M., Hangan, H., Wurman, J., Kosiba, K., 2017b. Doppler radar-derived wind field of five tornado events with application to engineering simulations. Engineering Structures 148, 509-521

Refan, M. and Hangan, H., 2018. Near surface experimental exploration of tornado vortices. Journal of Wind Engineering & Industrial Aerodynamics 175, 120–135

Reynolds, O., 1883. An experimental investigation of the circumstances which determine whether the motion of water shall be direct or sinuous, and of the law of resistance in parallel channels. Proc. R. Soc. Lond. Vol. 35, No. 224-226, 84-99

Rohatgi, V.K., 1976. An Introduction to Probability Theory and Mathematical Statistics. John Wiley & Sons, New York-London-Sydney-Toronto. 684pp

Rott, N., 1958. On the viscous core of a line vortex. Zeitschrift für angewandte Mathematik und Physik 9, 543-553

Rotunno, R., 1977. Numerical simulation of a laboratory vortex, Journal of Atmospheric Science 34, 1942-1956

Rotunno, R., 1979. A study in tornado-like vortex dynamics, J Journal of Atmospheric Science 36, 140-155

Rotunno, R., 2013. The Fluid Dynamics of Tornadoes. Annual Review in Fluid Mechanics 45, 59–84

Sabareesh, G.R., Matsui, M., Tamura, Y., 2012.Dependence of surface pressures on a cubic building in tornado like flow on building location and ground roughness. Journal of Wind Engineering and Industrial Aerodynamics 112, 52-57

Sabareesh, G.R., Matsui, M., Tamura, Y., 2013a. Characteristics of internal pressures and net local roof wind forces on a building exposed to a tornado-like vortex. Journal of Wind Engineering and Industrial Aerodynamics 103, 50-59

Sabareesh, G.R., Matsui, M., Tamura, Y., 2013b. Ground roughness effects on internal pressure characteristics for buildings exposed to tornado-like flow. Journal of Wind Engineering and Industrial Aerodynamics, 122, 113-117

Sarkar, P. P., Haan, F. L., Balaramudu, V., and Sengupta, A., 2006. Laboratory simulation of tornado and microburst to assess wind loads on buildings. ASCE Structures Congress, Reston, VA, USA

Sarkar, P, Haan, F.,Gallus, W., Wurman, J., 2014. Velocity Measurements in a Laboratory Tornado Simulator and their comparison with Numerical and Full-Scale Data

Sengupta, A., Haan, F. L., Sarkar, P. P., and Balaramudu, V., 2008. Transient loads on buildings in microburst and tornado winds. Jouornal of Wind Engineering and Industrial Aerodynamics 96, 2173–2187

shutterstock – Joplin, MO, tornado – May 21, 2011 by Melissa Brandes. Image ID: 80099773 (last accessed 06/07/2018)

shutterstock – supercell storm in Kansas, US, by Cammie Czuchnicki. Image ID: 470220380 (last accessed 05/07/2018) (last accessed 05/07/2018)

shutterstock – tornado in Colorado, US, by Justin Hobson. Image ID: 303480896 (last accessed 05/07/2018)

Snow, J.T., 1982. A Review of Recent Advances in Tornado Vortex Dynamics. Review of Geophysics and Space Physics 20, 953–964

Solution for Research Ltd. (last accessed: 06/06/2018)

Stull, R., 2015. Practical Meteorology - An Algebra-based Survey of Atmospheric Science. ISBN-13: 978-0-88865-176-1

Sullivan, R.D., 1959. A Two-Cell Vortex Solution of the Navier-Stokes Equations. Journal of the Aerospace Sciences 26, 767-768

Tang, Z., Feng, C., Wu, L., Zuo, D., James, D.L., 2018. Characteristics of Tornado-Like Vortices Simulated in a Large-Scale Ward-Type Simulator. Boundary-Layer Meteorology 166, 327–350

TFI Manual: Series 100 Cobra Probe, 2011 (last accessed: 08/05/2018)

Trapp, R.J., 2000. A Clarification of Vortex Breakdown and Tornadogenesis. Monthly Weather Review 128, 888–895

TWISTEX - Tactical Weather Instrumented Sampling in Tornadoes Experiment – About the Project (last accessed 02/07/2018)

Vatistas, G.H., Kozel V. and Mih, W.C., 1991. A simpler model for concentrated vortices. Experiments in Fluids, 11, 73–76

Vyas, A. B., Majdalani, J., and Chiaverini, M. J., 2003. The Bidirectional Vortex. Part 1: An Exact Inviscid Solution

Wan, C.A. and Chang, C.C., 1971. Measurement of the Velocity Field in a Simulated Tornado-Like Vortex Using a Three-Dimensional Velocity Probe. Journal of the Atmospheric Science 29. 116–127

Ward, N.B., 1972. The Exploration of Certain Features of Tornado Dynamics Using a Laboratory Model. Journal of the Atmospheric Science 29, 1194–1204

Whipple, A.B.C., 1982. Storm. Planet Earth. Time-Life Books, Vol. 4. New York

Winn, W.P., Hunyady, S.J., Aulich, G.D., 1999. Pressure at the ground in a large tornado. Journal of Geophysical Research: Atmospheres 104, 22067-22082

Wood, V.T., Brown, R.A., 2011. Simulated Tornadic Vortex Signatures of Tornado-Like Vortices Having One- and Two-Celled Structures. Journal of Applied Meteorology and Climatology 50, 2338-2342

Wood, V.T., White, L.W., 2011. A New Parametric Model of Vortex Tangential-Wind Profiles: Development, Testing, and Verification. Journal of the Atmospheric Sciences 68, 990-1006

Wurman, J., Gill, S., 2000. Finescale Radar Observations of the Dimmitt, Texas (2 June 1995), Tornado. Monthly Weather Review 128, 2135-2164

Wurman, J., Kosiba, K., Robinson, P., 2013. In Situ, Doppler radar, and Video Observations of the Interior Structure of a Tornado and the Wind–Damage Relationship. Bulletin of the American Meteorological Society 94, 835-846

Xu, Z and Hangan, H., 2009. An Inviscid Solution for Modeling of Tornado-like Vortices. Journal of Applied Mechanics 76, 31011-31015

Yang, Z., Sarkar, P. Hu, H., 2011. An experimental study of a high-rise building model in tornado-like winds. Jounral of Fluids and Structures, 27, 471-486

Zhang, W. and Sarkar, P.P., 2012. Near-ground tornado-like vortex structure resolved by particle image velocimetry (PIV). Exp. Fluids 52, 479-493

Zuh, J., Cao, S., Tamura, T., 2016. Numerical study of the effects of rotating forced downdraft in reproducing tornado-like vortices. APS Division of Fluid Dynamics